GDAŃSK UNIVERSITY OF TECHNOLOGY
Faculty of Applied Physics and Mathematics

The author of the PhD dissertation: Damian Głowienka
Scientific discipline: Physics

DOCTORAL DISSERTATION

Title of PhD dissertation:
"Electrical properties of organic and perovskite systems used in solar cells"

Title of PhD dissertation (in Polish):
„Właściwości elektryczne układów organicznych i perowskitowych stosowanych w ogniwach słonecznych"

Supervisor *signature*	Second supervisor *signature*
dr hab. inż. Jędrzej Szmytkowski, prof. nadzw. PG.	
Auxiliary supervisor *signature*	Cosupervisor *signature*

Gdańsk, year 2019

Scientific papers with results presented in this work

D. Głowienka, J. Szmytkowski
Influence of Excitons Interaction with Charge Carriers on Photovoltaic Parameters in Organic Solar Cells,
Chemical Physics 503 (**2018**) 31–38

D. Głowienka, J. Szmytkowski
Modeling of Transient Photocurrent in Organic Semiconductors Incorporating the Annihilation of Excitons on Charge Carriers,
Acta Physica Polonica A 132 (**2017**) 397–400

D. Głowienka, T. Miruszewski, J. Szmytkowski
The Domination of Ionic Conductivity in Tetragonal Phase of the Organometal Halide Perovskite $CH_3NH_3PbI_{3-x}Cl_x$,
Solid State Sciences 82 (**2018**) 19–23

D. Głowienka, J. Szmytkowski
Numerical Modeling of Exciton Impact in Two Crystalographic Phases of the Organo–lead Halide Perovskite ($CH_3NH_3PbI_3$) solar cell,
Semiconductor Science and Technology 34 (**2019**) 035018

D. Głowienka, D. Zhang, F. D. Giacomo, M. Najafi, S. Veenstra, J. Szmytkowski, Y. Galagan
Role of Surface Recombination in the Interface of Cu:NiO_x/$CH_3NH_3PbI_3$ Perovskite Solar Cells,
submitted (**2019**)

D. Głowienka, F. D. Giacomo, M. Najafi, J. Szmytkowski, Y. Galagan
The Effect of Different Source of Bromide on Perovskite $Cs_{0.18}Fa_{0.82}Pb(I_{0.94}Br_{0.06})_3$ Solar Cells,
in preparation

Additional papers

M. Martynow, D. Głowienka, J. Szmytkowski, Y. Galagan, J. Guthmuller
Relation Between Structural and Optical Absorption Properties in Hybrid Metal–Halide Perovskite $CH_3NH_3PbI_3$ Investigated by DFT/TD-DFT Calculations and Experimental Methods,
in preparation

Conference contributions

D. Głowienka, T. Miruszewski, B. Kusz, J. Szmytkowski
Badanie Własności Strukturalnych oraz Elektrycznych Związków o Strukturze Perowskitu $CH_3NH_3PbI_3$ oraz $CH_3NH_3PbI_{3-x}Cl_x$.
Kryształy Molekularne, Kazimierz Dolny, Poland. 12–16 September **2016**, Poster

D. Głowienka, J. Szmytkowski
Modeling of Transient Photocurrent in Organic Semiconductors Incorporating the Annihilation of Excitons on Charge Carriers,
46th International School & Conference on the Physics of Semiconductors 2017, Szczyrk, Poland. 17–23 June **2017**, Poster

D. Głowienka, J. Szmytkowski
Badanie Roli Ekscytonów w Fazie Tetragonalnej i Rombowej w Perowskitowym Ogniwie Słonecznym,
Kryształy Molekularne, Kolumna, Poland. 3–7 September **2018**, Poster

D. Głowienka, F. D. Giacomo, M. Najafi, J. Szmytkowski, Y. Galagan
The Effect of Different Source of Bromide on Perovskite $Cs_{0.18}Fa_{0.82}Pb(I_{0.94}Br_{0.06})_3$ Solar Cells,
European Materials Research Society, Warsaw, Poland. 17–20 September **2018**, Poster

D. Głowienka, D. Zhang, F. D. Giacomo, M. Najafi, S. Veenstra, J. Szmytkowski, Y. Galagan
Surface Recombination in the Interface of $Cu:NiO_x/CH_3NH_3PbI_3$ Perovskite Solar Cells,
Pomorsko–Wielkopolskie Forum Nanotechnologiczne, Gdańsk, Poland. 24–26 September **2018**, Talk

M. Martynow, D. Głowienka, J. Szmytkowski, Y. Galagan, J. Guthmuller
Structural and Optical Properties of Hybrid Halide Perovskite ($CH_3NH_3PbI_3$) Investigated by DFT and TD-DFT Simulations,
European Materials Research Society, Nice, France. 27–31 May **2019**, Poster

A part of this thesis has been supported by National Science Center, Poland 2018/29/N/ST7/02326, Grant PRELUDIUM 15. Calculations were carried out at the Academic Computer Centre (CI TASK) in Gdańsk.

Abstract

Currently, a great progress in the areas of molecular and hybrid electronics and photovoltaics is observed. The devices based on organic materials can be flexible and their cost of production is very low which make them suitable for application in solar cells. However, their efficiency and stability are much lower than for inorganic materials which causes that they are still less popular. Recently, the hybrid organic–inorganic materials have attracted a lot of attention. Their cost of production is also low due to a solution processing which, similarly to organic devices, make them flexible. Perovskite solar cells are one of most popular hybrid photovoltaic devices and drew the attention due to a tremendous increase of efficiency in a short period of time. However, before commercialization there have to be solved few problems related to ionic conductivity, long–time stability and toxicity. Therefore, a detailed understanding of the device physics is fundamental for organic and perovskite solar cells. The goal of this thesis is to understand which processes influence the electrical properties of both types of solar cells. Here, numerical and experimental techniques are used to accurately determine and understand electrical phenomena taking place in both organic and perovskite photovoltaic cells.

The role of excitons is greater for organic structures as the photogeneration of charge carriers occurs as a result of excitons dissociation into separated electrons and holes. Therefore, the excitonic processes are dominant for operation of organic solar cells and give a visible contribution to photoelectric properties of such devices. Thus, here we discuss the influence of excitons interaction with electrons and holes on photovoltaic parameters and dynamics of the operation. Also, the influence of the nonuniform generation profile and interfaces are shown to give a better understanding of the exciton annihilation mechanism. It has been found that physics of the process is crucial for understanding of the organic solar cells operation. The exciton annihilation has been shown to observably influence all the photovoltaic parameters, especially when simulated with interfaces.

Here, we present studies of the excitons impact in the perovskite solar cell operating in two crystallographic phases associated with different temperatures (80 K and 295 K). They are done based on the Saha relation and numerical simulations, which clearly distinguish a domination of free charge carriers or excitons. It has been confirmed that excitons prevail in the orthorombic phase and that excitons formation is mostly observable for a case of an open–circuit. We have also investigated the contribution of iodide ions to a total conductivity of

the perovskite material with a use of the modified DC Hebb–Wagner polarization method. It has been identified that an ionic conductivity dominates in tetragonal phase which is associated with a room temperature. We have found the activation energy of ions in perovskite material equal to 0.87±0.02 eV, which is in a good agreement with previous literature reports. The high contribution of ionic conductivity at a room temperature might be a reason of the observed hysteresis in halide perovskite solar cells which is still very important problem in the perovskite photovoltaics.

In order to achieve the highest performance of organometal trihalide perovskite solar cells, the dominant mechanisms which play a key role in a perovskite material are required to be recognized. Therefore, we have focused on the interfacial recombination between the hole transporting layer (HTL) and the perovskite material in solar cell devices with p–i–n architecture. It has been experimentally shown that Cu:NiO_x used as a HTL drastically decreases a short–circuit photocurrent and an open–circuit voltage. However, we have found that an addition of PTAA thin layer improves cells quality and, as a consequence, the efficiency of such solar cells increases by 2%. Here, based on experimental results and numerical simulations, we have explained that both losses are related to a "dead layer", where a very high surface recombination occurs. The studies have been demonstrated by the means of series detailed analyses to get in–depth understanding of the physical processes. The following results could be useful for improving the quality of perovskite solar cells.

The recent research for improvement in stability has led to the conclusion that perovskite solar cells with a mixed dual A–cation have much better structural stability without loss of efficiency. Simultaneously, the electrical properties are not reduced. However, using a dual cation in the perovskite raises a question which salt should be used to introduce bromide ions. Here, we have investigated the three sources of bromide in the perovskite absorption layer, using lead bromide ($PbBr_2$), formamidinium bromide (FABr) and cesium bromide (CsBr). The experimental results have shown a better performance for FABr and CsBr sources of bromide in comparison to regularly used $PbBr_2$. This effect has been explained with the properties of colloidal dispersion present in the perovskite solutions which changes the defect states during the crystallization of the absorber layer. It has been found with numerical simulations that observed phenomena directly impacts the rates of the trap–assisted recombination. The following results are step forward in understanding the physics behind the crystallization process which is crucial in further improvement of the perovskite solar cells.

Streszczenie

W obecnych czasach obserwowany jest znaczący postęp w dziedzinie molekularnej i hybrydowej elektroniki, a zwłaszcza fotowoltaiki. Jedną z głównych przyczyn sprawiającą, że struktury oparte na materiałach organicznych są stosowane w ogniwach słonecznych są ich właściwości elastyczne, a także bardzo niski koszt produkcji. Jednakże ich wydajność i stabilność są znacznie gorsze niż w przypadku materiałów nieorganicznych, co sprawia, że nadal są mniej popularne. Dlatego też materiały hybrydowe składające się z części organicznej i nieorganicznej przyciągają ostatnimi czasy wiele uwagi. Podobnie do materiałów organicznych mogą być one elastyczne, jak również ich koszt produkcji jest niski. Jedną z najpopularniejszych struktur hybrydowych są perowskitowe ogniwa słoneczne, które zwróciły uwagę ze względu na znaczący wzrost wydajności w krótkim okresie czasu. Jednak zanim nastąpi ich komercjalizacja należy rozwiązać problemy związane z przewodnością jonową, długotrwałą stabilności, a także z toksycznością. Dlatego też szczegółowe zbadanie fizyki ogniw słonecznych bazujących na materiałach organicznych i perowskitowych ma fundamentalne znaczenie. Celem tej pracy jest zrozumienie, które mechanizmy wpływają na właściwości elektryczne obu typów ogniw słonecznych. W tym przypadku techniki numeryczne i eksperymentalne zostały wykorzystane do dokładnego określenia i zrozumienia zjawisk elektrycznych zachodzących zarówno w organicznych, jak i perowskitowych ogniwach fotowoltaicznych.

Rola ekscytonów jest większa dla struktur organicznych, ponieważ fotogeneracja nośników ładunku zachodzi w wyniku dysocjacji ekscytonów na swobodne elektrony i dziury. Dlatego też procesy ekscytonowe są dominujące podczas działania organicznych ogniw słonecznych i wyraźnie wpływają na właściwości fotoelektryczne takich urządzeń. Z tego powodu, w poniższej pracy omawiany jest wpływ oddziaływania ekscytonów z elektronami i dziurami na parametry fotowoltaiczne, a także na dynamikę funkcjonowania ogniwa. Pokazano również rolę niejednorodnego profilu generacji i zjawisk międzyfazowych, aby lepiej zrozumieć mechanizm anihilacji ekscytonów. W pracy pokazano, że ten proces ekscytonowy ma kluczowe znaczenie dla działania organicznych ogniw słonecznych. Udowodniono również, że anihilacja ekscytonów w widoczny sposób wpływa na wszystkie parametry fotowoltaiczne, zwłaszcza gdy jest symulowana z uwzględnieniem interfejsów.

Przedstawiono wyniki badań wpływu ekscytonów w perowskitowym ogniwie słonecznym znajdującym się w dwóch fazach krystalograficznych związanych z różnymi temperaturami (80 K i 295 K). Procesy ekscytonowe zostały przebadane za pomocą równania Saha i symu-

lacji numerycznych, które pozwoliły na wyodrębnienie dominacji swobodnych nośników ładunku lub ekscytonów. Dzięki temu, potwierdzono dominacje ekscytonów w fazie rombowej, zaś proces tworzenia się ekscytonów można zaobserwować głównie w przypadku ogniwa działającego w obwodzie otwartym. Zbadany został również udział jonów w całkowitej przewodności materiału perowskitowego z użyciem zmodyfikowanej techniki polaryzacji stałonapięciowej Hebb–Wagner'a. Wyniki badań pokazały, że przewodnictwo jonowe dominuje w fazie tetragonalnej występującej w temperaturze pokojowej. Wyznaczona energia aktywacji jonów w materiale perowskitowym równa jest 0.87±0.02 eV, co jest w dużej zgodności z wcześniejszymi doniesieniami literaturowymi. Wysoki udział przewodnictwa jonowego w temperaturze pokojowej może być przyczyną zaobserwowanego efektu histerezy w perowskitowych ogniwach słonecznych, która jest nadal bardzo ważnym problemem w badanych materiałach.

Aby uzyskać najwyższą wydajność ogniw słonecznych bazujących na halogenkowym materiale perowskitowym, kluczowe jest rozpoznanie dominujących mechanizmów ograniczających działanie tych ogniw. Dlatego też, dalsze badania skupiły się na rekombinacji międzyfazowej zachodzącej pomiędzy warstwą transportującą dziury (HTL), a materiałem perowskitowym w ogniwach ze strukturą p–i–n. Wyniki eksperymentu pokazały, że użyty materiał Cu:NiO_x jako HTL drastycznie zmniejsza wartość prądu zwarcia i napięcie obwodu otwartego. Stwierdzono jednak, że dodanie cienkiej warstwy PTAA poprawia jakość badanych ogniw słonecznych, a w konsekwencji wydajność wzrasta o 2%. W poniższej pracy wyjaśniono, że obserwowane straty są związane z tzw. "martwą warstwą", w której zachodzi bardzo wysoka rekombinacja powierzchniowa. Wykonano serię szczegółowych analiz wykorzystujących symulacje numeryczne, które pozwoliły odtworzyć wyniki eksperymentalne. Otrzymane wyniki mogą być przydatne do dalszej poprawy jakości perowskitowych ogniw słonecznych.

Ostatnie badania nad poprawą stabilności wykazały, że perowskitowe ogniwa słoneczne z mieszanym podwójnym kationem mają znacznie lepszą stabilność strukturalną. Jednocześnie właściwości elektryczne nie są zmniejszone, a więc zachowana jest wysoka wydajność. Jednak zastosowanie podwójnego kationu w perowskicie rodzi pytanie jaki związek powinien być użyty do wprowadzenia jonów bromkowych. W poniższej pracy zbadano trzy źródła bromku w warstwie absorpcyjnej perowskitu, używając bromku ołowiu ($PbBr_2$), bromku formamidyny (FABr) i bromku cezu (CsBr). Wyniki eksperymentalne wykazały lepszą wydajność dla ogniw z użyciem FABr i CsBr w porównaniu z regularnie stosowanym $PbBr_2$. Efekt ten wyjaśniono właściwościami koloidów występującej w dyspersyjnych roztworach perowskitu, które wpływają na ilość defektów w czasie krystalizacji warstwy absorbującej. Dzięki symulacjom numerycznym stwierdzono, że obserwowane zjawiska bezpośrednio wpływają na szybkość rekombinacji przez stany pułapkowe. Uzyskane wyniki pozwalają lepiej zrozumieć fizykę procesu krystalizacji, która ma kluczowe znaczenie dla dalszego ulepszania perowskitowych ogniw słonecznych.

Contents

Chapter I

Introduction

Nowadays, the generation of electricity is mostly made with fossil fuels which also make the basis of the modern economy. However the resources are limited and leads to warming of the global climate. Therefore, the cleaner technologies are sought and the renewable energy production starts to play an important role. The solar energy is unlimited and could easily covered all the human needs for electricity. Therefore, there has been observed a constant progress in the development of photovoltaic materials. The most popular material is still silicon which gives the highest efficiency and stability so far. However, the cost of production of monocrystalline silicon solar cells is high mostly due to a process of production. Therefore, the organic solar cells have been proposed as alternative due to a low cost of production but the efficiency and stability are still lower than for regular solar cells. Thus it needs further progress before commercialization. The other group of materials applied in photovoltaics are perovskite materials which progressed in efficiency very quickly. The organic and perovskite materials are getting attention as future semiconductors in photovoltaics. To overcome the limiations related with these solar cells, the deeper studies are needed. The goal of the thesis is to understand physical phenomena taking place in organic and perovskite solar cells.

In the first part of the chapter, the economical and ecological aspects of photovoltaics are given to motivate the following studies. Further, the general description of organic and perovskite solar cells is given with their basic principles of operation. Subsequently, the widely applied current–voltage characterization method for solar cells is described. At last, the overview of the following thesis is presented.

1.1 Energy economy

The industrial technologies and living standards are mainly dependent on the stored energy resources, therefore the industrial evolution drives the energy consumption observably. Figure 1.1(a) shows the trend of primary energy (rather than final energy) consumption globally. In the 20^{th} century, the energy consumption has raised drastically and about 87% of total en-

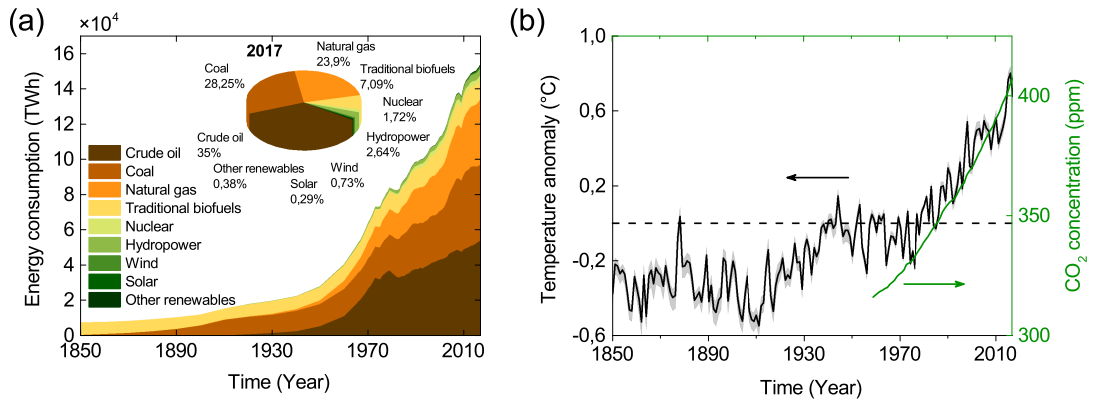

Figure 1.1: Statistical data of a) global primary energy consumption measured in terawatt–hours (TWh) per year with different source, and b) average global temperature anomaly and CO_2 concentration. The inset of (a) shows global energy consumption by different sources from 2017. The experimental data is extracted from literature [3–5].

ergy is mainly built upon fossil fuels (crude oil, coal and natural gas). However, there are two main problems with the use of fossil fuels, meaning their limit resources and contribution to environmental warming process [1, 2].

First, the fossil fuels are organic materials developed millions of years ago which make them non–reusable. Thus, their resources are limited and depleting rapidly as new reserves are becoming harder to find. There are different models predicting how much time should left before total depletion of fossil fuels. The results show scarce of energy supply in the next two decades, especially in the transportation before 2020. The electricity generation from fosil fuels should not fulfill the demands already in 2025–2040 [6]. The other problem is the global warming effect. Their organic structure is based mainly on hydrogen, carbon and nitrogen elements. Therefore, fossil fuels combustion leads to a production of greenhouse gases which emission has been related with a long–term global temperature change [7]. This relation comes as a result of the dominant production of CO_2 which is about three quarters of total annual anthropogenic greenhouse gases and it has a long atmospheric lifetime [8, 9]. Figure 1.1(b) shows the global average temperature anomaly and CO_2 concentration. It is observed that with increase of carbon oxide concentration, the annual temperature is rising almost linearly from 1960s. It is has been agreed that the rise over 2°C of global temperature anomaly may lead to irreversible changes in the climate. The critical warming of 2°C would lead to heat waves, reduction in annual water availability, global sea level rise, changes in local crop yields, etc. [10]. Therefore, the international climate policy under the United Nations Framework Convention on Climate Change has taken the goal to keep the global mean temperature below 1.5°C [11].

The different mitigation scenarios are proposed to decrease the production of greenhouse gases, and therefore not to allow to increase the global temperature. This mostly includes changes in policy to reduce CO_2 emission by changing fuel emission standards and increasing

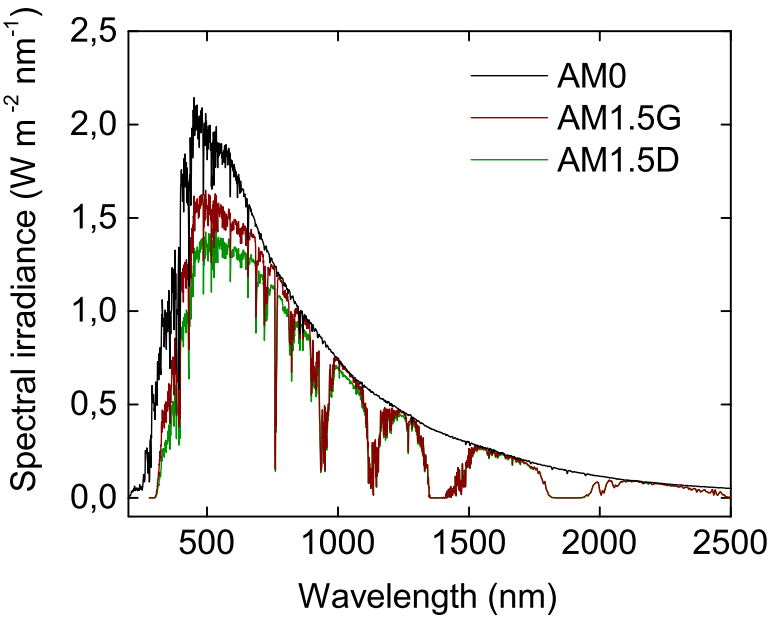

Figure 1.2: Spectral irradiance as a function of wavelength for AM0, AM1.5G and AM1.5D. Data is adopted from [13].

the requirement for renewable energy resources [12]. Today, only approximately 4% of global energy production is coming from renewable energy resources and 9% from green energy including nuclear power and biofuels, see Figure 1.1(a-inset). The solar installations have already demonstrated an economical and expansion potential with the use of organic and perovskite materials. Therefore, the further development of these solar cells are crucial for future of energy sector.

1.2 Solar energy supply

The solar energy reaching the earth is in the form of photons which possess an energy that further could be transformed to any form of electricity or heat. The amount of energy produced by sun which reaches the earth is enourmously high and could easily cover all the human needs. Figure 1.2 shows the spectrum of light reaching top regions of the earth, meaning there is no absorption through the atmosphere. Therefore, it is called the air mass zero (AM0), as there is no air between the sun and the measuring point. This is practical for usage of solar cell out of space and corresponds to energy of 1353 W m^{-2}. However, the most of solar cells are measured under solar spectrum with irradiation through the atmosphere. A typical spectrum for a moderate climate is AM1.5 which assumes an angle of incidence of solar irradiation equal to 47° in respect to the surface. The integral of AM1.5 spectrum gives a total irradiation energy equal to 1000 W m^{-2}. The differences in total energy are coming

from the absorption of photons by molecules present in the atmosphere. Further AM1.5 is divided into a global spectrum (AM1.5G) and a direct beam from the sun (AM1.5d). Figure 1.2 shows both as a function of wavelength. The AM1.5G includes a total direct and diffuse light, while the AM1.5D only the irradiation from 2.5° circumsolar component [14]. The latter is useful for solar concentrated light which is not a part of the thesis. Therefore, only AM1.5G will be further used and called AM1.5 for simplicity. To harvest solar energy, the sun transforming energy devices are needed. In a case of conversion to electricity, the photovoltaic solar cells are used.

1.3 The basics of semiconductor physics

The operation of p-i-n junction applied in the perovskite solar cell is given in a brief version. The more detailed description can be found in the literature [14–16]. Next, a short information about the operation of organic solar cell will be presented. Also for this case, the deeper description of organic solar cell is widely available in the literature [17].

1.3.1 The perovskite solar cell

Hybrid organic-inorganic perovskites attracted a lot of attention in the last ten years since these materials started to be used as an absorber layer in solar cells. Their general structure is ABX_3, where A is a small organic cation, B represents a divalent metallic cation, and X denotes a halogen anion. The most frequently used compound with a perovskite crystallographic structure is methylammonium lead halide $CH_3NH_3PbI_3$. However, recently, the perovskite materials with a mixed dual A–cation (2C) has brought a much atention as they have better structural stability without loss of efficiency [18]. With a continuous progress in the field, current state-of-the-art power conversion efficiency of perovskite solar cells (PSCs) reached the record value of 23.7% [19]. The outstanding performance of this material is due to a direct band–gap [20], a high charge carrier mobility [21], a small exciton binding energy [22] and a high absorption coefficient in a wide spectrum of light [23]. However, the electrical and transport properties of trihalide perovskites may drastically change with a phase transition. Three phases of the organo–lead halide perovskite material are observed in different temperature regimes [24–26]. The orthorhombic phase is present at a low temperature and converts into tetragonal phase at about 160 K. The transition between tetragonal and cubic phases takes place above 330 K [27–29].

The performance of PSCs are still far from the final goal. The analysis of current–voltage characteristics demonstrates the effect of rate–dependent hysteresis in numbers of such structures [30–32]. Therefore, the understanding of the major mechanism influencing the hysteresis effect is crucial for a future development of the perovskite solar cells. According to Snaith *et al.* [30], there are three possible explanations of the hysteresis: (1) the large density of defect states at the interface, (2) ferroelectric properties and slow polarization of the material, and (3) the polarization–dependent moveable ions which can screen a space charge built–up

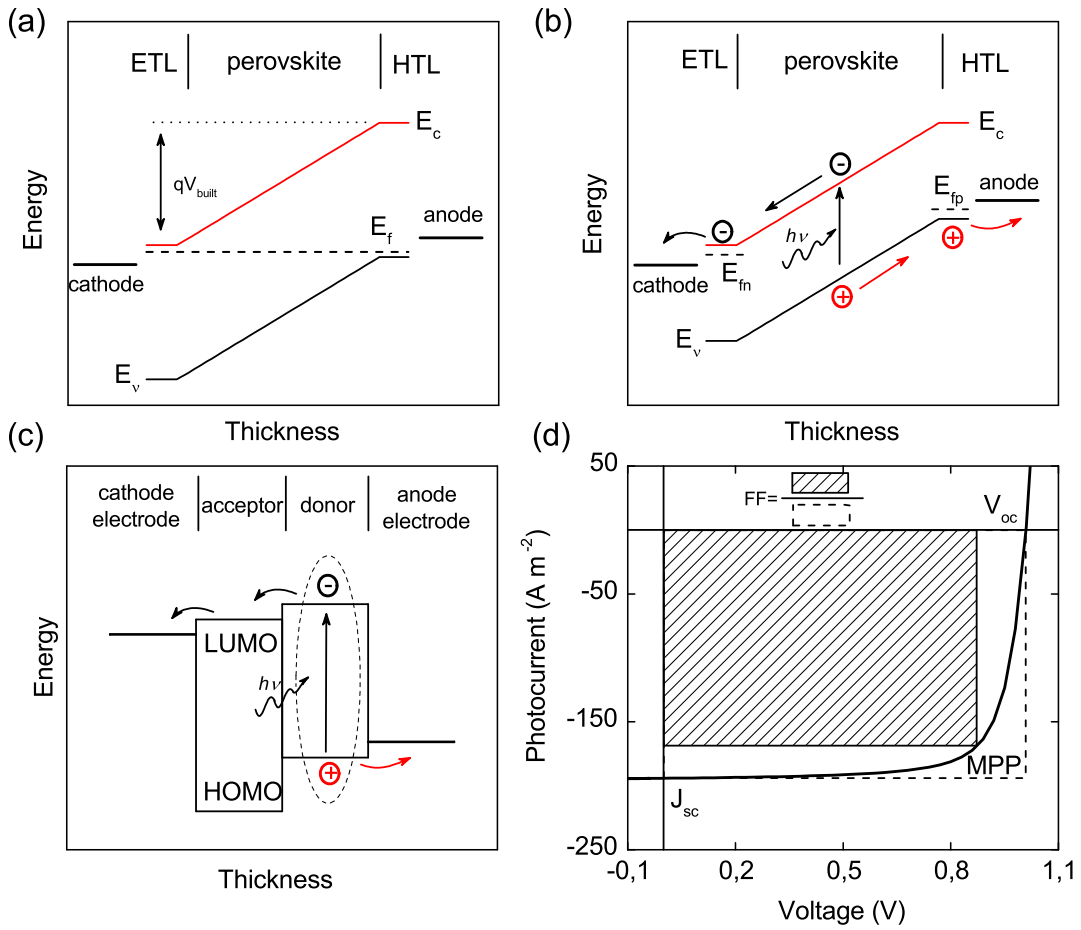

Figure 1.3: Energy band diagram of a) p-i-n junction solar cell at a thermal equilibrium in the dark conditions, b) p-i-n junction solar cell at a non–equilibrium with external light source, and c) organic solar cell with an external light source. d) The regular J–V characteristics showing characteristic points.

that influences the charge collection at the contacts. The previous studies suggest that the time of interfacial trapping and ferroelectric domain are not the source of hysteresis solely [32–34]. However, it seems that ions accumulate at the interface of electrodes and screen the built–in electric field independently of illumination [35]. Therefore, the conclusion is that the ionic flow with a timescale of seconds to minutes could create the J–V hysteresis dependently of voltage sweep rate. Also, the ion diffusion has been connected with a stability of perovskite solar cells [36]. Thus, the further studies of perovskite physics are needed to understand their mechanism of operation to increase their stability and efficiency which would lead to commercialization of PSCs in the future.

Figure 1.3 shows a simple model to explain basics of solar cell operation. Perovskite solar cells could be constructed in regular n-p and n-i-p structures or inverted p-n or p-i-n stacks,

where p and n stands for a hole transporting layer (HTL) and an electron transporting layer (ETL), respectively. The intrinsic (i) layer is a perovskite semiconductor. In this thesis, only p-i-n structure will be considered. The HTL and ETL have the ability to transport only one sign charge carriers in the used structure due to different energy affinities in the solar cell. When these types of semiconducting materials create a junction with a perovskite, it results in a total diffusion of charge carriers to the other side. Also, due to the built–in voltage (defined as the difference of the top to the bottom level of a conduction band of the ETL and HTL), the perovskite layer possess a built–in electric field, see Figure 1.3(a). The difference between p-i-n and p-n junctions is that in the the depletion region, the electron field extents over a wider region in intrinsic layer. The flow of electrons and holes lasts until the thermodynamical equilibrium state is reached and the Fermi level is equal across all three materials. At this condition, there is no flow of current through the PSC. The occupancy distribution of charge carriers at the corresponding bands can be well described with the Fermi–Dirac statistics.

The equilibrium state changes when the solar cell is irradiated and photons of energy higher than a band–gap (an energy difference between a conduction and a valence bands in the first Brillouin zone) are absorbed, as shown in Figure 1.3(b). Then both oppositely sign charge carriers can be separated by the built–in electric field. Further, the charges are transported and collected at the electrodes. This results in the flow of current which could be related to the transport of charge carriers by the electric field (drift) or a gradient of concentration (diffusion). The drift and diffusion currents constitute to the total current collected from the operating solar cell. Other scenarios gives the possibility of charge carriers to recombine. It should be noted that a light can create also the electron–hole pairs bound with a Coulomb force which keeps both charge carriers together. Such a pair is called the exciton. However, its creation is less possible in room temperatures for inorganic materials.

The non–equilibrium condition leads to creation of quasi–Fermi levels for electrons and holes. Under the biased condition, the applied voltage changes the built–in voltage depending on the direction of polarization. Thus, if an external voltage is positive, the Fermi levels raises on one side in respect to the other and charge carriers are injected from electrodes. When negative voltage is applied, the charge carriers are attracted to the electrodes. Therefore, the p-i-n junction acts as an rectifier with a nonlinear current to voltage characteristics.

1.3.2 The organic solar cell

Organic semiconductors are materials that possess a few features which make them suitable to construct electronic devices, like solar cells, light-emitting diodes, and transistors. Most importantly, their cost of production is relatively low. Therefore currently, a great progress in the areas of molecular electronics and organic photovoltaics is observed. Nevertheless, devices based on inorganic materials are still more popular due to their better stability and efficiency. In order to obtain more efficient organic solar cells, it is important to solve a problem which physical processes significantly influence their photovoltaic parameters.

The operation of organic solar cell is straightly different and requires other consideration.

Figure 1.3(c) shows an organic junction created from donor and acceptor materials. The difference lies down in the electron affinity levels for these two materials. The junction can be treated in a sandwich structure or by mixing in the bulk of two materials. The Lowest Unoccupied Molecular Orbital (LUMO) and the Highest Occupied Molecular Orbital (HOMO) can be created as analogs to valence and conduction bands in inorganic semiconductor. The electrical properties of organic semiconductor are much different, and their permittivity is much lower. This results in a much higher exciton binding energy which is higher than the thermal energy. Therefore, the absorption of photon causes the creation of an electron–hole pair (exciton) which is relatively strongly bonded. In such materials, excitons may dissociate into free charge carriers and then transported to electrodes driven by electric forces or the gradient of concentration. Both constitute to electric current flowing from the solar cell. However, in organic solar cell, the mechanisms concerning excitons are of main importance as the electric field resulting from a built–in potential is usually not sufficient for the dissociation of excitons. As a result, excitons may recombine before giving any contribution to the photocurrent. Therefore any process, which influences a concentration of excitons, is relevant for final efficiency of such devices [37, 38]. Also, this is one of the reasons, the blended bulk heterojunction solar cells have much higher efficiency, as the distance between distributed interface is much shorter than an exciton diffusion length which allows for higher dissociation rate at donor–acceptor interface.

1.3.3 The device characterization

In order to characterize the solar cell, the current–voltage (J–V) characteristics are measured. Figure 1.3(d) shows the regular characteristics obtained under AM1.5 condition by changing the applied voltage and measuring the output photocurrent. The plot exhibits a few characteristic points which are used for description of the solar cell. Under a zero applied voltage, the short–circuit current (J_{sc}) can be found. At the open–circuit voltage (V_{oc}) the current is zero and it is the maximum voltage that can be obtained during the operation of the solar cell. At the maximum power point (MPP) proportional to the voltage and photocurrent of the cell, the fill–factor (FF) can be calculated

$$FF = \frac{J_{MPP} V_{MPP}}{J_{sc} V_{oc}}. \tag{1.1}$$

Figure 1.3(d) shows the illustrative way to describe FF. The power conversion efficiency (PCE) is proportional to the output power of the cell and inversely proportional to the input power

$$PCE = \frac{J_{sc} V_{oc} FF}{I}, \tag{1.2}$$

where I represent the incident light intensity.

1.4 Objectives and a scope of the thesis

The aim of this thesis is to investigate the phenomena which influences electrical properties of organic and perovskite solar cells. A special attention is paid on an impact of different effects (excitonic processes, interface phenomena or recombination) on the photovoltaic parameters (J_{sc}, V_{oc}, FF and PCE). In addition, a role of different crystallographic phases is taken into account for perovskite systems.

In Chapter 2 all the details for the used numerical model are given which includes the drift–diffusion model description. The numerical model is the main tool used throughout the thesis to simulate the operation of solar cell. From the numerical simulation of the charge carrier mechanisms, the theory can be confirmed if properly used with the experiment.

Chapter 3 focuses on the annihilation of excitons on charge carriers. The steady–state and transient simulation results are provided to understand the operation of the solar cell. Further, the roles of generation profile and interfaces are shown for the same exciton annihilation rates.

Chapter 4 is focused on studies on perovskite solar cells to understand the exciton and ion properties. The numerical studies on excitonic processes are focused on answering the question if excitons prevails in room and low temperature. Also, the experimental studies of ionic conductivity in perovskite material based on the DC Hebb–Wagner polarization method are presented. Both parts of this Chapter describe the perovskite behavior in different crystallographic phases.

In Chapter 5, the role of the interfaces surface recombination between HTL and perovskite material is discussed. The experimental results of two types of PSCs with one having modified interface layer and one without modification are presented. The verification of the theory of a "dead layer" has been made with a numerical drift–diffusion model. The Chapter has been extended with numerical simulation with different dead layer thicknesses which helped in explanation of the role of surface recombination.

Chapter 6 focuses on the more complex double cation perovskite solar cells. Experimental studies of different source of salts in the perovskite layer to introduce bromide ions are shown. The influence of a crystallization process on photovoltaic parameters and recombination via trap states are also investigated by numerical simulations.

It should be noted that this work presents experimental and theoretical results obtained by author in Gdańsk University of Technology (Chapters 3 and 4) and in TNO Solliance in Eindhoven (Chapters 5 and 6). The synthesis of all perovskites were prepared by author of this thesis.

Chapter 2

Drift–diffusion modeling

Numerical modeling are highly desirable when discussing physical mechanisms, interpreting experimental results or searching the way to optimize the solar cell device. There are variety of simulation models which represent different scale and physical details. However, usually it is with the cost of calculation speed. Therefore, there has to be a compromise between a computation time and how detail the model is. It is also necessary to know the limitation of the used model to interpret the simulation results correctly by improper application of the numerical tool. The useful tool for macroscopic description is an equivalent circuit model. However, it does not give any detailed information about the dominant mechanism but rather gives macroscopic parameters which describe the device. Its computation time seems to be very short, therefore it still finds applications in variety of organic [39] and perovskite [40] solar cells. From the other hand, the quantum mechanical models are microscopic and give much more physical details but increase the computation time. They are used for simulation of processes taking place in molecular [41] or crystal materials [42]. The compromise between the physical details and the computation time is a drift–diffusion model which has been already applied in organic [43–46] and perovskite [47–50] solar cells. The numerical modeling applies physical parameters which are mostly acquired from the experiment. Most of the mechanisms can be used in the computational model to see their influence on the operation of solar cells. The limitation of the tool can be related to the conditions to simulate only free charge carriers which obey continuity equation. Considering all the advantages, the drift–diffusion model has been chosen as the main tool for the presented theoretical studies.

This chapter presents a brief description of theoretical models and mechanisms used in simulations reported in this thesis. However, we should note that this part cannot be treated as a full review of all theoretical formalisms which can be implemented in the drift-diffusion model [2]. First, we present the general concept of the drift–diffusion model quantitatively describing transport equations for charge carriers (electrons, holes, ions) and excitons. Next, the generation and recombination mechanisms which take place in solar cells are explained.

Further, we describe the details of boundary and interface conditions which completes the general numerical model. However, for simulation of the semiconducting devices, the numerical model has to be discretized and implemented with a specific algorithm that gives the iteration procedure used in the code. Finally in this chapter, the numerical results are confronted with a simple analytical model for validation purposes.

2.1 Governing equations and models

2.1.1 Poisson equation

According to one of the Maxwell equation (the Gauss's law), the density of charge carriers (ρ), which accumulate locally, causes the spatial change of electric field (F). This change creates the variations of an electric potential which is described by the Poisson equation

$$\frac{\partial^2 \varphi}{\partial x^2} = -\frac{q}{\varepsilon_0 \varepsilon_r} \rho(x), \tag{2.1}$$

where φ is a local electric potential that depends on the dielectric constant (ε_r) of the material and also on a total density of charge carriers (ρ). The equation presented here is one–dimensional (x) across the solar cell. The parameter ε_0 is a vacuum permittivity and q represents an elementary charge constant. The electric field distribution can be calculated from the following relation

$$F = -\frac{\partial \varphi}{\partial x}. \tag{2.2}$$

2.1.2 Electronic charge transport

Based on the Boltzmann equation, the continuity equations are given in the one–dimensional forms for electrons

$$\frac{\partial n}{\partial t} = G(x) - R(x) + \frac{1}{q} \frac{\partial J_n(x)}{\partial x}, \tag{2.3}$$

and holes

$$\frac{\partial p}{\partial t} = G(x) - R(x) - \frac{1}{q} \frac{\partial J_p(x)}{\partial x}, \tag{2.4}$$

where $G(x)$ is a sum of generation rates of charge carriers, while $R(x)$ represents sum of all recombination processes. Parameters J_n and J_p represent electron and hole current densities, respectively. Both are described by the sum of drift (associated with an electric field) and diffusion (associated with a gradient of charge carriers concentration) currents for electrons

$$J_n(x) = -qn(x)\mu_n \frac{\partial \varphi}{\partial x} + qD_n \frac{\partial n}{\partial x}, \tag{2.5}$$

and holes

$$J_p(x) = -qp(x)\mu_p \frac{\partial \varphi}{\partial x} - qD_p \frac{\partial p}{\partial x}, \tag{2.6}$$

where $\mu_{n(p)}$ represents the mobility of electrons (holes) and $D_{n(p)}$ is a diffusion coefficient for electrons (holes). The diffusion coefficient can be related to charge carrier mobility with the Einstein relation which can be obtained directly from Equations 2.5 or 2.6. Using the current equation in the equilibrium condition with no current flow and the concept of electrochemical potential, the following (Einstein) relation can be acquired

$$\frac{D_{n(p)}}{\mu_{n(p)}} = \frac{k_B T}{q}, \tag{2.7}$$

where T represents an absolute temperature and k_B is the Boltzmann constant. Therefore, the drift–diffusion current equations can be written for electrons

$$J_n(x) = -qn(x)\mu_n \frac{\partial \varphi}{\partial x} + \mu_n k_B T \frac{\partial n}{\partial x}, \tag{2.8}$$

and for holes

$$J_p(x) = -qp(x)\mu_p \frac{\partial \varphi}{\partial x} - \mu_p k_B T \frac{\partial p}{\partial x} \tag{2.9}$$

within the entire scope of this work. Due to the fact that the model is calculated in time (t) domain, the equation for displacement current density should be also included

$$J_{disp} = \varepsilon_r \varepsilon_0 \frac{\partial F}{\partial t}. \tag{2.10}$$

2.1.3 Ionic charge transport

The equations which describe behavior of ions can be written in the same form as for electrons and holes [51]. Therefore, the continuous equation for anions looks as follows

$$\frac{\partial a}{\partial t} = \frac{1}{q} \frac{\partial}{\partial x} \left(-qa\mu_a \frac{\partial \varphi}{\partial x} + \mu_a k_B T \frac{\partial a}{\partial x} \right) \tag{2.11}$$

while for cations

$$\frac{\partial c}{\partial t} = -\frac{1}{q} \frac{\partial}{\partial x} \left(-qc\mu_c \frac{\partial \varphi}{\partial x} - \mu_c k_B T \frac{\partial c}{\partial x} \right), \tag{2.12}$$

where a and c are densities of anions and cations, respectively. The diffusion coefficients for ionic charge carriers are also correlated with mobilities with the use of Einstein relation. Therefore, above equations are already given with μ_a and μ_c which represent mobilities of

these ions. The currents of anions (J_a) and cations (J_c) are symmetrical as in the case of electrons and holes. There is no generation and recombination processes for ions, therefore the drift–diffusion currents are included in the continuous equations for clarity.

2.1.4 Excitonic transport

The excitons are Coulombically bound electron–hole pairs with a binding energy defining the type of the exciton. The continuity equation for the excitons can be written as

$$\frac{\partial S}{\partial t} = G_S(x) - R_S(x) - \frac{1}{q}\frac{\partial J_s}{\partial x}, \tag{2.13}$$

where $G_S(x)$ and $R_S(x)$ are the sums of generation or recombination rates, respectively. J_s is a current density of excitons given by

$$J_s = -qD_S\frac{\partial S}{\partial x}, \tag{2.14}$$

where S is an exciton concentration and D_S represents a diffusion coefficient of excitons. Here, we could also assume validity of the Einstein relation, however as exciton does not possess any charge, the diffusion coefficient is used instead (a mobility of excitons μ_S might be sometimes taken as an useful parameter). For the same reason, there is only a diffusion part in the current equation with no drift.

2.1.5 Generation profile

In inorganic materials, the generation of charge carriers takes place when a photon of energy higher than a band–gap ($h\nu \geq E_g$) is absorbed by the material. In the simplest scheme, the electron located in a valence band is excited to a conduction band, while a hole appears in the valence band. In molecular materials, the creation of charge carriers can be treated as a two step process. First, a photon excites a molecule to a higher energy level. This molecular exciton can dissociate into seperated electron and hole (see Section 2.1.6).

It is assumed within this work that the generation of charge carriers occurs only in the active (absorber) layer. The different models might be used for defining generation profile and the simplest uses an uniform generation rate within the absorber (G is constant). The uniform generation model is very useful in simulating solar cells [46]. However, in any semiconductor, the absorption of light is the highest at the illuminating side and decreases with a device depth. Therefore, an exponential generation profile, which could be described with the Beer–Lambert model, seems to be a better assumption. However, it lacks of the interface and interference effects which can occur in multilayer device. Therefore, a more precise method of calculating generation profile is the transfer–matrix optical model which takes into account the reflection and transmission effects at each interface which lead to a constructive or destructive interference [52, 56]. In order to calculate a generation profile, two

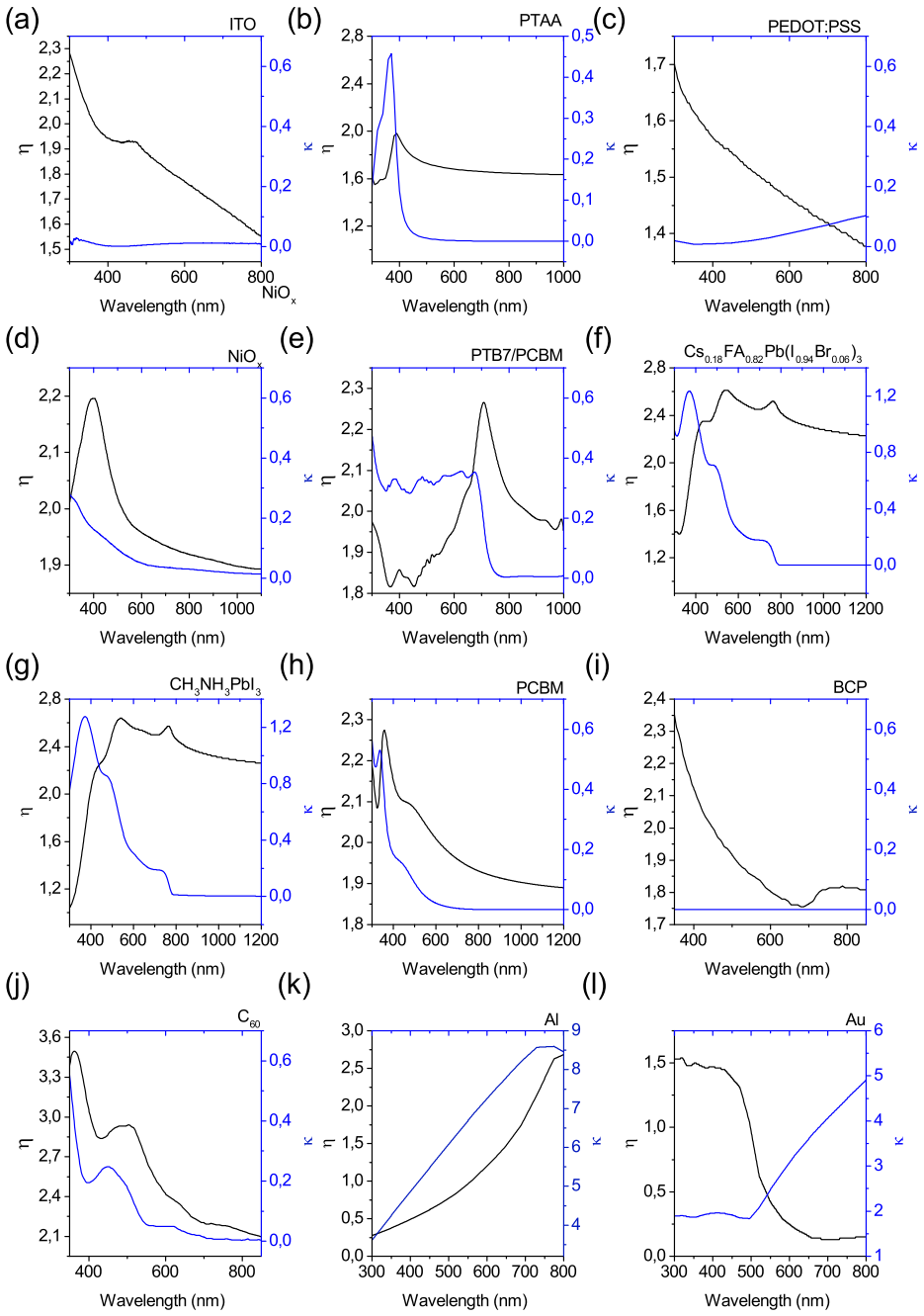

Figure 2.1: The parameters η and κ versus wavelength presented for a) ITO [52], b) PTAA, c) PEDOT:PSS [52], d) NiO_x [53], e) PTB7/PCBM bulk [54], f) $Cs_{0.18}FA_{0.82}Pb(I_{0.94}Br_{0.06})_3$ prepared with gas quenching (GQ), g) $CH_3NH_3PbI_3$ prepared with gas quenching, h) PCBM, i) BCP [55], j) C_{60} [55], k) Al electrode [52], and l) Au electrode [52] materials. If the reference is not given, the sample has been measured in the experiment

optical parameters [an extinction coefficient ("κ) and a refraction index ("η)] are required. Both parameters can be obtained in the experiment and they are widely available in the literature. In the Figure 2.1, there are shown values of both optical parameters versus a wavelength of light used within this work.

2.1.6 Exciton dissociation

The electron and hole which are part of an exciton (or were born from the same exciton) may recombine with each other which is called a geminate recombination. This process can be simply characterized by the rate $R_S = S(x)/\tau_S$, where τ_S is the lifetime of exciton. However, the electron–hole pair may also dissociate, meaning separate to free charge carriers that can freely move within the semiconductor. In organic solar cells, there is much higher probability of exciton formation due to a lower permittivity which leads to an exciton binding energy of approximately 500 meV. This value is much higher than a thermal energy in room temperature [57]. Therefore, it is usually assumed that the generation of free charge carriers in organic solar cells is an effect of a Frenkel–type exciton dissociation process [58]. In general, this mechanism depends on the electric field and temperature. For inorganic materials, the probability of exciton creation is much lower than in organic materials due to a higher dielectric constant which leads to lower exciton binding than the thermal energy in room temperature. Therefore, the generation of charge carriers is assumed to occur directly via band-to-band transition, however the Wannier(–Mott)–type exciton mechanisms may still play an important role in the operation of solar cells, especially in low temperatures [59]. There are many mechanisms of exciton dissociation, but here we focus only on these ones which are applied within this work.

2.1.6.1 Electric field dependent dissociation

A dissociation of Frenkel–type excitons in molecular materials strongly depends on electric field. However, it is also a temperature dependent process. The most popular model used to describe organic solar cells is the Onsager-Braun formalism [60, 61]. Here, the overall exciton dissociation probability can be expressed as [43, 62]

$$D(F) = \int_0^\infty P(F,a)\, F_D(a)\, da, \tag{2.15}$$

where the probability of dissociation P for an exciton separation distance a is given by

$$P(F,a) = \frac{k_{diss}(F)}{k_{diss}(F) + k_f} \tag{2.16}$$

and F_D represents a normalized distribution function which is defined as [43, 62]

$$F_D(a) = \frac{4}{\sqrt{\pi}\, a_0^3}\, a^2 \exp\left(-\frac{a^2}{a_0^2}\right). \tag{2.17}$$

In the above equations k_f is a decay rate of excitons ($k_f = 1/\tau_s$) and a_0 is an initial exciton separation distance. Further, the exciton dissociation rate can be expressed as

$$k_{diss}(F) = \frac{3q}{4\pi\varepsilon_0\varepsilon_r a^3}\left(\mu_n + \mu_p\right)\exp\left(-\frac{E_b}{k_B T}\right)\frac{J_1\left(2\sqrt{-2b}\right)}{\sqrt{-2b}}, \tag{2.18}$$

where J_1 is the first–order Bessel function, E_b is the Coulombic binding energy of the electron–hole pair defined as

$$E_b = \frac{q^2}{4\pi\varepsilon_0\varepsilon_r a} \tag{2.19}$$

and b is the electric field parameter given by

$$b = \frac{q^3 F}{8\pi\varepsilon_0\varepsilon_r k_B^2 T^2}. \tag{2.20}$$

2.1.6.2 Temperature dependent dissociation

The dissociation of Wannier excitons in inorganic materials depends only on temperature. Due to the fact that a binding energy is smaller than the thermal energy, even an energy equal to $k_B T$ should be enough for the dissociation process. Therefore, the rate of exciton dissociation into separated charge carriers can be based on the thermal model [63, 64]

$$k_{diss} = \frac{E_b}{h}\exp\left(-\frac{E_B}{k_B T}\right), \tag{2.21}$$

where h represents the Planck's constant.

2.1.7 Recombination

2.1.7.1 Monomolecular recombination

Figure 2.2(a) presents a scheme of the trap–assisted recombination. The electron (hole) from the conduction (valence) band could be trapped by the impurity or defect states (traps) which are distributed within the band–gap. In general, there are two types of traps based on their positions in the energy scale. The shallow trap is located just below the conduction (above the valence) band within the Urbach tail, however such a trap does not act as a recombination center. The deeper trap state means the location closer to the middle of band–gap, thus it can be treated as a recombination center. The recombination rate for a monomolecular recombination rate is proportional to a concentration of charge carriers ($R_m \propto n$). This rate could be defined using a time dependent occupancy of traps

$$\frac{\partial n_t}{\partial t} = R_{m,n}(x) - R_{m,p}(x), \tag{2.22}$$

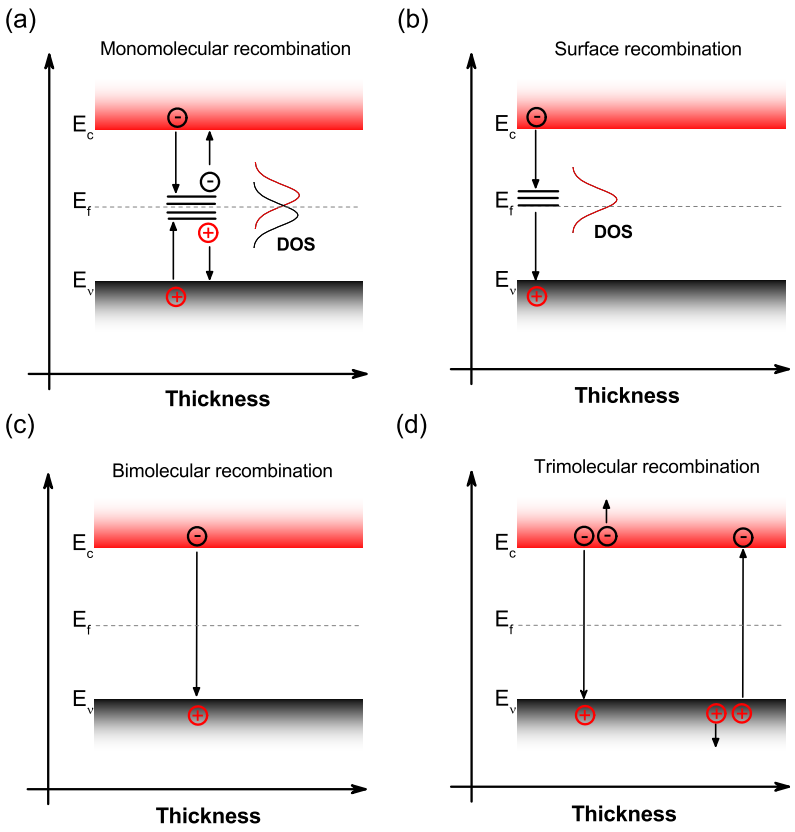

Figure 2.2: Schematic illustration of recombination processes in semiconductor with arrows pointing the direction of electron (hole) transition. Mechanism of (a) trap–assisted monomolecular recombination in the bulk, (b) trap–assisted monomolecular recombination at the surface, (c) bimolecular recombination, and (d) trimolecular recombination

with the recombination rates for electrons

$$R_{m,n}(x) = \frac{1}{\tau_n N_t}\left[n(x)N_t - n_t(x)\left(n(x) + n_1\right)\right], \tag{2.23}$$

and holes

$$R_{m,p}(x) = \frac{1}{\tau_p N_t}\left[n_t(x)\left(p(x) + p_1\right) - N_t p_1\right], \tag{2.24}$$

where n_t is a trap density distribution and N_t represents a trap states density. However, as most of the studies are related with a steady–state condition, and also to increase a computation speed, it is convenient to assume that $\partial n_t/\partial t = 0$, which gives $R_{m,n} = R_{m,p}$. Then Equations 2.23 and 2.24 convert both into the well–known Shockley-Read-Hall (SRH) recombination rate for electrons and holes [65]

$$R_{SRH,n(p)}(x) = \frac{C_n C_p N_t}{C_n \left[n(x) + n_1(E)\right] + C_p \left[p(x) + p_1(E)\right]} \left[n(x)p(x) - n_{int}^2\right], \tag{2.25}$$

where C_n and C_p are charge carrier capture rates for electrons and holes, respectively, defined as $C_{n(p)} = 1/\left(N_t \tau_{n(p)}\right)$ with $\tau_{n(p)}$ as an electron (a hole) lifetime. The energy (E) dependent parameters n_1 and p_1 are given by

$$n_1(E) = N_c \exp\left(-\frac{E_c - E_t}{k_B T}\right), \tag{2.26}$$

$$p_1(E) = N_v \exp\left(-\frac{E_t - E_v}{k_B T}\right), \tag{2.27}$$

$$n_{int} = \left(N_c N_v\right)^{1/2} \exp\left(-\frac{E_g}{2k_B T}\right), \tag{2.28}$$

where N_c and N_v are effective densities of states, E_c and E_v represent edges (energies) of conduction and valence bands, respectively, E_t is a trap energy level which is located in the middle of band–gap ($E_g/2$). The SRH model assumes the trap location in the mid–gap because in this scenario they are the most efficient recombination centers [66]. However, it is not always possible to use a simple model with only one recombination center. In closer to reality scenario, the traps are distributed with different traps energies. Therefore the density of states (DOS) is commonly applied to explain the traps distribution [67, 68]. However, the trap–assisted recombination model needs to sum all the trapped electrons from the conduction band (CBT)

$$R_{m,CBT}(x) = \int_{E_v}^{E_c} \rho_T(E) R_{SRH,n}(E,x) dE \tag{2.29}$$

and holes from the valence band (VBT)

$$R_{m,VBT}(x) = \int_{E_v}^{E_c} \rho_T(E) R_{SRH,p}(E,x) dE, \tag{2.30}$$

where ρ_T is the DOS for traps, and $R_{SRH,n(p)}$ are recombination rates for electrons

$$R_{SRH,n}(E,x) = \frac{C_{nc} C_{pc} N_{tn}}{C_{nc} \left[n(x) + n_1(E)\right] + C_{pc} \left[p(x) + p_1(E)\right]} \left[n(x)p(x) - n_{int}^2\right] \tag{2.31}$$

and holes

$$R_{SRH,p}(E,x) = \frac{C_{nv} C_{pv} N_{tp}}{C_{nv} \left[n(x) + n_1(E)\right] + C_{pv} \left[p(x) + p_1(E)\right]} \left[n(x)p(x) - n_{int}^2\right], \tag{2.32}$$

where, C_{nc} and C_{pc} are trapping and detrapping rates for electrons from the conduction band, respectively, and C_{pv} and C_{nv} represent trapping and detrapping rates for holes from the valence band, respectively. The detrapping processes associated with C_{pc} and C_{nv} are related with capturing of opposite charge carriers. Parameters N_{tn} and N_{tp} represent trap states densities for electrons and holes, respectively. The total recombination can be defined as the sum of both rates $R_m(x) = R_{m,CBT}(x) + R_{m,VBT}(x)$. The DOS function is usually characterized by an exponential density function for shallow traps close to the energy band [69, 70] and a Gaussian density function for deep traps [71]. However, it has been shown that the exponential trap distribution can be also simulated with the Gaussian function [68]. Therefore in this work, ρ_T is only defined with a Gaussian distribution

$$\rho_T(E) = \frac{N_t}{\sqrt{2\pi\sigma_t}} \exp\left[-\frac{[E-(E_c-E_t)^2]}{2\sigma_t^2}\right], \tag{2.33}$$

where σ_t is the width of the distribution.

2.1.7.2 Surface recombination

The trap–assisted monomolecular recombination can occur at the interface (surface) of two layers, as shown in Figure 2.2(b). Then, it is called the surface recombination and its rate may be described by the equation:

$$R_s(x) = \frac{N_t\sigma_s}{\nu_{s,p}^{-1}\left[n(x)+n_1(E)\right] + \nu_{s,n}^{-1}\left[p(x)+p_1(E)\right]}\left[n(x)p(x) - n_{int}^2\right], \tag{2.34}$$

where $\nu_{s,n}$ and $\nu_{s,p}$ are the surface recombination velocities for electrons and holes, respectively. N_t, n_1, p_1 and n_{int} are the same as for the SRH recombination, while L_a represents the absorber thickness as all charge carriers migrate to the interface for extraction, so the surface recombination must be related to the bulk thickness as well. Therefore, the thickness is involved in the equation for the capture cross section.

$$\sigma_s = 1/\left(N_{tn(p)}L_a\right). \tag{2.35}$$

2.1.7.3 Bimolecular recombination

The other possible scenario for the charge carrier recombination is a bimolecular recombination, see Figure 2.2(c), where $R_b \propto n^2$. This mechanism can be easily explained with an electron transition process from the conduction band to the valence band, where this electron recombines with a hole. In molecular materials, such a recombination process occurs when an electron and a hole gets close to each other, within the Coloumbic radius $R_c = q^2/\left(4\pi\varepsilon_0\varepsilon_r k_B T\right)$. As a result, the photon with an energy of band–gap can be emitted, therefore this recombination is usually called a radiative recombination. However, the

bimolecular recombination might be sometimes nonradiative. The recombination rate is well described with the Langevin model

$$R_b(x) = \xi\gamma_L \left[n(x)p(x) - n_{int}^2\right]. \tag{2.36}$$

Here, a recombination reduction factor ($\xi < 1$) has been introduced because it is often needed to fit experimental results [72, 73]. The theoretical explanation of the reduction coefficient is still under debate and many scenarios have been created to explain it [72, 74–76]. The parameter γ_L, which represents a Langevin recombination coefficient can be written as

$$\gamma_L = \frac{q}{\varepsilon_0\varepsilon_r}\left(\mu_n + \mu_p\right), \tag{2.37}$$

2.1.7.4 Trimolecular recombination

The trimolecular recombination of charge carriers can be treated as an Auger process [77]. The Auger mechanism is a non–radiative recombination with the rate proportional to the cube of charge carrier density ($R_t \propto n^3$). Therefore it is mostly dominant only for high charge carrier concentration which occurs for very high illumination of semiconductor. As shown in Figure 2.2(d), this mechanism can be explained with an electron transition from the conduction band to the valence band. However, the excess of the energy is not emitted by photon but instead transferred to other electron (or hole). Further, the third interacting particle may loose an energy in the form of thermal vibrations. Therefore, the mechanism is also called a non–radiative recombination process and it is well explained with the Auger model

$$R_t = \left(\Gamma_n n + \Gamma_p p\right)\left(np - n_{int}^2\right), \tag{2.38}$$

where Γ_n and Γ_p are trimolecular recombination constants for electrons and holes, respectively.

2.2 Boundary conditions

The solar cell device is a sandwich structure with metal electrode contacts at the bottom and top of the cell. These contacts are responsible for the injection and/or extraction mechanisms of charge carriers. Thus, their mathematical description is important to define boundary conditions for the numerical model. We may use the following terminology (if not stated otherwise) to define cathode ($x = 0$) and anode at ($x = L$) electrodes. The contacts are the source of a built–in potential (V_{built}) which in great extent influences the simulation of operating solar cell. Therefore, the boundary conditions for the electric potential are given by

$$\varphi(0) = V_{built} - V_a,\ \varphi(L) = 0, \tag{2.39}$$

where V_a represents the applied voltage and on the anode it is numerically set to zero. For charge carrier concentrations, we assume the Schottky contacts at both sides. Therefore, for the cathode

$$n(0) = N_c \exp\left(\frac{-\varphi_n}{k_B T}\right),\ p(0) = N_v \exp\left(\frac{\varphi_n - E_g}{k_B T}\right), \tag{2.40}$$

and for the anode

$$n(L) = N_c \exp\left(\frac{\varphi_p - E_g}{k_B T}\right),\ p(L) = N_v \exp\left(\frac{-\varphi_p}{k_B T}\right), \tag{2.41}$$

where φ_n and φ_p are work functions for both electrodes. In the absence of excitonic injection from contacts, it is convenient to assume a total annihilation of excitons at the contacts. Therefore, the concentrations of excitons at both electrodes are

$$S(0) = 0, \quad S(L) = 0. \tag{2.42}$$

If injection currents are neglected, then boundary conditions for the electron and hole current densities can be written as

$$J_n(0) = 0, \quad J_n(L) = 0, \quad J_p(0) = 0, \quad J_p(L) = 0. \tag{2.43}$$

The time boundary conditions ($t = 0$) for concentrations of electrons and holes are assumed to be zero. However, for the case of ion densities, we should note that ions cannot migrate outside the active layer of the material. Thus, initial densities of anions and cations are

$$a\,(t = 0) = N_0, \quad c\,(t = 0) = N_0. \tag{2.44}$$

In addition, the change of ions concentrations at both electrodes can be defined as

$$\left.\frac{\partial a}{\partial x}\right|_{x=0,L} = 0, \quad \left.\frac{\partial c}{\partial x}\right|_{x=0,L} = 0, \tag{2.45}$$

which is consistent with an assumption of isolating layers for ions diffusion outside the active layer.

2.3 Interface effects

The injection barrier influences the charge carrier concentration at the interfaces of the sandwich solar cell strucutre. Therefore, to account for energy variations, the generalized potential method is used [78–80]. This method assumes calculation of a potential in every discrete position of the solar cell for electrons and holes

$$\hat{\varphi}_{n(p)}(x) = \varphi(x) - \theta_{n(p)}(x)/q, \tag{2.46}$$

where $\varphi(x)$ is the Poisson potential calculated from Equation 2.1. The terms θ_n and θ_p are band parameters related to a spatial energetic alignment of all layers in solar cell for electrons

$$\theta_n(\vec{x}) = E_c(\vec{x}) - E_{c,act} - k_B T \ln\left(\frac{N_c(\vec{x})}{N_{c,act}}\right) \tag{2.47}$$

and holes

$$\theta_p(\vec{x}) = E_v(\vec{x}) - E_{v,act} + k_B T \ln\left(\frac{N_v(\vec{x})}{N_{v,act}}\right). \tag{2.48}$$

The band parameters are different for each material, therefore they have been described with $(\vec{x})$ notation [79]. The energies of band edges $E_{c,act}$, $E_{v,act}$ and the effective densities of states $N_{c,act}$, $N_{v,act}$ denote quantities for the active layer. The generalized potential is used in the drift–diffusion system of equations, and also for the electric field calculations

$$F_{n(p)}(x) = -\frac{\partial \hat{\varphi}_{n(p)}(x)}{\partial x}. \tag{2.49}$$

The energy levels change in space due to variations of charge carrier concentrations, therefore they are calculated as follows for the conduction band

$$E_c(x) = E_c(\vec{x}) - q\varphi(x) \tag{2.50}$$

and for the valence band

$$E_v(x) = E_v(\vec{x}) - q\varphi(x). \tag{2.51}$$

The quasi–Fermi levels are given for electrons

$$E_{fn}(x) = E_c(x) + k_B T \ln\left(\frac{n}{N_c}\right) \tag{2.52}$$

and holes

$$E_{fp}(x) = E_v(x) - k_B T \ln\left(\frac{p}{N_v}\right). \tag{2.53}$$

2.4 Implementation of the model

The drift–diffusion model is discretized with the Scharfetter–Gummel [81] method and solved with a C++ language self–written program. The detailed codes are available in the repository, see the website https://github.com/dglowienka/drift-diffusion. The code for the

transfer–matrix model has been adopted from https://web.stanford.edu/group/mcgehee/. In the following section, first the discretized equations are given with the scaling procedure for them. Subsequently, the algorithm used for the numerical model is described with its implementation. Finally, the confrontation of the numerical and analytical results is presented.

2.4.1 Discretization procedure

The discreatization is performed with the finite difference method. Therefore, the discretized form of the Poisson equation for the electric potential distribution looks as follows

$$\begin{aligned}&\frac{1}{\frac{h_i+h_{i-1}}{2}}\left[\frac{\varepsilon_i+\varepsilon_{i+1}}{2}\varphi_{i+1}^{t+1}-\left(\frac{\varepsilon_i+\varepsilon_{i+1}}{2h_i}+\frac{\varepsilon_{i-1}+\varepsilon_i}{2h_{i-1}}\right)\varphi_i^{t+1}+\frac{\varepsilon_{i-1}+\varepsilon_i}{2h_{i-1}}\varphi_{i-1}^{t+1}\right]=\\&=-\frac{q}{\varepsilon_0}\rho_i^t\end{aligned} \tag{2.54}$$

while an electric field distribution is given by

$$F_i^t=-\frac{\varphi_{i+1}^t-\varphi_i^t}{h_i}. \tag{2.55}$$

The general potentials are also calculated but as they do not need discretization, they are not mentioned here. Also, the variation of permittivity and mobility at the interface led to discretization of these two variables as well [82]. Moreover, the equation is calculated for the non–uniform grid to enhance the speed of calculation by reducing the number of points. Using an irregular grid, we are able to increase number of points at the interface where the most abrupt changes of charge carrier concentrations are observed. To acquire such a spatial grid for the simulated cell, it is defined with a Chebyshev polynomial. First, we calculate a parameter

$$x_k=\cos\left(\frac{2k-1}{2N}\pi\right), \tag{2.56}$$

where k is a number of each iteration point, $x_k\in[-1,1]$ and N represents number of pointes. Second, it is necessary to scale x_k to x_i by recalculation it from the interval $[-1,1]$ to $[0,L]$

$$x_i=-\frac{L\,(x_k-1)}{2}. \tag{2.57}$$

Finally, the difference in grid points is defined as

$$h_i=x_{i+1}-x_i. \tag{2.58}$$

The continuous equations for electrons, holes and excitons are

$$\frac{n_i^{t+1}-n_i^t}{\Delta t}=G_i-R_i+\frac{1}{q}\frac{k_BT}{\frac{h_i+h_{i-1}}{2}}\left\{\frac{\mu_{n,i}+\mu_{n,i+1}}{2h_i}B\left[\frac{q}{k_BT}\left(\varphi_{i+1}^{t+1}-\varphi_i^{t+1}\right)\right]n_{i+1}^{t+1}+\right.$$
$$-\left[\frac{\mu_{n,i}+\mu_{n,i+1}}{2h_i}B\left[\frac{q}{k_BT}\left(\varphi_i^{t+1}-\varphi_{i+1}^{t+1}\right)\right]+\frac{\mu_{n,i-1}+\mu_{n,i}}{2h_{i-1}}B\left[\frac{q}{k_BT}\left(\varphi_i^{t+1}-\varphi_{i-1}^{t+1}\right)\right]\right]n_i^{t+1}+$$
$$\left.\frac{\mu_{n,i-1}+\mu_{n,i}}{2h_{i-1}}B\left[\frac{q}{k_BT}\left(\varphi_{i-1}^{t+1}-\varphi_i^{t+1}\right)\right]n_{i-1}^{t+1}\right\},\tag{2.59}$$

$$\frac{p_i^{t+1}-p_i^t}{\Delta t}=G_i-R_i+\frac{1}{q}\frac{k_BT}{\frac{h_i+h_{i-1}}{2}}\left\{\frac{\mu_{p,i}+\mu_{p,i+1}}{2h_i}B\left[\frac{q}{k_BT}\left(\varphi_i^{t+1}-\varphi_{i+1}^{t+1}\right)\right]p_{i+1}^{t+1}+\right.$$
$$-\left[\frac{\mu_{p,i}+\mu_{p,i+1}}{2h_i}B\left[\frac{q}{k_BT}\left(\varphi_{i+1}^{t+1}-\varphi_i^{t+1}\right)\right]+\frac{\mu_{p,i-1}+\mu_{p,i}}{2h_{i-1}}B\left[\frac{q}{k_BT}\left(\varphi_{i-1}^{t+1}-\varphi_i^{t+1}\right)\right]\right]p_i^{t+1}+$$
$$\left.\frac{\mu_{p,i-1}+\mu_{p,i}}{2h_{i-1}}B\left[\frac{q}{k_BT}\left(\varphi_i^{t+1}-\varphi_{i-1}^{t+1}\right)\right]p_{i-1}^{t+1}\right\},\tag{2.60}$$

and

$$\frac{S_i^{t+1}-S_i^t}{\Delta t}=G_{S,i}-R_{S,i}+\frac{1}{q}\frac{k_BT}{\frac{h_i+h_{i-1}}{2}}\left[\frac{\mu_{S,i}+\mu_{S,i+1}}{2h_i}\left(S_{i+1}^{t+1}-S_i^{t+1}\right)-\frac{\mu_{S,i-1}+\mu_{S,i}}{2h_{i-1}}\left(S_i^{t+1}+S_{i-1}^{t+1}\right)\right],\tag{2.61}$$

respectively. The continuity equations for anions and cations can be written as

$$\frac{a_i^{t+1}-a_i^t}{\Delta t}=\frac{1}{q}\frac{\mu_a k_BT}{\frac{h_i+h_{i-1}}{2}}\left\{\frac{1}{h_i}B\left[\frac{q}{k_BT}\left(\varphi_{i+1}^{t+1}-\varphi_i^{t+1}\right)\right]a_{i+1}^{t+1}-\right.$$
$$\left[\frac{1}{h_i}B\left[\frac{q}{k_BT}\left(\varphi_i^{t+1}-\varphi_{i+1}^{t+1}\right)\right]+\frac{1}{h_{i-1}}B\left[\frac{q}{k_BT}\left(\varphi_i^{t+1}-\varphi_{i-1}^{t+1}\right)\right]\right]a_i^{t+1}+\tag{2.62}$$
$$\left.\frac{1}{h_{i-1}}B\left[\frac{q}{k_BT}\left(\varphi_{i-1}^{t+1}-\varphi_i^{t+1}\right)\right]a_{i-1}^{t+1}\right\}$$

and

$$\frac{c_i^{t+1}-c_i^t}{\Delta t}=\frac{1}{q}\frac{\mu_c k_B T}{\frac{h_i+h_{i-1}}{2}}\left\{\frac{1}{h_i}B\left[\frac{q}{k_B T}\left(\varphi_i^{t+1}-\varphi_{i+1}^{t+1}\right)\right]c_{i+1}^{t+1}-\right.$$
$$\left[\frac{1}{h_i}B\left[\frac{q}{k_B T}\left(\varphi_{i+1}^{t+1}-\varphi_i^{t+1}\right)\right]+\frac{1}{h_{i-1}}B\left[\frac{q}{k_B T}\left(\varphi_{i-1}^{t+1}-\varphi_i^{t+1}\right)\right]\right]c_i^{t+1}+ \quad (2.63)$$
$$\left.\frac{1}{h_{i-1}}B\left[\frac{q}{k_B T}\left(\varphi_i^{t+1}-\varphi_{i-1}^{t+1}\right)\right]c_{i-1}^{t+1}\right\},$$

where $B(z)$ is a Bernoulli function, which is defined as follows

$$B(z)=\frac{z}{e^z-1}. \quad (2.64)$$

2.4.2 Scaling

Table 2.1: Scaling factors for the drift–diffusion model

Description	Scaling quantity	Scaling factor	Unit
Space position	x_c	10^{-9}	m
Time	t_c	$\frac{x_c^2 q}{\mu_{max} k_B T}$	s
Carrier concentration	N_{car}	$\frac{\varepsilon_0 \varepsilon_{max} k_B T}{q^2 x_c^2}$	m^{-3}
Relative permittivity	ε_{max}	100	–
Mobility	μ_{max}	10^{-2}	$m^2\,V^{-1}\,s^{-1}$
Potential	φ_c	$\frac{k_B T}{q}$	V
Electric field	F_c	$\frac{k_B T}{q x_x}$	$V\,m^{-1}$
Current density	J_c	$\frac{N_{car}\mu_{max} k_B T}{x_c}$	$A\,m^{-2}$
Recombination/generation	B_c	$\frac{N_{car}}{t_c}$	$m^{-3}\,s^{-1}$
Energy	E_c	$k_B T$	J

Scaling procedure is an extremely useful technique in numerical modeling to reduce the number of constants, to make all variables dimensionless, and therefore to decrease numerical error and increase the computational speed. Therefore, we have decided to scale all equations within the numerical program. The scaling system needs scaling factors [83]. All of them are given in the Table 2.1. For clarity, only few scaled equations are shown. The Poisson equation is now in the following form

$$\frac{1}{\frac{\overline{h}_i+\overline{h}_{i-1}}{2}}\left[\frac{\overline{\varepsilon}_i+\overline{\varepsilon}_{i+1}}{2}\overline{\varphi}_{i+1}^{t+1}-\left(\frac{\overline{\varepsilon}_i+\overline{\varepsilon}_{i+1}}{2\overline{h}_i}+\frac{\overline{\varepsilon}_{i-1}+\overline{\varepsilon}_i}{2\overline{h}_{i-1}}\right)\overline{\varphi}_i^{t+1}+\frac{\overline{\varepsilon}_{i-1}+\overline{\varepsilon}_i}{2\overline{h}_{i-1}}\overline{\varphi}_{i-1}^{t+1}\right]=-\overline{\rho}_i^t. \quad (2.65)$$

The continuous equations for electrons, holes and excitons are now given as

$$\frac{\overline{n}_i^{t+1}-\overline{n}_i^t}{\overline{\Delta t}} = \overline{G}_i - \overline{R}_i + \frac{1}{\frac{\overline{h}_i+\overline{h}_{i-1}}{2}}\left\{\frac{\overline{\mu}_{n,i}+\overline{\mu}_{n,i+1}}{2\overline{h}_i}B\left(\overline{\varphi}_{i+1}^{t+1}-\overline{\varphi}_i^{t+1}\right)\overline{n}_{i+1}^{t+1} + \right.$$
$$-\left[\frac{\overline{\mu}_{n,i}+\overline{\mu}_{n,i+1}}{2\overline{h}_i}B\left(\overline{\varphi}_i^{t+1}-\overline{\varphi}_{i+1}^{t+1}\right)+\frac{\overline{\mu}_{n,i-1}+\overline{\mu}_{n,i}}{2\overline{h}_{i-1}}B\left(\overline{\varphi}_i^{t+1}-\overline{\varphi}_{i-1}^{t+1}\right)\right]\overline{n}_i^{t+1}+,$$
$$\left.\frac{\overline{\mu}_{n,i-1}+\overline{\mu}_{n,i}}{2\overline{h}_{i-1}}B\left(\overline{\varphi}_{i-1}^{t+1}-\overline{\varphi}_i^{t+1}\right)\overline{n}_{i-1}^{t+1}\right\} \tag{2.66}$$

$$\frac{\overline{p}_i^{t+1}-\overline{p}_i^t}{\overline{\Delta t}} = \overline{G}_i - \overline{R}_i + \frac{1}{\frac{\overline{h}_i+\overline{h}_{i-1}}{2}}\left\{\frac{\overline{\mu}_{p,i}+\overline{\mu}_{p,i+1}}{2\overline{h}_i}B\left(\overline{\varphi}_i^{t+1}-\overline{\varphi}_{i+1}^{t+1}\right)\overline{p}_{i+1}^{t+1} + \right.$$
$$-\left[\frac{\overline{\mu}_{p,i}+\overline{\mu}_{p,i+1}}{2\overline{h}_i}B\left(\overline{\varphi}_{i+1}^{t+1}-\overline{\varphi}_i^{t+1}\right)+\frac{\overline{\mu}_{p,i-1}+\overline{\mu}_{p,i}}{2\overline{h}_{i-1}}B\left(\overline{\varphi}_{i-1}^{t+1}-\overline{\varphi}_i^{t+1}\right)\right]\overline{p}_i^{t+1}+,$$
$$\left.\frac{\overline{\mu}_{p,i-1}+\overline{\mu}_{p,i}}{2\overline{h}_{i-1}}B\left(\overline{\varphi}_i^{t+1}-\overline{\varphi}_{i-1}^{t+1}\right)\overline{p}_{i-1}^{t+1}\right\} \tag{2.67}$$

and

$$\frac{\overline{S}_i^{t+1}-\overline{S}_i^t}{\overline{\Delta t}} = \overline{G}_{S,i}-\overline{R}_{S,i}+\frac{1}{\frac{\overline{h}_i+\overline{h}_{i-1}}{2}}\left[\frac{\overline{\mu}_{S,i}+\overline{\mu}_{S,i+1}}{2\overline{h}_i}\left(\overline{S}_{i+1}^{t+1}-\overline{S}_i^{t+1}\right)-\frac{\overline{\mu}_{S,i-1}+\overline{\mu}_{S,i}}{2\overline{h}_{i-1}}\left(\overline{S}_i^{t+1}+\overline{S}_{i-1}^{t+1}\right)\right], \tag{2.68}$$

The same scaling form are used for anions and cations. Also, the mechanisms of generation, recombination and dissociation for charge carriers and excitons are scaled. However, there is only a slight difference in the form of these equations, therefore they are not presented here.

2.4.3 Algorithm

Even if we are mainly interested in the steady–state condition, the following algorithm for numerical drift–diffusion model is given also for the transient condition. The reason is that the transient simulations can be applied for deeper analysis. Also, such simulations could be sometimes used after a steady–state condition is reached. One of the example is an illumination of a solar cell with pulses of light which is one of the protocol used for our simulations. Here, the generation rate is first set to zero ($G = 0$) and the simulations last until the steady–state is achieved. At this moment, charge carriers are at thermodynamical equilibrium. Afterwards, the sunlight is turned on ($G \neq 0$) and each iteration is recorded [84]. The other

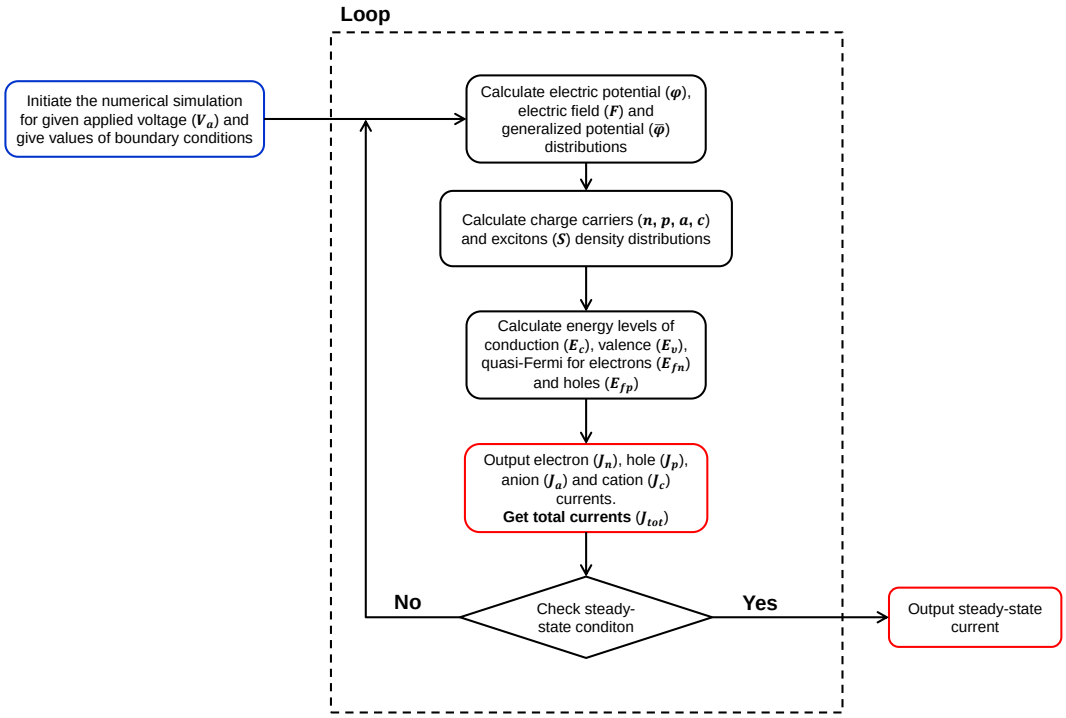

Figure 2.3: The implemention algorithm for the drift–diffusion numerical model.

procedure is simulating until the steady–state condition is reached for a given applied voltage. As a result, the current–voltage (J–V) characteristics are obtained.

The basic algorithm used for a single steady–state condition is shown in Figure 2.3. At first, the initial variables are given, including loading the physical parameters and setting the boundary conditions for space and time. Forward in time in the loop, there are calculated unknown variables for the next time iteration $(t+1)$ with the knowledge of values from current time (t). Then, the potential, the generalized potential and electric field distributions are calculated. Using these parameters, the charge carrier and exciton densities can be found, and also the related energy levels. At last, the partial currents are calculated and summed up to get the total current

$$\begin{aligned} J(x,t) =& qE\left(n\mu_n + p\mu_p + a\mu_a + c\mu_c\right) + \\ &+ k_B T\left(\mu_n\frac{\partial n}{\partial x} - \mu_p\frac{\partial p}{\partial x} + \mu_a\frac{\partial a}{\partial x} - \mu_c\frac{\partial c}{\partial x}\right) + \\ &+ \varepsilon_0\varepsilon_r\frac{\partial E}{\partial t} \end{aligned} \tag{2.69}$$

in every space position. To obtain the total current for simulated solar cell, the current density is averaged throughout the device. At this point, all the calculations are done for this

time iteration, therefore the steady–state condition can be found. The convergence condition for numerical calculations can be expressed with different numerical methods. One is related with the rate of change for each variable. It shows how the given value has changed in comparison to the previous time iteration. In other method, the total current variation is calculated or checked if the displacement current is closer to zero in time. In this work, only the total current method is used as it includes all the variations by themselves. Therefore, the steady–state condition can be calculated as follows

$$\left| \frac{J_{total}^{t+1} - J_{total}^{t}}{J_{total}^{t}} \right| \leqslant C, \tag{2.70}$$

where C represents a given threshold, here typically used 10^{-6}.

2.5 Verification with analytical solution

The numerical solution of the drift–diffusion is not an exact solution but gives much more flexibility in analysis of different scenarios. However, the complexity of the differential equations may lead to errors in discretization procedure or simply in the code itself. Therefore, it is always good to compare the numerical model with an analytical solution. But finding exact solution for the drift–diffusion system of equations is only possible for a specific situation. One of the useful analytical model is the space charge limited current (SCLC) model, where a flow of charge carriers is not limited by injection processes but only with conductivity of the semiconductor. The drift–diffusion current equation for holes has no direct solution due to its nonlinear form, see Equation 2.9. However, when solving for high electric fields, the diffusion part has a negligible influence, and therefore this equation could be rewritten to

$$J_p = qp(x)\mu_p F(x), \tag{2.71}$$

with an electric field (F) distribution instead of a potential. The Poisson equation is now in the following form

$$\frac{\partial F}{\partial x} = \frac{q}{\varepsilon_0 \varepsilon_r} p(x). \tag{2.72}$$

Equations 2.71 and 2.72 gives together

$$J_p = \varepsilon_0 \varepsilon_r \mu_p F(x) \frac{\partial F}{\partial x}, \tag{2.73}$$

Next, we will integrate the above equation to calculate the average currents. The electric field distribution, when integrated, gives

$$\int_0^L F(x)dx = V, \tag{2.74}$$

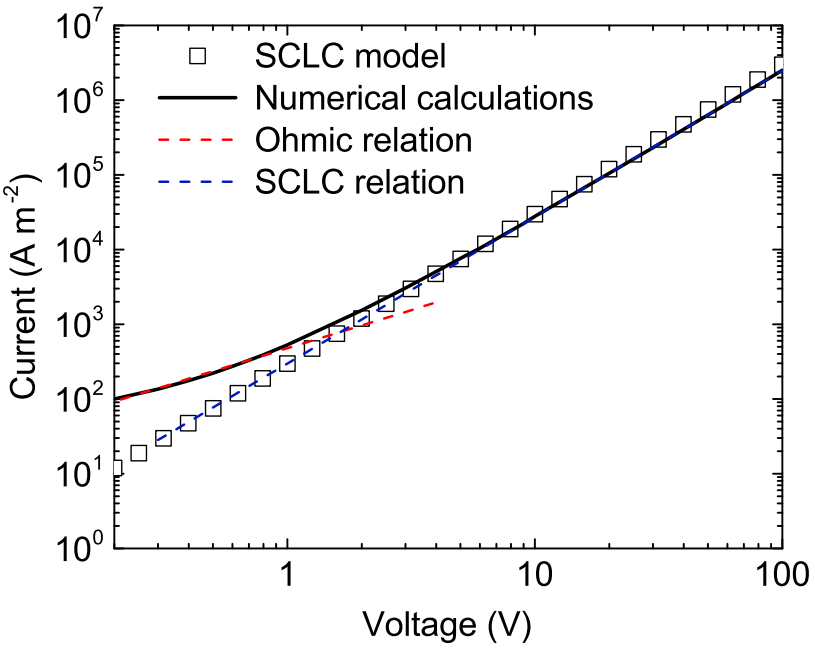

Figure 2.4: The simulation results for SCLC analytical model (square symbols) and drift–diffusion model (black solid line). The parameters used are $\mu_p = 10^{-8}$ m^2 V^{-1} s^{-1}, $\varepsilon_r = 3$, $L = 100$ nm.

with V as a voltage across the semiconductor. The hole density at the electrode is assumed to be very high, which can be written in the form

$$p(x) \to \infty, \quad F(0) = 0. \tag{2.75}$$

All together gives the SCLC current

$$J_p = \frac{9}{8}\varepsilon_r\varepsilon_0\mu_p\frac{V^2}{L^3}. \tag{2.76}$$

Figure 2.4 shows the results obtained from the SCLC model and from the drift–diffusion numerical calculation. It is observed that at low voltage, there is a discrepancy between two models. However, at higher applied potential, both models are comparable. Here, there are two regions which can be explained with SCLC and ohmic behaviors. In the model, it is assumed no injection barrier, thus at the ohmic region, the slope is with order of 1 ($J \propto V$). However, at higher voltage, the SCLC starts to dominate and the order of slope increases to 2 ($J \propto V^2$). This agrees well with the assumption that the SCLC model works only in specific conditions, whereas the drift–diffusion model resemble semiconductor operation much more accurately. What is more, the numerical model is validated and can be further used as a tool for the thesis.

Chapter 3

Influence of excitons interaction with charge carriers in organic solar cells

Excitonic processes are of great importance for organic solar cells [37, 38]. In contrast to inorganic materials, the mechanism which leads to photogeneration of charge carriers occurs as a consequence of excitons dissociation into separated electrons and holes. Recently, the annihilation of excitons on charge carriers has been intensively studied in organic light–emitting diodes [85–91], organic solar cells [75, 92–99] and organic light–emitting transistors [100]. It is believed that this process should give a significant contribution to the loss of efficiency of these organic optoelectronic devices, especially for a high excitation densities [95, 101]. Therefore, this chapter contains studies on the annihilation of excitons on charge carriers which may occur in organic solar cells [102]. Considering a simple explanation of this phenomenon, a hole (an electron), which is a part of an exciton interacts with a free electron (hole). As a consequence, both opposite sign charge carriers annihilate and an electron (a hole) from the exciton turns into a free carrier. If we take into account a quantum mechanical description of this process, an energy of the quenched exciton is fully transferred to the interacting carrier via the Förster resonance energy transfer. As a result, the exciton is fully quenched. For both scenarios of this effect, a concentration of excitons decreases but concentrations of free electrons and holes are still the same.

In the first section, we investigate steady–state simulations to understand an influence of the annihilation rate constants on the operation of organic solar cells. Next, we demonstrate the role of annihilation on the photovoltaic parameters with spatial simulations. Further, we will focus on the transient photocurrents which allow to investigate the dynamics of charge carriers generation mechanisms. In the next part, we discuss an influence of nonuniform generation profile obtained from the optical model. Finally, the role of interfaces in the modeling of organic solar cells will be presented.

This chapter is partially based on [D. Głowienka, J. Szmytkowski *Influence of Excitons Interaction with Charge Carriers on Photovoltaic Parameters in Organic Solar Cells*, Chem. Phys. **503** (2018) 31–38] and [D. Głowienka, J. Szmytkowski *Modeling of Transient Photocurrent in Organic Semiconductors Incorporating the Annihilation of Excitons on Charge Carriers*, Acta Phys. Pol. A **132** (2017) 397–400].

3.1 Theoretical model and parameters for the investigated device

First, it should be mentioned about assumptions used in the presented model. Similarly to earlier numerical studies [43–46, 103–105], the recombination of charge carriers is treated only as a bimolecular process. For simplicity, thermionic and excitonic injection currents from electrodes are not taken into account. According to the Lambert–Beer law, the intensity of light decreases exponentially due to absorption. This effect causes that most of light is absorbed near illuminated surface. Thus, it is convenient to assume that an illumination is uniform in the whole volume of a very thin sample what leads to a constant value of an exciton generation rate (G_S). However, in further part of this chapter the numerical model will be extended to implement a nonuniform generation profile.

Excitons can interact with trapped and free (predominantly slow) charge carriers or ex-

Table 3.1: The parameters used in simulations, if not specified otherwise.

Parameter	Symbol	Numerical value
Temperature	T	293 K
Length of a photoactive material [106]	L	100 nm
Relative permittivity [105]	ε_r	3.9
Mobility of electrons	μ_n	2.8×10^{-7} m^2 V^{-1} s^{-1}
Mobility of holes	μ_p	5.2×10^{-8} m^2 V^{-1} s^{-1}
Recombination reduction factor	ξ	10^{-2}
Diffusion of excitons	D_S	2.53×10^{-9} m^2 s^{-1}
Exciton binding energy [105]	E_b	105.5 meV
Exciton lifetime [107]	τ_s	1×10^{-5} s
Energy band–gap	E_g	1.22 eV
Schottky barrier height for cathode	φ_n	0.15 eV
Schottky barrier height for anode	φ_p	0.15 eV
Exciton generation rate [106]	G_S	9.79×10^{27} m^{-3} s^{-1}
Effective density of states in conduction band [43, 105]	N_c	2.5×10^{25} m^{-3}
Effective density of states in valence band [43, 105]	N_v	2.5×10^{25} m^{-3}
Built–in voltage	V_{built}	0.8 V
Spatial grid	Δx	2 nm
Temporal grid	Δt	0.5 ns

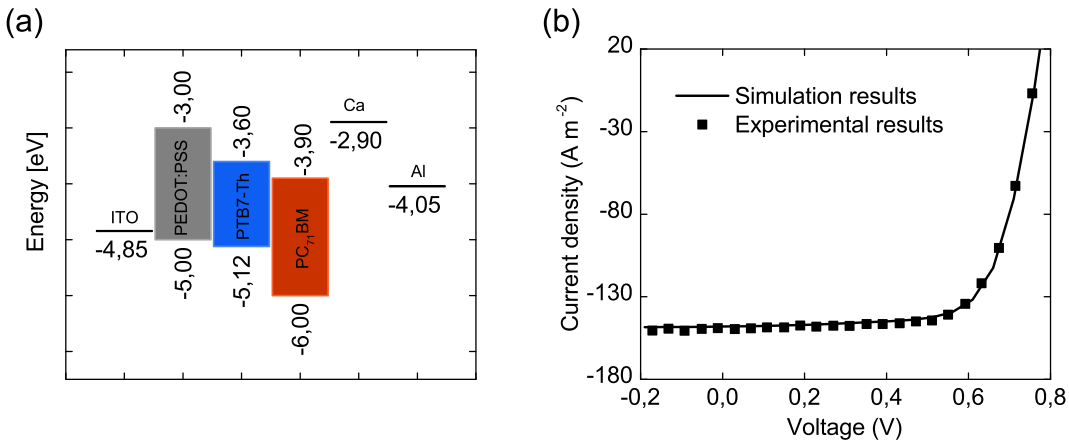

Figure 3.1: (a) Schematic illustration of energy level diagram for organic solar cell with PTB7–Th:$PC_{71}BM$ as absorber, (b) numerical (solid line) and experimental (squares) results of current density as a function of voltage for PTB7–Th:$PC_{71}BM$. The experimental points for J–V characteristics are extracted from literature [106]. Parameters used in calculations: $\xi = 5\times10^{-2}$, $\mu_s = 1.2\times10^{-8}$ m^2 V^{-1} s^{-1}. The process of annihilation is not considered in this fit.

citons themself. All the mechanisms are characterized by different rate constants. However, we have decided to neglect the exciton–exciton interaction. It has been also demonstrated experimentally that an annihilation rate constant for the exciton–trapped charge carrier interaction can be even three orders of magnitudes lower than an annihilation rate constant which describes the exciton–free carrier interaction in the same material (anthracene) [108]. Therefore we decided to ignore trapping and detrapping effects in our calculations.
Continuity equations for excitons, electrons and holes are given by relations

$$\frac{\partial S}{\partial t} = G_S + \frac{1}{4}R_B - \frac{S}{\tau_s} - k_{diss}(F)\,S - \gamma_{ns}nS - \gamma_{ps}pS - \frac{1}{q}\frac{\partial J_s}{\partial x}, \tag{3.1}$$

$$\frac{\partial n}{\partial t} = k_{diss}(F)\,S - R_B + \frac{1}{q}\frac{\partial J_n}{\partial x} \tag{3.2}$$

and

$$\frac{\partial p}{\partial t} = k_{diss}(F)\,S - R_B - \frac{1}{q}\frac{\partial J_p}{\partial x}, \tag{3.3}$$

which are based on Equations 2.13, 2.3 and 2.4, respectively. The parameters γ_{ns} and γ_{ps} are the second order rate constants for the annihilation of excitons on electrons and holes, respectively. In this work, the results obtained for symmetric $\gamma_{ns} = \gamma_{ps}$ will be presented, therefore $\gamma_{n(p)s}$ is used instead.

The electric field dependent exciton dissociation rate $k_{diss}(F)$ has been chosen from the Onsager–Brown model, see Equation 2.18. The only recombination mechanism of charge

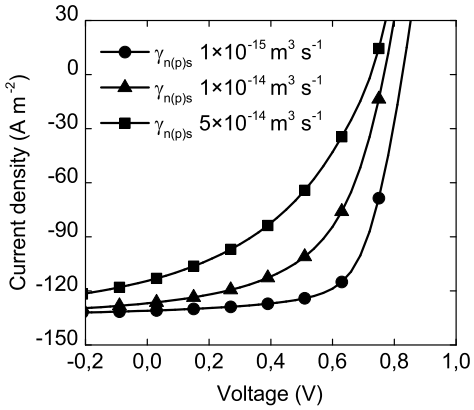

Figure 3.2: Numerical results of current density as a function of voltage. Circles, triangles and squares denote the annihilation rate constants $\gamma_{n(p)s}$ equal to 10^{-15}, 10^{-14} and 5×10^{-14} m^3 s^{-1}, respectively.

carriers is bimolecular (see Section 2.1.7.3), where a term with a factor 1/4 in Equation 3.1 is a consequence of an assumption that 25% of recombining electrons and holes form excitons [44]. It should be noted that terms with the rate constants γ_{ns} and γ_{ps} are not included in Equations 3.2 and 3.3 because the concentrations of free charge carriers do not change directly in the process of excitons annihilation. The electron, hole and exciton currents are given in Equations 2.8, 2.9 and 2.14, respectively.
A local electric potential is found from the Poisson equation (see Section 2.1.1)

$$\frac{\partial^2 \varphi}{\partial x^2} = -\frac{q}{\varepsilon_0 \varepsilon_r} (p - n) . \tag{3.4}$$

A detailed implemention procedure is presented in Chapter 2. All parameters used in the simulation are listed in Table 3.1. If a reference is given in Table 3.1, it means that the parameter is fixed. The Schottky barrier heights, an energy band–gap and a built–in voltage have been taken from an energy level diagram which is presented in Fig. 3.1. The mobilities of charge carriers were treated as free parameters in the fitting procedure. However, their final values are close to the magnitudes reported in literature [43, 105, 106, 109]. A validity of the model and electrical parameters has been proved by fitting of an experimental J–V characteristics (AM 1.5G illumination, room temperature) extracted from the literature [106]. This fit is presented in Fig. 3.1. It should be noted that the exciton annihilation on charge carriers has not been considered here ($\gamma_{n(p)s} = 0$) because such a process was not taken into account in the interpretation of these experimental results [106]. However, we were also able to achieve a satisfactory fit when these annihilation parameters were not equal to zero (not shown here).

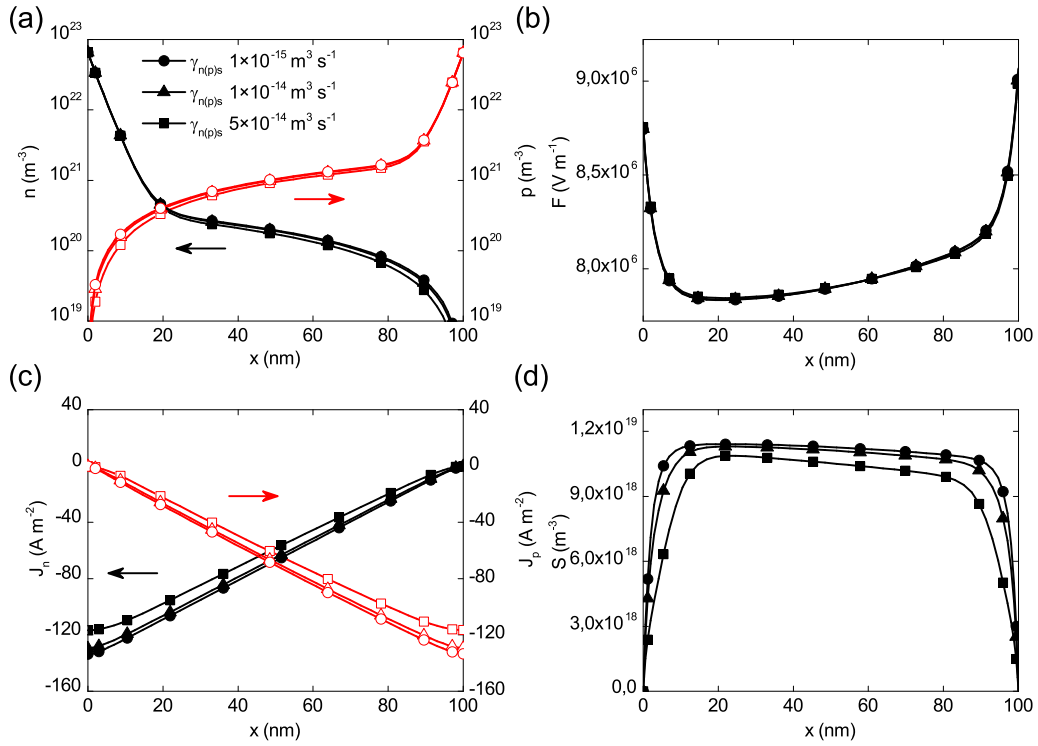

Figure 3.3: Numerical results calculated for short–circuit current (J_{sc}) with different annihilation rate constants. a) spatial distributions of electrons and holes b) electric field distribution, c) current densities for electrons and holes versus distance from cathode, and d) a spatial distribution of excitons. Results of simulations are plotted as lines with symbols. Circles, triangles and squares denote the $\gamma_{n(p)s}$ equal to 10^{-15}, 10^{-14} and 5×10^{-14} m^3 s^{-1}, respectively. Closed and open symbols in parts (a) and (c) are used for electrons and holes, respectively.

3.2 Spatial simulation results

The magnitudes of the rates $\gamma_{n(p)s}$ are in very wide ranges, usually between 10^{-18}–10^{-15} m^3 s^{-1}. Recently, it has been reported that the parameter γ_{ps} can achieve a value of 3×10^{-14} m^3 s^{-1} for the material which is often used in organic photovoltaics (P3HT) [92]. Therefore, a similar maximal values of the annihilation are used in our simulations. Also, we have decided not to plot the results obtained for the annihilation rate constants lower than 10^{-15} m^3 s^{-1} because this annihilation does not impact the operation of organic solar cell. Figure 3.2 illustrates the total current density versus voltage calculated for different rates of annihilation. It is clearly seen that the shapes of J–V characteristics significantly change. Therefore, this effect influences other photovoltaic parameters as well, which will be demonstrated in further part of this chapter. The three characteristic points are analyzed, a short–circuit current (J_{sc}), an open–circuit voltage (V_{oc}) and a maximum power point (MPP).

We observe that the current density reaches larger values of the short–circuit current J_{sc}

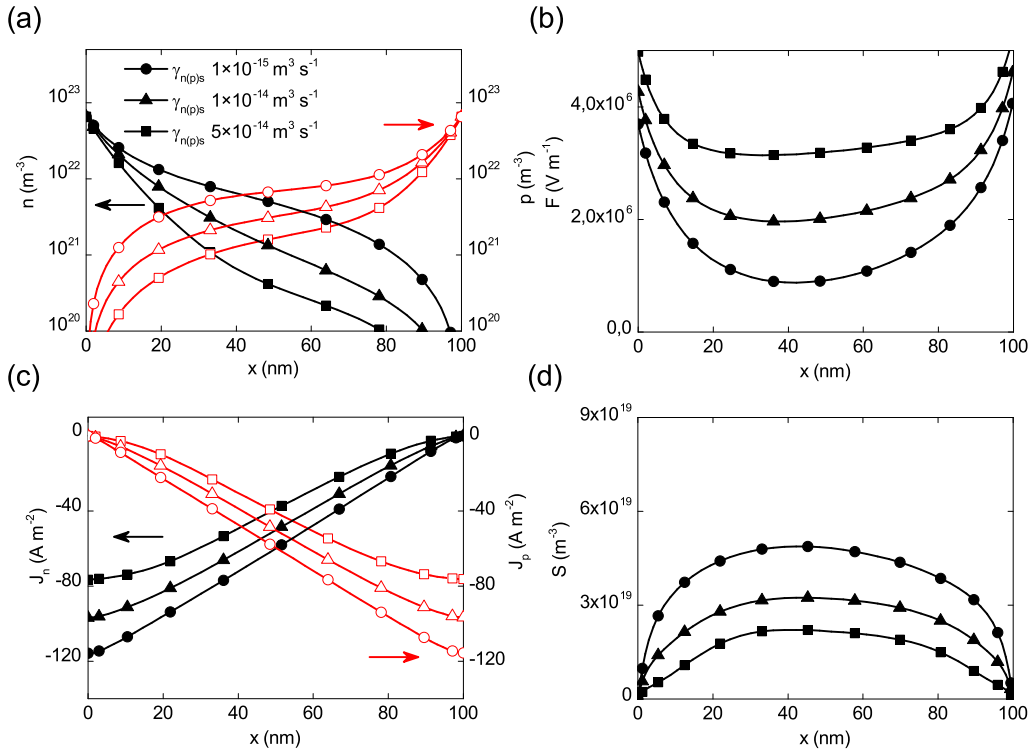

Figure 3.4: Numerical results calculated for maximum power point (MPP) with different annihilation rate constants. a) spatial distributions of electrons and holes, b) electric field distribution, c) current densities for electrons and holes versus distance from cathode, and d) a spatial distribution of excitons. Results of simulations are plotted as lines with symbols. Circles, triangles and squares denote the $\gamma_{n(p)s}$ equal to 10^{-15}, 10^{-14} and 5×10^{-14} m^3 s^{-1}, respectively. Closed and open symbols in parts (a) and (c) are used for electrons and holes, respectively.

for lower magnitudes of the rate constants. Therefore, an influence of the annihilation rate constant at the short–circuit (SC) conditions is presented in Figure 3.3. Figure 3.3(a) demonstrates spatial distributions of charge carriers. Due to differences between the mobilities of electrons and holes, we observe that the hole density is around one order of magnitude larger than the density of electrons. The increasing of annihilation rate constant causes a slight drop of the concentrations n and p. The small change in charge carrier concentration leads to negligible variation of electric field for different annihilation rates, see Figure 3.3(b). Figure 3.3(c) presents spatial distributions of current components for electrons (J_n) and holes (J_p). Both distributions exhibit linear dependencies in the bulk of organic material. This result has been explained as a consequence of large internal electric field at SC conditions [43, 105]. Our simulations indicate that higher values of annihilation cause a monotonic decreasing of $|J_n|$ and $|J_p|$. Figure 3.3(d) illustrates that the density of excitons S also decreases for larger annihilation rate due to higher probability of the exciton annihilation process. It causes that less excitons can dissociate into separated charge carriers. Consequently, lower concentrations

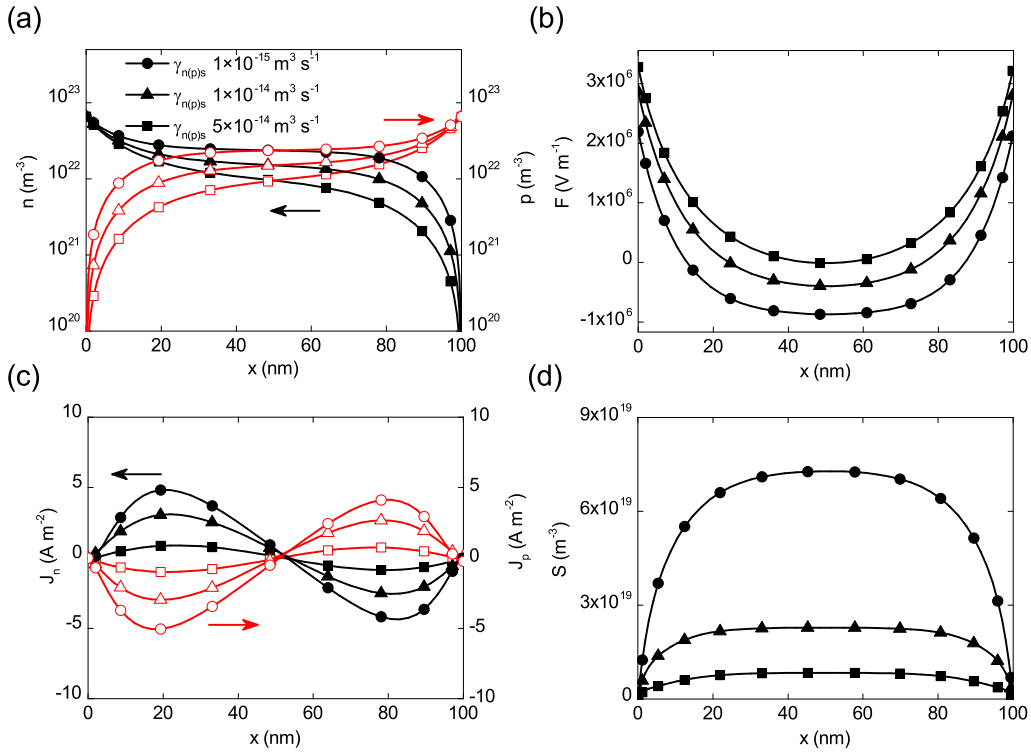

Figure 3.5: Numerical results calculated for open–circuit voltage V_{oc} with different annihilation rate constants. a) spatial distributions of electrons and holes, b) electric field distribution, c) current densities for electrons and holes versus distance from cathode, and d) a spatial distribution of excitons. Results of simulations are plotted as lines with symbols. Circles, triangles and squares denote the $\gamma_{n(p)s}$ equal to 10^{-15}, 10^{-14} and 5×10^{-14} m^3 s^{-1}, respectively. Closed and open symbols in parts (a) and (c) are used for electrons and holes, respectively.

of electrons and holes are observed. We can see that different charge carrier mobilities lead to an asymmetrical shape of $S(x)$ curve. In our calculations $\mu_n > \mu_p$, therefore the probability of the excitons annihilation on charge carriers increases for slower holes. We should note that other calculations carried out for $\mu_n = \mu_p$ led to symmetrical tendency of the $S(x)$ function (not shown here).

The next characteristic point to be analyzed is a maximum power point (MPP), where the solar cell usually operates under normal conditions. The impact of excitons annihilation is much more visible here. Figure 3.4(a) shows that a total charge carrier density is decreasing for higher annihilation rate constant. The assymetry of electron and hole concentrations originates from differences in mobilities, however this effect is much less visible than in short–circuit current. The obtained profile of electric field is a result of differences in charge carrier concentration, see Equation 3.4. Therefore, it has the highest magnitude at the contacts, where the most abrupt changes are observed, see Figure 3.4(b). Variations of the charge carrier concentration and the electric field impacts the diffusion and drift currents, respectively.

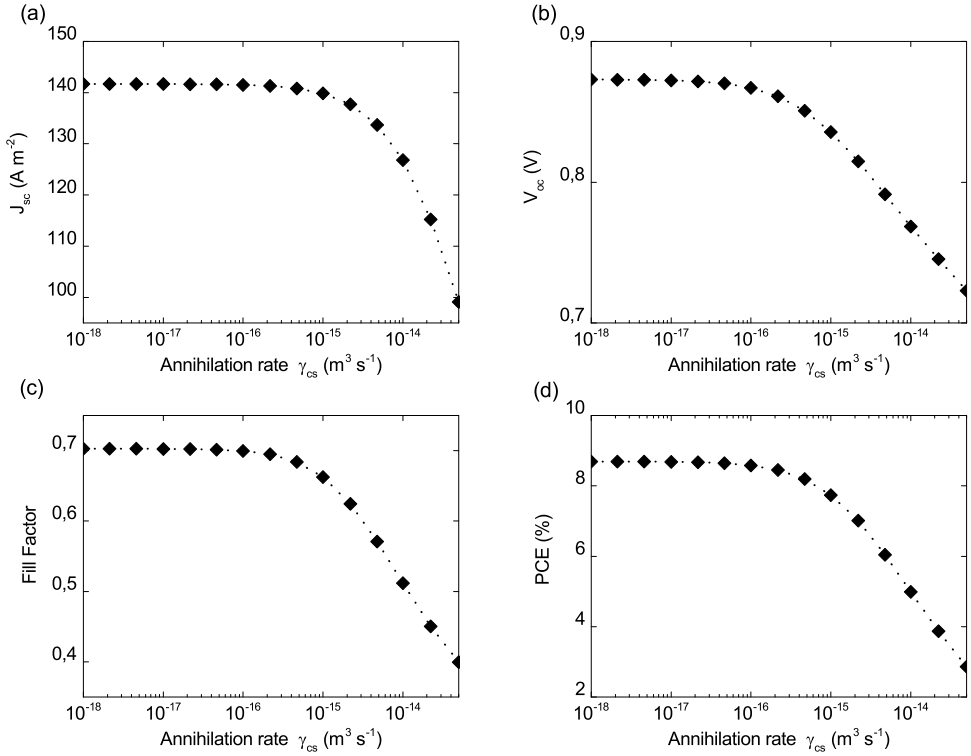

Figure 3.6: Numerical results for a) short–circuit current, b) open–circuit voltage, c) fill factor, and d) power conversion efficiency as a function of annihilation rate constant ($\gamma_{ns} = \gamma_{ps}$). Dotted lines are plotted as guides for the eye.

In Figure 3.4(c), the electron and hole current distributions are presented. We can see that the total photocurrent is getting lower for higher annihilation rate. The same effect is observed for partial currents which decrease monotonically. The exciton concentration follows the same tendency as observed previously. Figure 3.4 demonstrates that the exciton density increases proportionally with $\gamma_{n(p)S}$. The small asymmetry of the exciton concentration is due to higher mobility of electrons which leads to a shift toward the cathode.

Figure 3.5 shows an influence of the annihilation on an open–circuit (OC) and is organized in the same manner as Figures 3.3 and 3.4 with the same annihilation rate constants. Figure 3.5(a) illustrates the electron and hole densities as a function of a distance from electrodes. In contrast to the case of SC and MPP, we observe symmetrical curves with respect to the middle of a sample. Such a behavior has been reported in previous steady–state drift–diffusion studies [43]. As a result, we observe the symmetrical electric field distribution, see Figure 3.5(b). The increase of annihilation rate causes a visible drop of both concentrations in the bulk of sample. A total current density is equal to zero for an open–circuit voltage V_{oc}. Therefore, the currents J_n and J_p have opposite signs and they are symmetrical about the zero axis, as shown in Figure 3.5(c). Figure 3.5(d) demonstrates a distribution of excitons

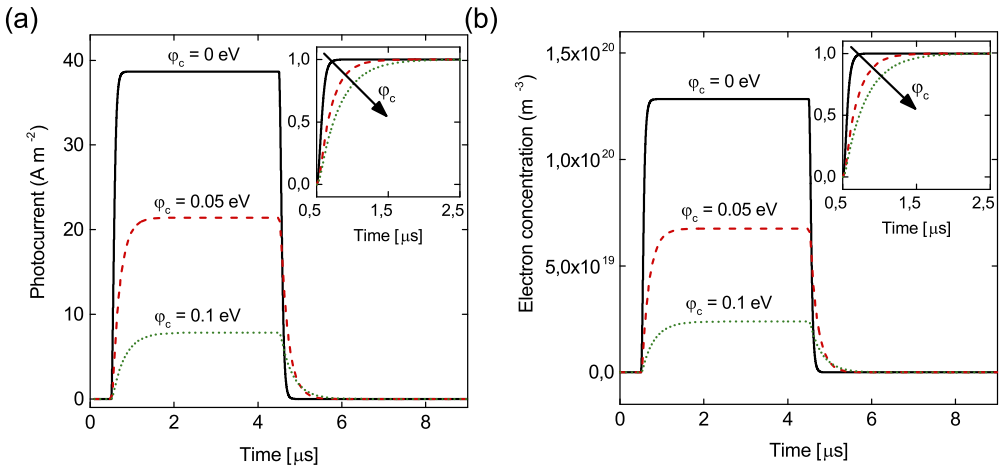

Figure 3.7: Transient photocurrent (a) and concentration of electrons versus time (b) both calculated with different injection barrier heights in the absence of annihilation process. Excitons mobility is equal to 10^{-7} m^2 V^{-1} s^{-1} for both cases. The vertical axes in insets show values of normalized photocurrent (a) and normalized concentration (b).

in space. We observe a symmetrical distribution of the $S(x)$ curve which is a consequence of symmetrical behavior of charge carriers concentrations. The calculations clearly illustrate that the density S decreases for higher rate of annihilation due to more efficient interaction of excitons with electrons and holes in the bulk of sample.

Figure 3.6 shows a short–circuit current (J_{sc}), an open–circuit voltage (V_{oc}), a fill factor (FF) and a power conversion efficiency (PCE) plotted as a function of annihilation rate. We can see that these parameters are constant for exciton annihilation rate lower than 10^{-16} m^3 s^{-1}. If the annihilation rate constant reaches the range 10^{-16}–10^{-15} m^3 s^{-1}, then all photovoltaic parameters start to decrease monotonically. For an open–circuit voltage V_{oc}, an almost linear decreasing (in semi–log plot) is observed. Figure 3.6(d) presents that a magnitude of PCE has dropped about a several percent. When we take into account that annihilation is equal to 3×10^{-14} m^3 s^{-1} for P3HT, commonly used in polymer photovoltaics, then the conclusion is that the process of excitons annihilation on charge carriers is not a beneficial phenomenon for polymer solar cells.

3.3 Transient simulation results

The parameters used for the transient simulations are shown in Table 3.2. For simplicity, we consider the same values of Schottky barrier heights for electrons (φ_n) and holes (φ_p). Also, the same mobilities and equal magnitudes of annihilation rate constants are chosen for both types of charge carriers. It causes that the transient concentration profiles are similar for both electrons and holes. Depending on the injection barrier height, the Schottky ($\varphi_{n(p)} \neq 0$) and the Ohmic ($\varphi_{n(p)} = 0$) contacts are defined. The model is solved forward in time with turn–

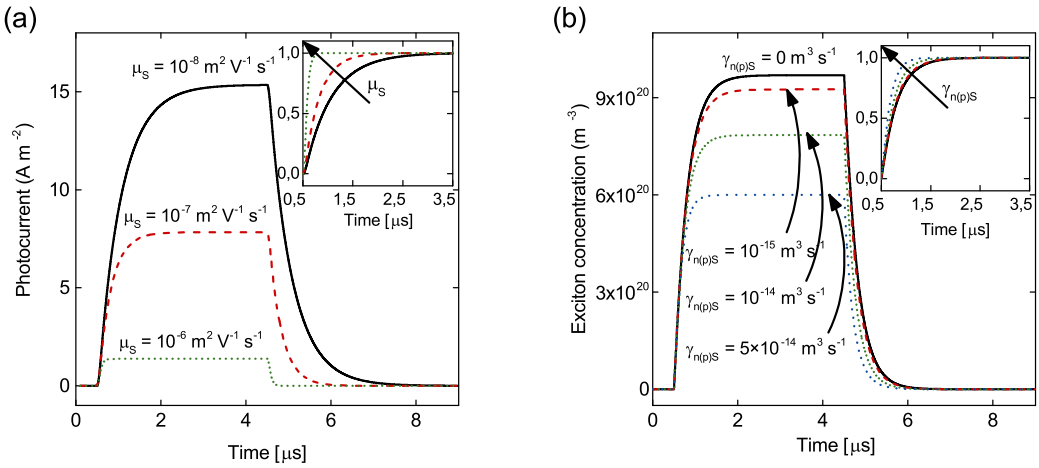

Figure 3.8: Transient photocurrent without annihilation process for different mobilities of excitons (a) and concentration of excitons as a function of time for varied annihilation rates with $\mu_S = 10^{-7}$ m^2 V^{-1} s^{-1} (b). Results of simulation are plotted for injection barrier equal to 0.1 eV. The vertical axes in insets show values of normalized photocurrent (a) and normalized concentration (b).

on method, see Section 2.4.3. First, the dark currents ($G_S = 0$) are simulated for 0.5 μs and then sample is illuminated with uniform G_S for 4 μs. Finally, the dark conditions are simulated up to 9 μs.

The terms, which describe the annihilation process in Equation 3.1, depend on three parameters: charge carriers concentration, excitons concentration and annihilation rate constants. Therefore, we will analyze how these parameters influence on transient photocurrents. The results are presented in the middle of material, because the dynamics of photocurrent is independent on the position. In addition, we decided to illustrate obtained results using both absolute and normalized scales in all presented figures.

Table 3.2: The different parameters used in the transient simulations in respect to Table 3.1.

Parameter	Symbol	Numerical value
Length of a photoactive material	L	120 nm
Relative permittivity	ε_r	3.4
Mobility of electrons and holes	$\mu_{n(p)}$	10^{-7} m^2 V^{-1} s^{-1}
Exciton binding energy	E_b	325.8 meV
Exciton lifetime	τ_s	1×10^{-6} s
Energy band–gap	E_g	0.8 eV
Exciton generation rate	G_S	2.7×10^{27} m^{-3} s^{-1}
Built–in voltage	V_{built}	1.34 V

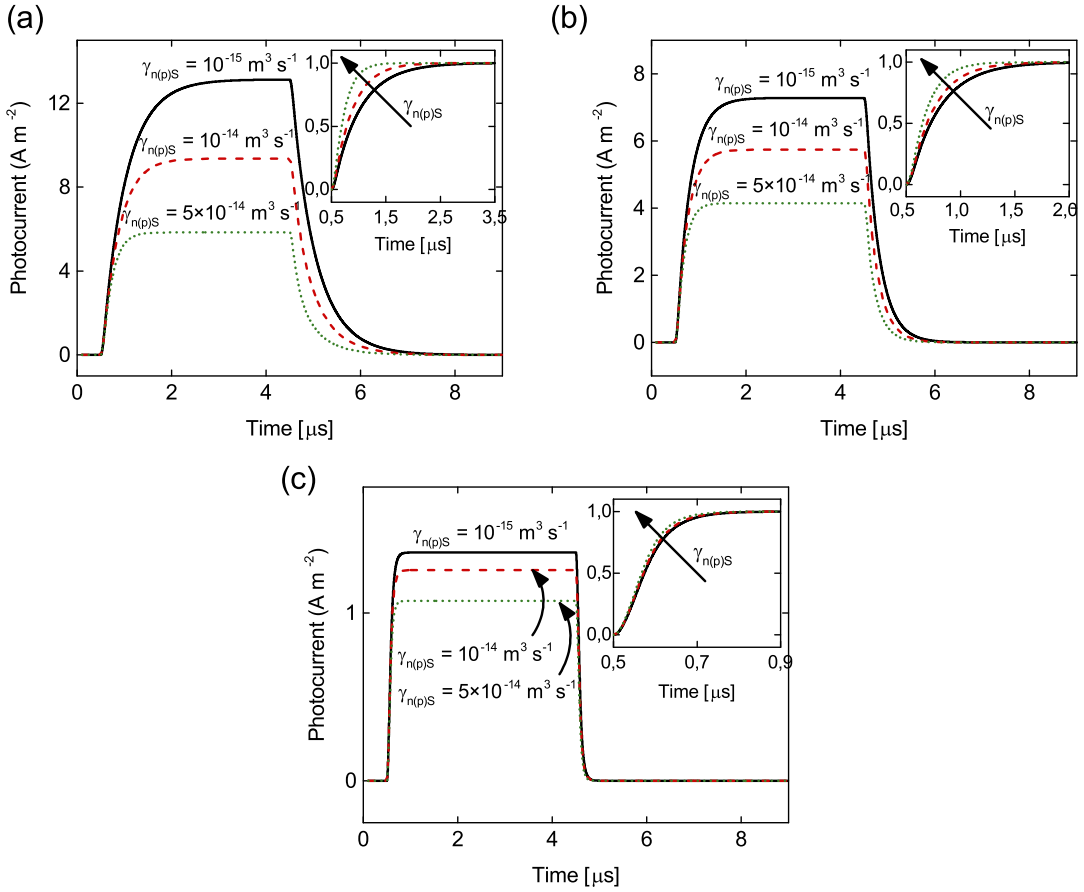

Figure 3.9: Transient photocurrent for different mobilities of excitons calculated for three annihilation rate constants. Excitons mobility equals to a) 10^{-8} m^2 V^{-1} s^{-1}, b) 10^{-7} m^2 V^{-1} s^{-1}, and c) 10^{-6} m^2 V^{-1} s^{-1}. The height of injection barrier for Schottky contacts is equal to 0.1 eV. The vertical axes in insets show normalized photocurrent.

Figure 3.7(a) shows transient photocurrents calculated for different injection barrier heights. We can see that a lowering of injection barrier leads to an increasing of photocurrent magnitude. The rise time is the shortest (0.2 μs) for Ohmic contact and increases for Schottky contacts (up to 0.64 μs for 0.1 eV). The explanation is that $\varphi_{n(p)}$ impacts directly on the concentration of charge carriers, as shown in Figure 3.7(b). The annihilation of excitons gives no visible influence on the dynamics of photocurrent for Ohmic contacts due to short rise times (not shown). Thus, next simulations are carried out only for Schottky contacts.

Figure 3.8(a) demonstrates the impact of excitons mobility on transient photocurrents. We can see that the magnitude of photocurrent is lower for higher μ_S. This result may be explained by the effect of charge carriers photogeneration due to the excitons dissociation. If the mobility is higher, the concentration of excitons decreases and, as a consequence, the pho-

tocurrent is getting lower. Apart from the photocurrent magnitude, the influence of exciton mobility on photocurrent's dynamics is visible [inset in Figure3.8(a)]. When the mobility of excitons is higher, then the dynamics is much faster. The rise time is equal to 0.23 μs for $\mu_S = 10^{-6}$ m^2 V^{-1} s^{-1} and increases up to 0.84 μs for $\mu_S = 10^{-8}$ m^2 V^{-1} s^{-1}. The concentration of excitons as a function of time is presented in Figure 3.8(b) for different values of annihilation rate constants. We can see that the annihilation process causes a decreasing of the S magnitude. The lowering concentration of excitons should lead to faster response of photocurrent, because less number of excitons dissociates into seperated charge carriers and the steady–state condition is achieved faster.

Figure 3.9 shows the influence of annihilation process on the dynamics of photocurrent calculated for different exciton mobilities. For each mobility, the annihilation rate is given for three values: low (10^{-15} m^3 s^{-1}), moderate (10^{-14} m^3 s^{-1}) and high (5×10^{-14} m^3 s^{-1}). We can see that the impact of excitons annihilation is the most evident for the lowest mobility ($\mu_S = 10^{-8}$ m^2 V^{-1} s^{-1}). In this case, the rising time is 0.83 μs for the lowest value of $\gamma_{n(p)S}$ and decreases to 0.53 μs when the probability of annihilation increases [inset in Figure 3.9(b)]. If the mobility of excitons is $\mu_S = 10^{-7}$ m^2 V^{-1} s^{-1}, we observe lower response of the annihilation to photocurrent's dynamics. Here, the rising time is equal to 0.62 μs for very low annihilation rate constant, and reaches a value of 0.45 μs when $\gamma_{n(p)S}$ increases, see Figure 3.9(b). For the mobility of excitons equal to 10^{-6} m^2 V^{-1} s^{-1}, the variation of annihilation rate changes the rise time of photocurrent negligibly, as shown in the inset of Figure 3.9(c).The obtained results demonstrate that the annihilation process has the highest impact for structures with lower exciton mobility and higher (the Schottky-type) injection barrier.

3.4 Influence of nonuniform generation profile

In previous sections, we have used the uniform generation profile as an approximation of the absorption of light within a thin organic material. However, an exact exciton distribution, which influences the generation of charge carriers is relevant for our studies. Therefore, a role of a nonuniform generation will be discussed in this part of the chapter. Although a Lambert-Beer law is predominantly used to describe an absorption of light within a sample, we have decided to use the transfer matrix model to calculate the generation profile G_S, see Section 2.1.5. This model needs much more efforts to be applied, however it gives more precise results. The optical parameters for ITO, PEDOT:PSS, PTB7–Th:$PC_{71}BM$ and Al are shown in Figure 2.1.

Figure 3.10(a) shows the calculated generation profile and the region of numerical simulation is focused only on the absorber layer of PTB7–Th:$PC_{71}BM$ in the solar cell. The illumination side of the cell is at the ITO electrode which is an anode contact situated in a position $x = L$. In this chapter, the interface effects are neglected assuming that the PEDOT:PSS material has the same electric potential levels as the interface of the absorber and the anode contact. It could be noticed that the highest generation appears not at the illu-

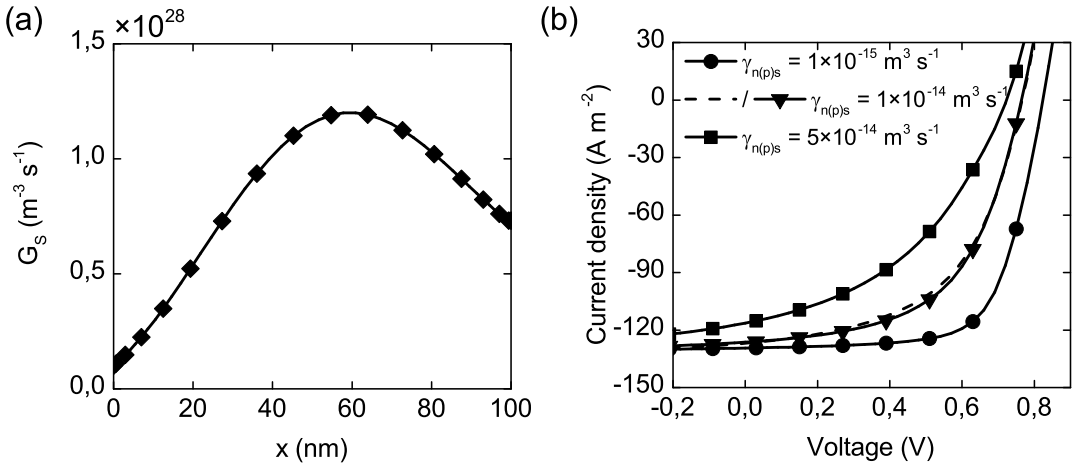

Figure 3.10: Numerical results for nonuniform generation profile. a) Generation profile used in the simulation, b) current density as a function of voltage. Circles, triangles and squares denote the annihilation rate constants ($\gamma_{ns} = \gamma_{ps}$) equal to 10^{-15}, 10^{-14} and 5×10^{-14} m^3 s^{-1}, respectively. The dashed line represents results for uniform generation profile and $\gamma_{n(p)s}$ equal to 10^{-14} m^3 s^{-1}.

mination side but is shifted toward a middle of the absorber. It proves that an exponential Lambert–Beer law cannot explain all the absorption effects, especially for thin organic films. Figure 3.10(b) demonstrates that a nonuniform generation profile has a small influence on the operation of this organic solar cell. It is visible that, for simulations with the same annihilation rate (10^{-14} m^3 s^{-1}) obtained from uniform and nonuniform generation profile, the changes of voltage–current characteristics are very weak. The only observed shift appears at MPP, therefore further analysis will be focused on that point.

Figure 3.11 demonstrates spatial distribution results for different annihilation rates obtained with nonuniform generation profile. It should be noticed that electron and hole distributions are slightly changed only in the region of a low charge carrier concentration [Figure 3.11(a)]. However, this variation is weak and almost does not impact the electric field distribution, see Figure 3.11(b). As discussed before for a case of uniform generation, the current distribution within an absorber layer monotonically decreases for both charge carriers. However, for a nonuniform G_S, the current distribution starts to resemble a generation profile itself, Figure 3.11(c). The tendency of decreasing total photocurrent for increasing annihilation rate is consistent with our previous results. Figure 3.11(d) presents exciton distributions within the solar cell. It is visible that the concentration of exciton is shifted toward anode, where a higher illumination is observed. However, the integration of the excitons distribution over a space dimension, causes that the densities for both types of generation profile are about the same. This suggests that the use of uniform generation is a good approximation in modeling and gives the same explanation of exciton annihilation role in this organic solar cell.

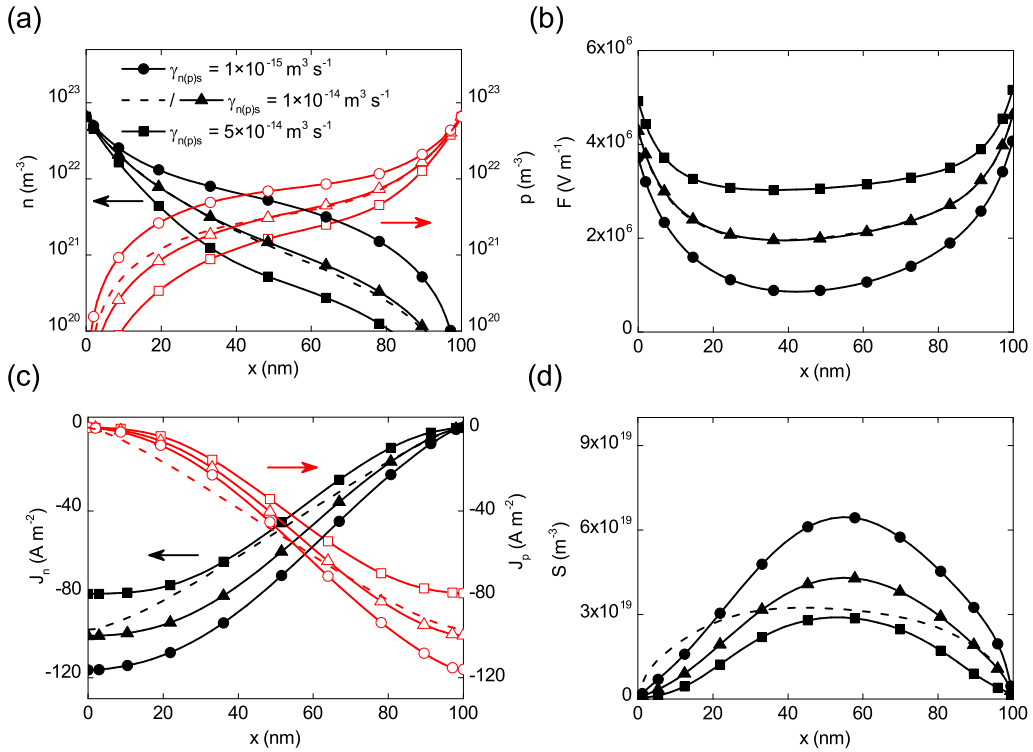

Figure 3.11: Numerical results calculated for a maximum power point MPP with different annihilation rate constants. a) spatial distributions of electrons and holes, b) electric field distribution, c) current densities for electrons and holes versus distance from cathode, and d) a spatial distribution of excitons. Results of simulations are plotted as lines with symbols. Circles, triangles and squares denote the $\gamma_{n(p)s}$ equal to 10^{-15}, 10^{-14} and 5×10^{-14} m^3 s^{-1}, respectively. Closed and open symbols in parts (a) and (c) are used for electrons and holes, respectively. The dashed line represents results for uniform generation profile and $\gamma_{n(p)s}$ equal to 10^{-14} m^3 s^{-1}.

3.5 On the impact of interfaces

In order to analyze the effect of interfaces on exciton annihilation, the drift–diffusion model has been extended to simulate both PTB7–Th:PC$_{71}$BM and PEDOT:PSS layers. Interfaces between the layers lead to numerical difficulties, therefore the variation of permittivity has been included in the Poisson equation [82], see Equation 3.4. In addition energy levels for electron and hole transporting layers are not aligned which creates injection barriers and drastically influences the final performance of solar cell, see Figure 3.1(a). Thus, the method of generalized potentials has been used to include these variations, see Section 2.3.

Figure 3.12(a) demonstrates the generation profile calculated with the transfer–matrix method. Here, the PEDOT:PSS (green layer), is treated as a layer with no photogeneration of charge carriers in there. Therefore, excitons are still analyzed only within the absorber, however the interface effects in between two organic layers are not omitted. We can see that the interfaces have a drastic effect on the operation of this solar cell, see Figure 3.12(b). Although,

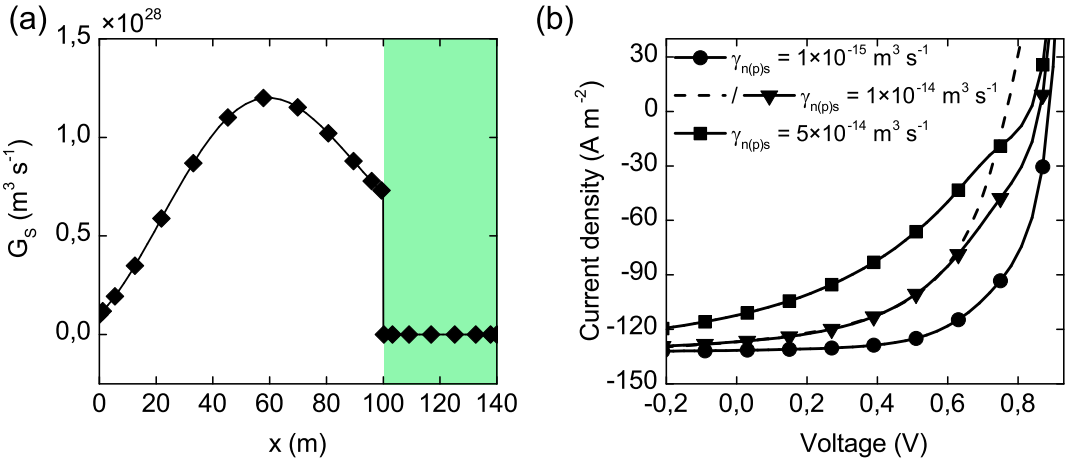

Figure 3.12: Numerical results for interface impact. a) Generation profile used in the simulation, and b) current density as a function of voltage. Circles, triangles and squares denote the annihilation rate constants ($\gamma_{ns} = \gamma_{ps}$) equal to 10^{-15}, 10^{-14} and 5×10^{-14} m^3 s^{-1}, respectively. The dashed line represents results with uniform generation profile and without interfaces, where $\gamma_{n(p)s}$ is equal to 10^{-14} m^3 s^{-1}.

the J_{sc} and MPP characteristic points practically do not change, the V_{oc} changes visibly. Also, the shape of J–V characteristics starts to resemble S–shape [110] for higher annihilation rates. Such an effect has been already explained with interface phenomena which stays in compliance with our results [111]. In the further part of this chapter, we will focus only on the V_{oc} conditions to understand the observed effect in details.

Figure 3.13 shows spatial results at open–circuit conditions. As it is seen in Figure 3.13(a), the charge carrier distribution is different than obtained from simulations without optical parameters for PEDOT:PSS. We can see that a part of hole concentration decreased due to the interface where 0.12 eV barrier between E_v of two layers exists, see Figure 3.1(a). The PEDOT:PSS acts as a hole transporting layer (HTL), therefore electrons are not transported through this layer. The change of charge carriers distribution has a direct impact effect on the electric field, as shown in Figure 3.13(b). Again, this effect is mostly visible at the interface where the most abrupt changes are observed. The electric field decreases extremely and it is the most visible for the smallest annihilation rate. In Figure 3.13(c) one could notice that the current distribution is shifted toward the interface. Also, no generation occurs in the HTL which leads to zero current for both electrons and holes. The excitons dristribution within an absorber follows the nonuniform profile, as shown in Figure 3.13(d). When integrating the concentration of excitons over space, it gives approximately the same concentration as for reference results for $\gamma_{n(p)S}$ equal to 10^{-14} m^3 s^{-1}. It is seen that for high annihilation rate there is a visible shift of exciton concentration toward the interface. As the generation profile is the same, this may be explained by bimolecular recombination which leads to creation of excitons with 25% probability. These simulations shows the importance of numerical simulations with interfaces which drastically changes current–voltage characteristics and influences the

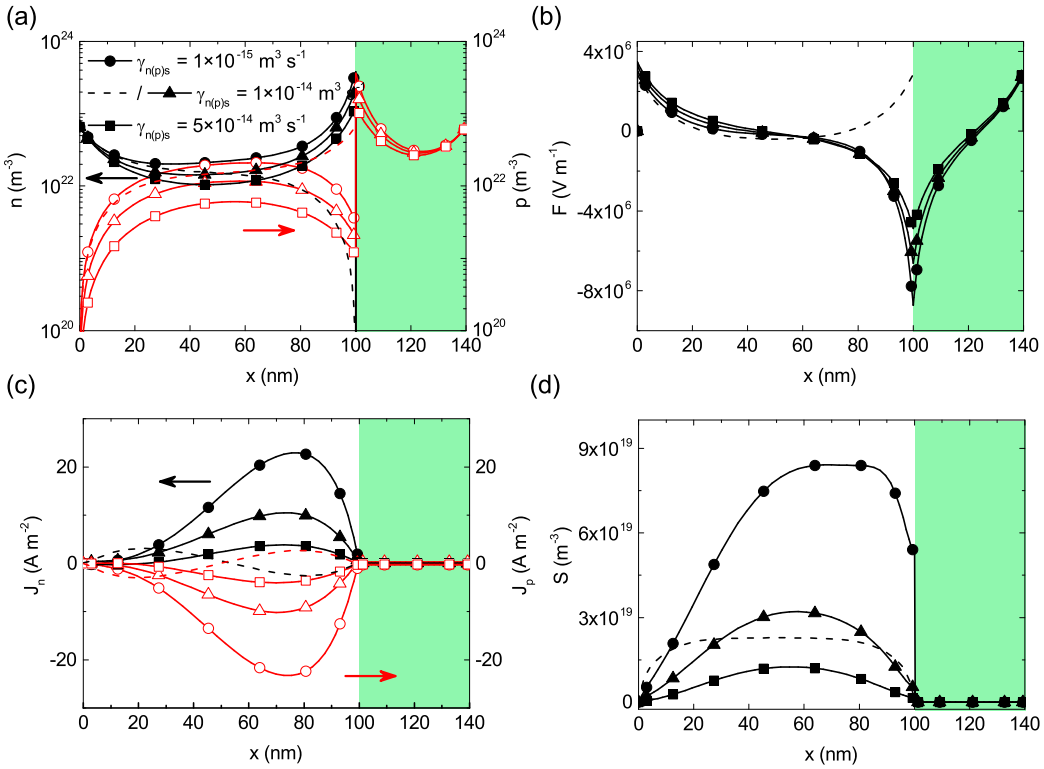

Figure 3.13: Numerical results calculated for open–circuit voltage V_{oc} with different annihilation rate constants. a) spatial distributions of electrons and holes, b) electric field distribution, c) current densities for electrons and holes versus distance from cathode, and d) a spatial distribution of excitons. Results of simulations are plotted as lines with symbols. Circles, triangles and squares denote the $\gamma_{n(p)s}$ equal to 10^{-15}, 10^{-14} and 5×10^{-14} m^3 s^{-1}, respectively. Closed and open symbols in parts (a) and (c) are used for electrons and holes, respectively. The dashed line represents results with uniform generation profile and without interfaces, where $\gamma_{n(p)s}$ is equal to 10^{-14} m^3 s^{-1}.

spatial distributions of electronic quantities.

Chapter 4

Studies of excitonic and ionic properties of organo–lead halide perovskite materials

Although perovskite materials have achieved extraordinary efficiency in application of solar cells, to further increase PCE, it is necessary to recognize all physical mechanisms which play a key role in the device operation. An open question is about a role of excitons and ions on the properties of perovskite solar cells (PSC). Therefore, the excitonic and ionic effects will be studied in the following chapter.

The perovskite materials are likely non–excitonic in the room temperature which an assumption is based on a very low effective mass and a high dielectric constant resulting in lower binding energy of Wannier exciton ($\approx$ 6 meV) in comparison to thermal energy ($\approx$ 26 meV) [22, 63, 112–114]. Therefore, a stability of this exciton would be extremely small. However, the electrical and transport properties of trihalide perovskites may drastically change with phase transition [24–26, 115]. In low temperature the binding energy of exciton increases to about 16–50 meV. Therefore, Wang et al. [116] have recently suggested that a perovskite semiconductor may be excitonic in orthorhombic phase due to a higher exciton binding energy than the thermal energy ($\approx$ 6 meV at 80 K) [22, 117]. This may have a direct implication in low temperature applications like in space environment for powering sattelites [118]. However, an exact role of excitons in the PSC requires better recognition.

In this chapter, the numerical studies are used to examine processes concerning excitons with a special focus on their formation mechanism. The results of simulations are validated with literature data of the most popular perovskite $CH_3NH_3PbI_3$ solar cell with different thicknesses. Here, we apply one dimensional transient model based on drift–diffusion equations for electronic charge carriers (electrons and holes), ions and excitons. Although the drift–diffusion model has been widely used to simulate organic photovoltaic cells [45, 46, 84, 105] and recently also for the organo–lead halide perovskite solar cells [33, 47–51, 119], it is

the first time where both ions and excitons are included for simulation of the perovskite material. We decided to analyze a perovskite solar cell in tetragonal (295 K) and orthorhombic (80 K) phases. The choice of temperature is based on accessibility of literature data for the PSC.

The investigation of halide–type perovskites suggests a high ionic conductivity caused by the migration of halide ions vacancies [120]. The recent studies of $CH_3NH_3PbI_3$ imply that this material is a mixed ionic and electronic conductor [49, 121, 122]. However, the nature of ionic migration still needs a better understanding especially that this phenomenon may influence the hysteresis effects. The aim of the second part of this chapter is to investigate the electronic and the ionic conductivities in $CH_3NH_3PbI_{3-x}Cl_x$ halide perovskite which is more stable (in air) than $CH_3NH_3PbI_3$. In order to separate both electronic and ionic conductivities, we have decided to use the modified DC Hebb–Wagner polarization method. In this experimental method, under the steady–state condition, only one type of charge carrier can flow through electrodes while the other is blocked by either ion or electron blocking material [123–127]. Recently, this technique was successfully applied to determine the partial conductivities in other materials [128, 129]. Thus, it seems to be a believable tool to investigate ionic effects in the perovskite. In addition, the ionic conductivity is measured as a function of temperature, which clearly shows an influence of different crystallographic phases on the electrical properties. Therefore, it can be treated as a complementary method to the numerical studies which involves both ions and excitons.

This chapter is partially based on [D. Głowienka, T. Miruszewski, J. Szmytkowski *The Domination of Ionic Conductivity in Tetragonal Phase of the Organometal Halide Perovskite* $CH_3NH_3PbI_{3-x}Cl_x$ Solid State Sci. **82** (2018) 19–23] and [D. Głowienka, J. Szmytkowski *Numerical Modeling of Exciton Impact in Two Crystalographic Phases of the Organo–lead Halide Perovskite (*$CH_3NH_3PbI_3$*) solar cell* Semicond. Sci. Technol. **34** (2019) 035018]

4.1 Investigation of excitonic effects

4.1.1 Theoretical model for the investigated device

For the purpose of the model, it is assumed that electron and hole transporting layers, which are usually used in perovskite solar cells, generate no losses of charge carriers. We can also neglect excitonic effects in ETL and HTL. This allows us to focus only in the absorber layer.

In the model, excitons are assumed to be immobile due to a very short lifetime. In addition, there is no information in literature about experimental observation of mobile excitons in the perovskite materials. Thus, to describe time (t) dependent excitonic processes, the continuity equation looks as follows [64, 130]

$$\frac{\partial S}{\partial t} = k_f np - k_{diss} S - \frac{S}{\tau_S}, \tag{4.1}$$

where k_f is bimolecular formation rate of excitons which can be formed from electrons and

holes. The excitons also dissociate with a rate k_{diss} described with the thermal dissociation model, see Section 2.1.6.2.
The system of equations for transport of electronic charges is based on continuity equations given for electrons

$$\frac{\partial n}{\partial t} = G + k_{diss}S - k_f np - R_m - R_b - R_t + \frac{1}{q}\frac{\partial}{\partial x}J_n, \tag{4.2}$$

and holes

$$\frac{\partial p}{\partial t} = G + k_{diss}S - k_f np - R_m - R_b - R_t - \frac{1}{q}\frac{\partial}{\partial x}J_p, \tag{4.3}$$

where J_n and J_p are given by Equations 2.8 and 2.9, respectively. The R_m, R_b and R_t are monomolecular, bimolecular and trimolecular recombination rates, respectively. More detailed description of the recombination mechanisms can be found in Section 2.1.7.

The simulated charge carriers densities are linked with the Poisson equation for potential distribution

$$\frac{\partial^2 \varphi}{\partial x^2} = -\frac{q}{\varepsilon_0 \varepsilon_r}\left(p - n + c - a\right). \tag{4.4}$$

It should be mentioned that the existence of electrons, holes and ions in one material causes nomenclature discrepancies in the names of electrodes. According to a standard definition, positively charged ions (cations) move toward the cathode and negatively ions (anions) flow in opposite direction. Thus, the positions of cathode and anode have been found as a result of temporal simulations where we investigated the accumulation of anions (mobile ions in the perovskite) near electrodes.

We should note that the existence of ionic charge carriers in the sample introduces a problem with a very long computing time. The reason is that ions are extremely slow in comparison to electronic charge carriers in perovskite solar cells [50]. The influence of ions on excitons is not studied here, therefore mobilities of ions can be set for higher values to increase the computation speed [33]. However, a special care must be taken for such dynamic simulations. In the transient calculations, the generation rate is first set to zero ($G = 0$) and the simulations last until steady state is achieved. At this moment charge carriers and ions are at thermodynamical equilibrium. In addition, ions should already finish to migrate through the sample just before illumination and futher simulations are not influencing their behaviour to a greater extent. Afterwards, the sunlight (AM1.5G) is turned on ($G \neq 0$) and each iteration is recorded [84]. In all simulations, the timestep is set to 1 ps due to relatively high dynamics of exciton processes. The spatial grid is nonuniformly distributed with Chebyshev polynomial, see Section 2.4.1. It makes possible to dense the grid closely to contacts where the most abrupt changes are observed. All parameters have been fixed in space which seems to be a good approximation that has been already used for simulation of perovskite solar cell [47, 49].

Table 4.1: Parameters used in the fitting of the experimental data and simulations at 295 K.

Parameter	Symbol	Value	
Relative permittivity	ε_r	63.05	Ref. [25]
Thickness of active material	L	250 nm	Ref. [131]
Exciton binding energy	E_b	6 meV	Ref. [112]
Exciton formation rate	k_f	10^{-12} m^3 s^{-1}	Ref. [64]
Exciton lifetime	τ_s	44 ps	Ref. [116]
Electron and hole capture coefficients	C_n, C_p	1.5×10^{-14} m^3 s^{-1}	Ref. [24]
Recombination reduction factor	ξ	10^{-4}	Ref. [47]
Electron and hole Auger constants	Γ_n, Γ_p	1.55×10^{-40} m^6 s^{-1}	Ref. [24]
Edge of conduction band	E_c	-3.9 eV	Ref. [132]
Edge of valence band	E_v	-5.4 eV	Ref. [132]
Schottky barrier heights for electrons and holes	φ_n, φ_p	0.1 eV	Ref. [48]
Initial density of ions	N_0	10^{23} m^{-3}	Ref. [50]
Trap density	N_t	10^{21} m^{-3}	Ref. [24]
Effective density of states in conduction and valence band	N_c, N_v	8.1×10^{24} m^{-3}	Ref. [48]
Mobility of anions	μ_a	10 cm^2 V^{-1} s^{-1}	Ref. [33]
Mobility of electrons	μ_n	4 cm^2 V^{-1} s^{-1}	Fit
Mobility of holes	μ_p	3 cm^2 V^{-1} s^{-1}	Fit
Built-in voltage	V_{built}	1.23 V	Fit
Maximum generation rate	G_{max}	1.55×10^{28} m^{-3} s^{-1}	Fit
Timestep	Δt	1 ps	Fixed
Number of grid points		100	Fixed

The model validation has been performed with a fit to experimental data for p-i-n structure with little or no hysteresis [131]. The data used in the fitting procedure are written in Table 4.1 with corresponding references to parameters for $CH_3NH_3PbI_3$. The mobilities are asymmetrical and within reported values [26, 133]. To fit a short–circuit photocurrent, the maximum charge generation rate is slightly changed and, for an open–voltage, the built–in voltage is fitted. The configuration of investigated device looks as follows: ITO/HTL/$CH_3NH_3PbI_3$/ETL/Al, where PEDOT:PSS is used for the hole transporting layer (HTL), and PCBM, C_{60} and BCP for the electron transporting layer (ETL). As mentioned earlier, the device stack has been modeled with only perovskite layer. Thus, we can assume that ETL and HTL are at the same electric potential levels as the interface of perovskite [50]. The model is sensitive for fitting, therefore a perovskite layer with three thicknesses 250, 280 and 630 nm were simulated with a single set of device parameters to find reasonable values. These values are used as a starting point for the following numerical simulations. Figure 4.1(a) shows a

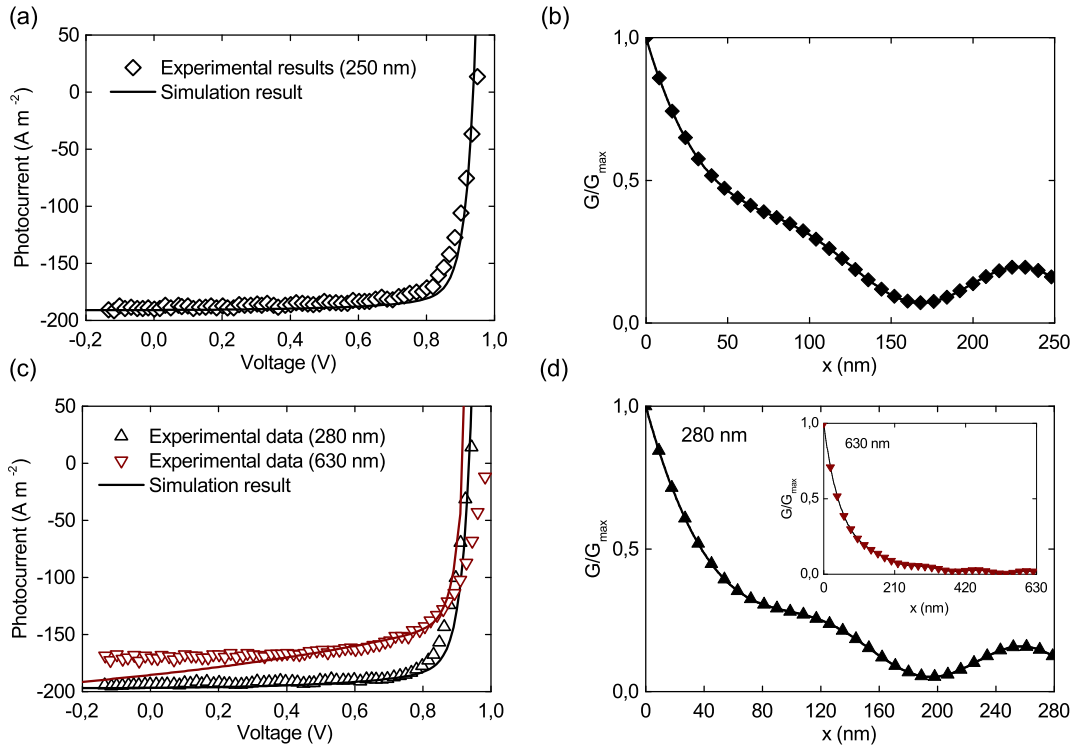

Figure 4.1: a) J–V characteristics for the absorber thickness 250 nm. The solid line represents the simulation and symbols show the experimental data for $CH_3NH_3PbI_3$ at 295 K, obtained from Ref. [131]. b) Generation (G) profile used in the simulation and calculated using the transfer matrix model. It is normalized with G_{max}.

comparison between theoretical and experimental results for a thickness 250 nm. A good agreement has been obtained. Further in the chapter, we focus only on 250 nm perovskite thickness layer. Figure 4.1(b) demonstrates the generation profile calculated with the transfer matrix model, see Section 2.1.5. The optical parameters of each layer used in the solar cell are given in Figure 2.1. The fitting could be also performed with a constant value of G (uniform generation profile), however the loss of absorbed light within the thick sample of perovskite solar cell is high. Therefore, a nonuniform generation should be used. The fitting results for 280 and 630 nm are presented in Figure 4.1(c) with corresponding generation profiles, see Figure 4.1(d). We can see that the fit is in excellent agreement with experimental results obtained for a thickness 280 nm. However, the J–V slope is slightly shifted for the case of 630 nm. This may be due to neglecting of interface effects. However, we focus only on the excitonic phenomena in the bulk, therefore the contact effects may be ignored. The ions are located only within a perovskite layer in the p-i-n structure. Obviously, anions and cations can change an electric field distribution in the bulk of sample. Therefore, it should be noted that the experimental data could be also well fitted with immobile ions using parameters adopted from literature (not shown here).

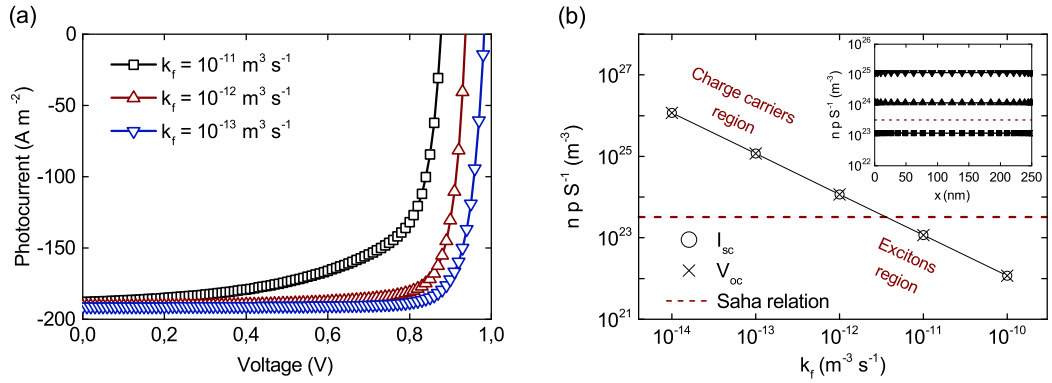

Figure 4.2: Simulation results for different exciton formation parameters at 295 K. a) J–V characteristics, b) a Saha relation for J_{sc} (circle symbol) and V_{oc} (cross symbol) with red line showing equilibrium level between charge carriers and excitons. An inset shows spatial distribution of Saha relation. Squares, upper triangles and lower triangles denote the exciton formation rates (k_f) equal to 10^{-11}, 10^{-12} and 10^{-13} m^3 s^{-1}, respectively.

The next two sections for 295 K and 80 K are organized in the following manner. First, we analyze spatial impact of excitons on perovskite solar cell at steady–state condition with continuous AM1.5 light illumination. Further, the dynamic simulations are shown. Also, if not specified otherwise, the parameters from Table 4.1 are used in all simulations.

4.1.2 Numerical results for tetragonal phase

To analyze the exciton impact in perovskite solar cells, we decided to choose three values of the exciton formation rate: 10^{-11}, 10^{-12} and 10^{-13} m^3 s^{-1}, called in the chapter high, intermediate and low formation rates, respectively. The values are chosen based on $k_f = 10^{-12}$ m^3 s^{-1} that is close to the experimental result estimated by Stranks et al. [64]. Figure 4.2(a) shows the J–V characteristics calculated for these three values of k_f. It is observed that the magnitude of J_{sc} is changed negligibly with k_f but a value of V_{oc} calculated for the high and low rates changes by about 0.05 V in respect to the intermediate formation rate. This may have practical implication for further analysis of losses for an open–circuit (OC) condition. Therefore, most of the simulations are shown only for OC state.

As the impact of excitons is not clearly visible in the spatial distribution in the bulk of perovskite material, the appropriate tool is needed. Therefore, the Saha equation [63, 114, 134, 135] is applied to distinguish whether excitons or free charge carriers dominate in the PSC. It has the form

$$\frac{np}{S} = n_{eq}(T) = \left(\frac{2\pi m_S k_B T}{h^2}\right)^{3/2} \exp\left(-\frac{E_B}{k_B T}\right), \tag{4.5}$$

where n_{eq} represents the equilibrium state which means that the densities of electrons, holes and excitons are equal ($n = p = S$). The reduced effective mass can be defined as $m_S =$

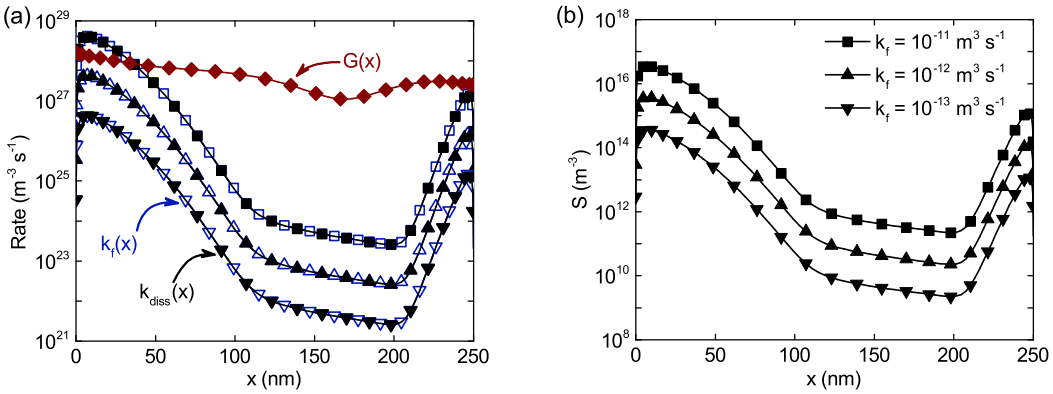

Figure 4.3: Simulation results for short–circuit current (J_{sc}) at 295 K. a) Exciton formation, dissociation and charge carrier generation rates, b) exciton density distribution. The diamond symbols indicate a rate of charge carriers generation. Squares, upper triangles and lower triangles denote the exciton formation rates (k_f) equal to 10^{-11}, 10^{-12} and 10^{-13} m^3 s^{-1}, respectively. The closed symbol is used for formation rate and open symbol represents dissociation rate of excitons.

$m_e m_h / (m_e + m_h)$, where m_e and m_h are effective masses of electron and hole, respectively. An interpretation of the Saha equation is that excitons prevail below n_{eq} and the free charge carriers are dominant above this value. Figure 4.2(b) presents a graphical illustration of the Saha equation where the ratio np/S is calculated for different exciton formation rates. The dashed line shows the equilibrium state n_{eq} calculated for the exciton binding energy equal to 6 meV for 295 K taken from literature [112], and the reduced effective mass 0.104 m_e reported for the $CH_3NH_3PbI_3$ perovskite [22]. For all cases, we obtained constant values of np/S presented by horizontal lines, as shown in Figure 4.2(b-inset). It is clearly seen that charge carriers prevail for the low and intermediate exciton formation rate and excitons are in dominance only for the high value of k_f. We should also mention that the Saha relation looks the same for J_{sc} and V_{oc} because it does not depend on the bias voltage, as shown in Figure 4.2(b).

Generally, under the short–circuit (SC) condition, all losses are lower than a generation of electrons and holes for integration over the entire device. This condition is self consistent for the model. Whereas for OC, both recombination and generation should be equal [47]. Therefore, the case when the sum of all recombination rates is greater than the generation rate has no physical sense. Figure 4.3(a) presents a comparison of a charge generation rate (G) with the rates $k_f \times np$ and $k_{diss}(T) \times S$, which are associated with the exciton formation and the exciton dissociation, respectively, all calculated for J_{sc}. It is seen that for a high value of k_f, the formation rate ($k_f \times np$) averaged in space (6.64×10^{27} m^{-3} s^{-1}) is slightly higher than the generation rate (5.85×10^{27} m^{-3} s^{-1}). Based on this observation, it can be concluded that although the Saha equation shows a domination of excitons [Figure 4.2(b)], the case with $k_f = 10^{-11}$ m^3 s^{-1} is not physical. This also shows the maximum limit for the formation rate of excitons at room temperature. We also observe that the formation and dissociation rates

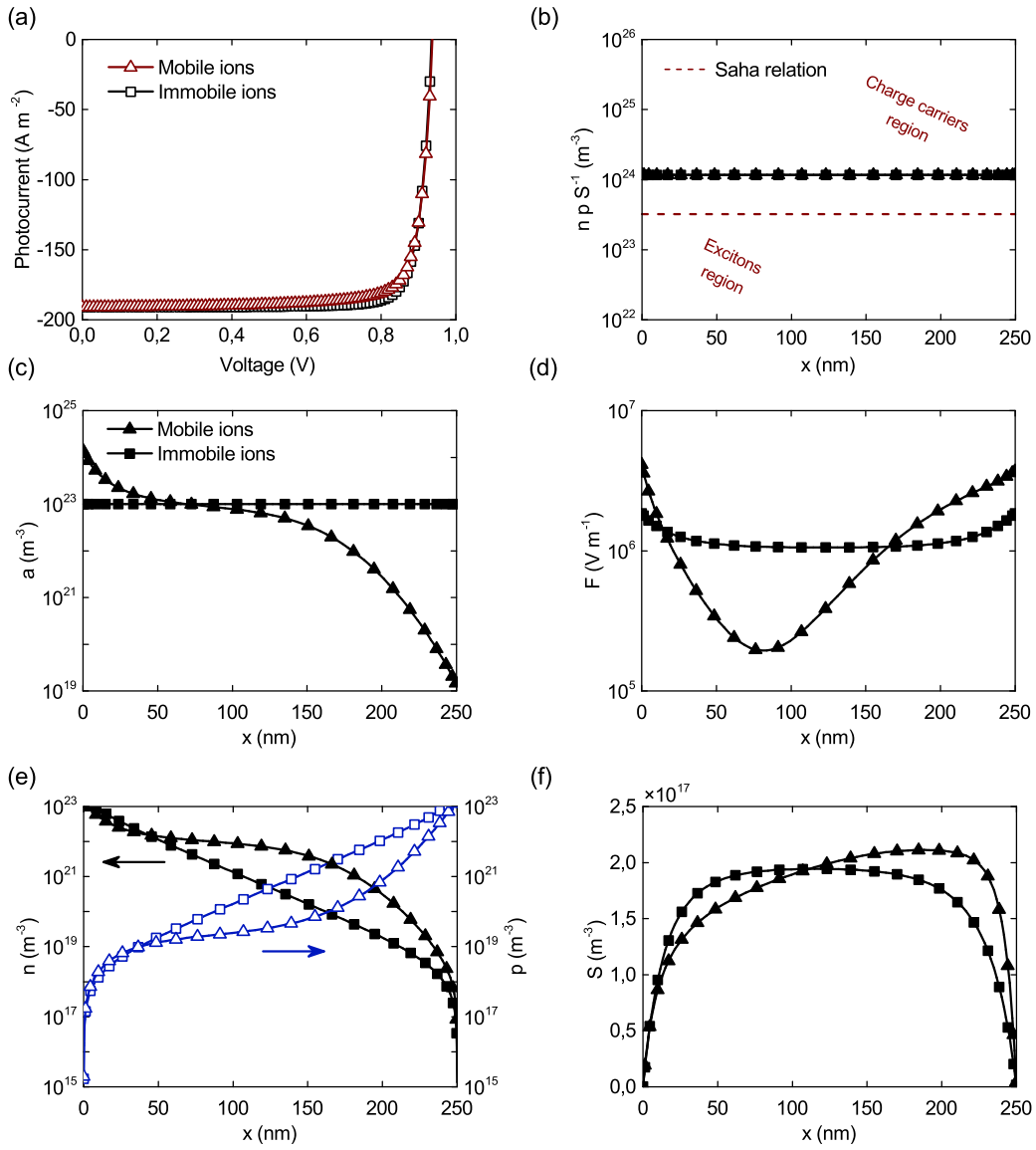

Figure 4.4: Simulation results at 295 K. a) J–V characteristics, b) a Saha relation with red line showing equilibrium level between charge carriers and excitons. Spatial distributions for c) anions density, d) electric field, e) electrons (closed symbol) and holes (open symbol) concentrations, and f) excitons concentration. Squares denote results for immobile ions and upper triangles represent results with mobile ions. The exciton formation rate (k_f) is equal to 10^{-12} m^3 s^{-1}.

follow the same dynamics for the equilibrium state which was recently suggested by Stranks et al. [64]. Therefore, excitons are created and lost within the same period of time due to their low binding energy. As shown in Figure 4.3, the shape of the formation rate follows the shape of the excitons distribution in space. This behavior can be explained this way that excitons are generated only as a result of the formation process, see Equation 4.1.

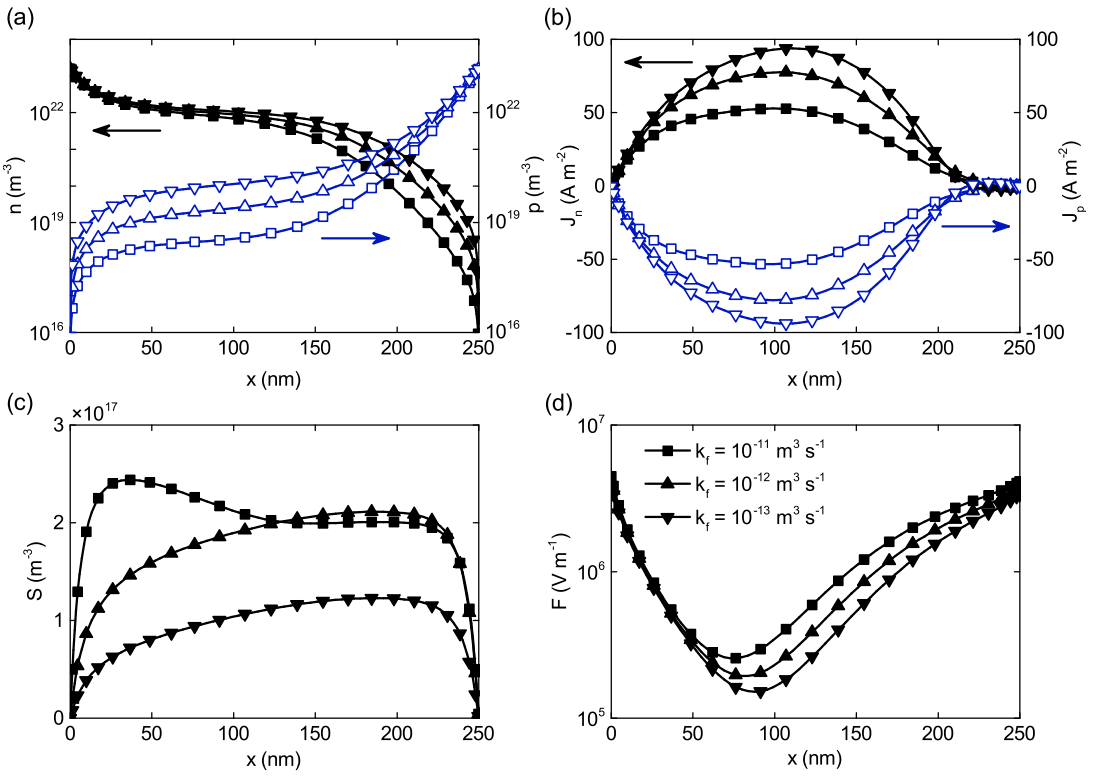

Figure 4.5: Simulation results for open–circuit (V_{oc}) at 295 K. Spatial distributions for a) electrons (closed symbol) and holes (open symbol) concentrations, b) electron (closed symbol) and hole (open symbol) photocurrents, c) exciton concentration, and d) electric field. Squares, upper triangles and lower triangles denote the exciton formation rates (k_f) equal to 10^{-11}, 10^{-12} and 10^{-13} m^3 s^{-1}, respectively.

We can see that nonuniform generation rate leads to irregular shape of the excitons distribution in space for SC condition. In addition, an electric potential and, as a consequence, an electric field depend on the distributions of all types of electric charges (electrons, holes and both types of ions) which, in general, are mobile with different mobilities. Thus, we can expect further irregularities in simulated curves which can create problems with an exact analysis. Therefore, we have decided to simulate also curves with immobile ions. The impact of a nonuniform generation profile on analysis of spatial distributions have been already discussed in Chapter 3 for the case of organic solar cells. These studies have shown that the nonuniform generation has only an impact on the distributions of photocurrents J_n and J_p which follow the shape of the generation profile. The same tendency is observed for perovskite materials, therefore the analysis is not shown here for clarity. The immobile ions slightly change the J–V characteristics and do not impact the Saha relation, see Figure 4.4(a,b). We can notice that a concentration of mobile anions (a) decreases drastically in the bulk of sample, as shown in Figure 4.4(c). Therefore, the electric field distribution changes visibly in comparison to the case of immobile ions, as illustrated in Figure 4.4(d). For an open–circuit, the minimum

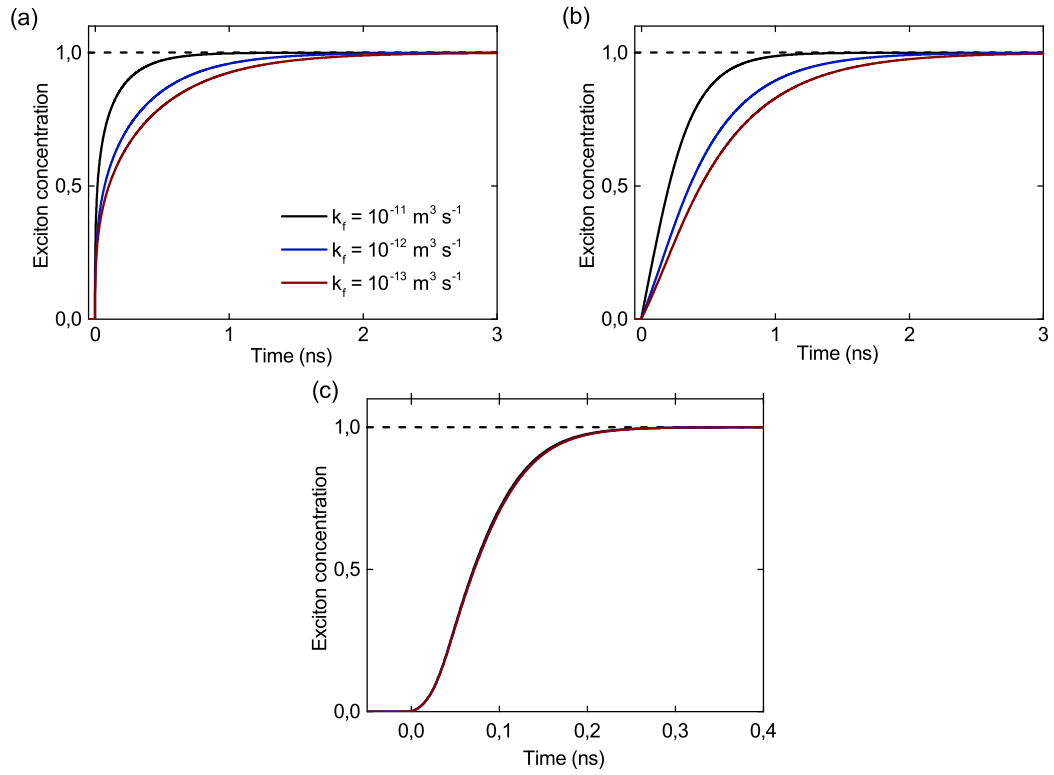

Figure 4.6: Simulation results at 295 K. Transient results for exciton concentration for open–circuit (V_{oc}) a) at the position close to the anode, and b) in the middle of sample. Transient results for exciton concentration for short–circuit (J_{sc}) in the middle of sample (c). Black, blue and red lines denote the exciton formation rates (k_f) equal to 10^{-11}, 10^{-12} and 10^{-13} m^3 s^{-1}, respectively. All results are normalized.

of $F(x)$ is shifted toward the anode. In Figure 4.4(e), it could be also noted that the mobile ions influence charge carrier concentrations by shifting charge carrier density toward the cathode of PSC. We can see that the exciton concentration in space is symmetrical when ions are immobile and becomes asymmetrical for a case of mobile anions. The position of the maximum in the distribution of excitons coincides with the observed changes of electrons and holes concentrations close to the cathode, see Figures 4.4(f).

Figure 4.5 presents simulation results calculated for three values of the exciton formation rate in the case of OC condition. As it is observed in Figure 4.5(a), an increase of the formation parameter lowers the density of electrons and holes which directly impacts the V_{oc} level in the same way. This behavior could be explained by the mechanism of exciton formation, where an electron and a hole interact with each other and create an exciton with a probability related to the formation rate, as shown in Equation 4.1. In Figure 4.3(a), it has been proved that excitons dissociate with the same rate for SC. Therefore only negligible changes in electrons and holes distributions, and their photocurrents would be observed. However, under OC condition, where an electric field is much lower inside the PSC, the exciton formation

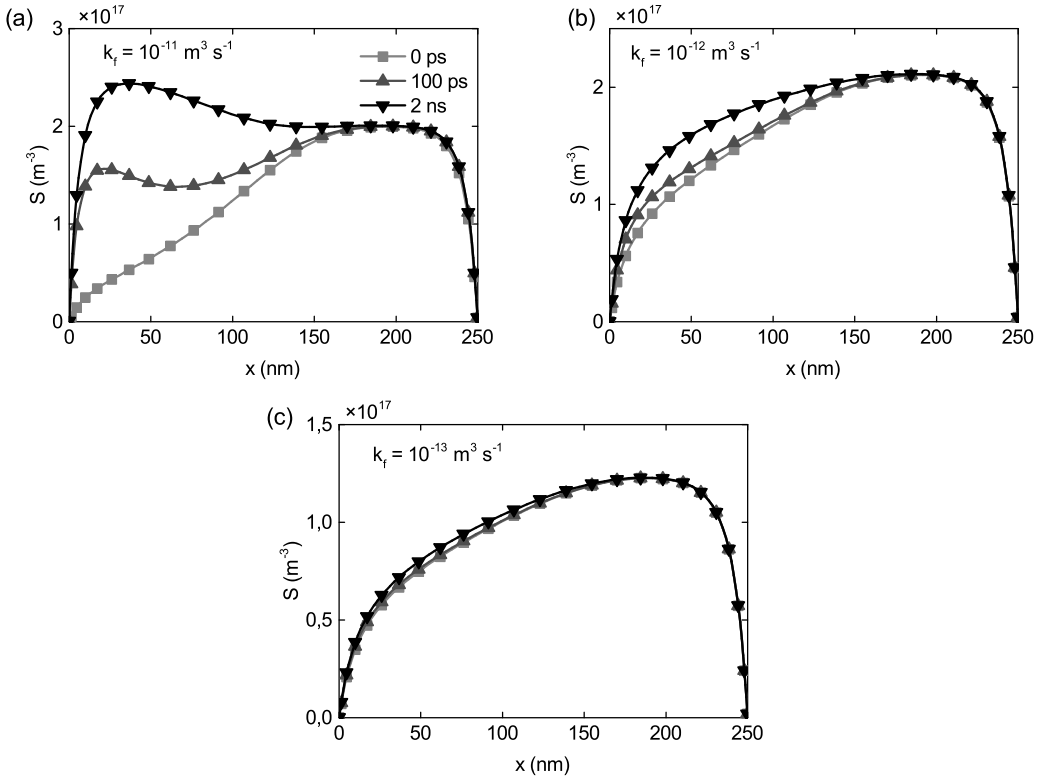

Figure 4.7: Simulation results for open–circuit (V_{oc}) at 295 K. Spatial distribution for formation rates (k_f) equal to a) 10^{-11}, b) 10^{-12}, and c) 10^{-13} m^3 s^{-1}. Squares, upper triangles and lower triangles denote spatial distributions for 0 ps, 100 ps and 2 ns, respectively, which is a time since generation was turned on ($G \neq 0$).

and the dissociation rates are not equal (results not shown here). Thus, excitons can also recombine monomolecularly within their lifetime τ_S. Consequently, not all free electrons and holes are produced back from excitons which results in lowering their densities. Due to changes of these concentrations, the space distributions of photocurrents are also influenced. For the higher exciton formation rate, the electron (J_n) and the hole (J_p) photocurrents decrease about the zero axis, see Figure 4.5(b). These distributions are likely lowered due to observed changes of electric field with increasing rate of exciton formation, illustrated in Figure 4.5(d). It can be also noticed that the value of photocurrent at a maximum point (for OC condition) is much higher than for organic solar cell [58, 105]. This is directly caused by a nonuniform generation and a thicker absorber layer. As shown in Figure 4.5(c), the exciton density increases uniformly across the material, if changed from low to intermediate values of formation rate. However, the shape of this distribution changes drastically for a high k_f. The explanation for this behavior will be provided in further part of the chapter with a discussion of dynamical simulation results.

The next step is to analyze transient results to get more insight into process of exciton formation. Figure 4.6 shows results of the normalized exciton concentrations close to an

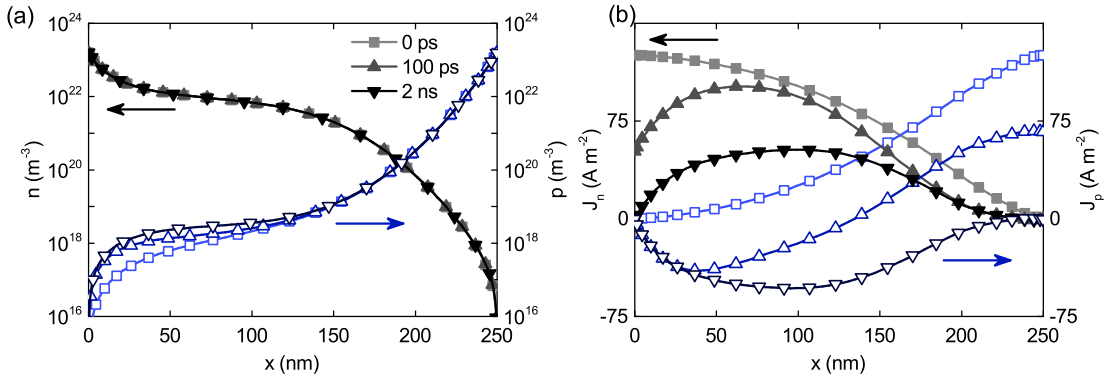

Figure 4.8: Simulation results for open–circuit (V_{oc}) at 295 K. Spatial distributions of a) electrons (closed symbol) and holes (open symbol) concentrations, and b) electron (closed symbol) and hole (open symbol) currents. Squares, upper triangles and lower triangles denote spatial distributions for 0 ps, 100 ps and 2 ns, respectively, which is a time since generation was turned on ($G \neq 0$). The exciton formation rate (k_f) is equal to 10^{-11} m^3 s^{-1}.

electrode position (part a) and in the middle of the sample (part b), both presented for an open–circuit. It is observed that excitons closer to the electrode are slightly more dynamic. The steady–state is reached faster when the exciton formation rate increases. For SC condition, the time of steady–state is shorter than for OC and independent on the value of k_f, as shown results in the middle of the sample in Figure 4.6(c). It originates from a higher level of electric field for J_{sc} and therefore the exciton formation rate does not influence neither dynamics of photocurrent nor excitons concentration. Therefore, further analysis of transient simulations are focused on OC condition only.

Figure 4.7 shows a spatial distribution of excitons (for the case of OC) calculated for three times equal to 0 ps, 100 ps and 2 ns which represent a time counting after generation is turned on ($G \neq 0$). These times have been chosen in a way that there is no illumination (0 ps), the light–soaking has already taken place (100 ps) and the steady–state condition has been reached (2 ns). It is seen that at 0 ps the shapes of excitons distribution for high (part a), intermediate (part b) and low (part c) values of k_f are similar due to negligible influence of illumination. However, when the generation is turned on, we observe an increase of excitons for high and intermediate formation rates but only close to the anode. Therefore, in Figure 4.8(a) we present results only for $k_f = 10^{-11}$ m^3 s^{-1} in OC condition as there is the most visible impact. Here, we can notice that light generates more holes near the anode. Therefore, excitons created with a high formation rate occur because light increases the concentration of holes which approach electrons that are major charge carriers in this region. The spatial distribution of photocurrent is also established for an open–circuit when an illumination is turned on, see Figure 4.8(b).

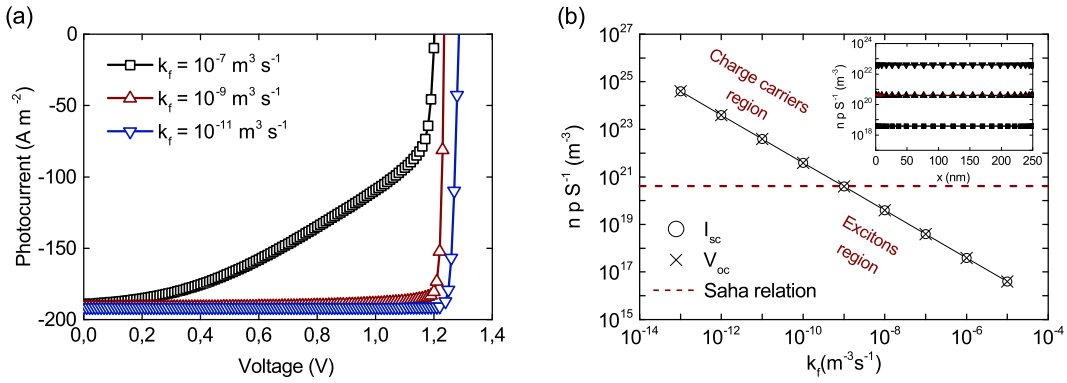

Figure 4.9: Simulation results for different exciton formation parameters at 80 K. a) J–V characteristics, b) a Saha relation for J_{sc} (circle symbol) and V_{oc} (cross symbol) with red line showing equilibrium level between charge carriers and excitons. An inset shows spatial distribution of Saha relation. Squares, upper triangles and lower triangles denote the exciton formation rates (k_f) equal to 10^{-7}, 10^{-9} and 10^{-11} m^3 s^{-1}, respectively.

4.1.3 Numerical results for orthorhombic phase

The next step is to analyze the impact of excitons at low temperature. As it was mentioned before, the perovskite material changes phase with temperature which influences its properties. The most importantly, the exciton binding energy is increasing for orthorhombic phase to about 34 meV which is now higher than the thermal energy (6 meV at 80 K) [136]. This may suggest higher stability of the produced exciton in lower temperature. However, Wang et al. [116] have reported that the exciton lifetime is much shorter and decreases to about 3 ps. Also, it is still not clear what is a type of excitons in organo-lead halide perovskite materials at low temperature. Although, one can find a hypothesis that such excitons are of Wannier type [117, 137] but this assumption requires further studies to prove it. The difficulties ar-

Table 4.2: Parameters for simulation at 80 K.

Parameter	Symbol	Value	
Exciton binding energy	E_B	34 meV	Ref. [136]
Dielectric constant	ε_r	39.39	Ref. [25]
Mobility of electrons	μ_n	143 cm^2 V^{-1} s^{-1}	Ref. [24]
Mobility of holes	μ_p	143 cm^2 V^{-1} s^{-1}	Ref. [24]
Exciton decay time	τ_s	3 ps	Ref. [116]
e$^-$ and h$^+$ capture coefficients	C_n, C_p	3.18×10^{-15} m^3 s^{-1}	Ref. [24]
e$^-$ and h$^+$ Auger constants	Γ_n, Γ_p	23.4×10^{-40} m^6 s^{-1}	Ref. [24]
Edge of conduction band	E_c	-3.9 eV	Ref. [29]
Edge of valence band	E_v	-5.5 eV	Ref. [29]
Reduction factor	ξ	1.66×10^{-4}	Ref. [24]

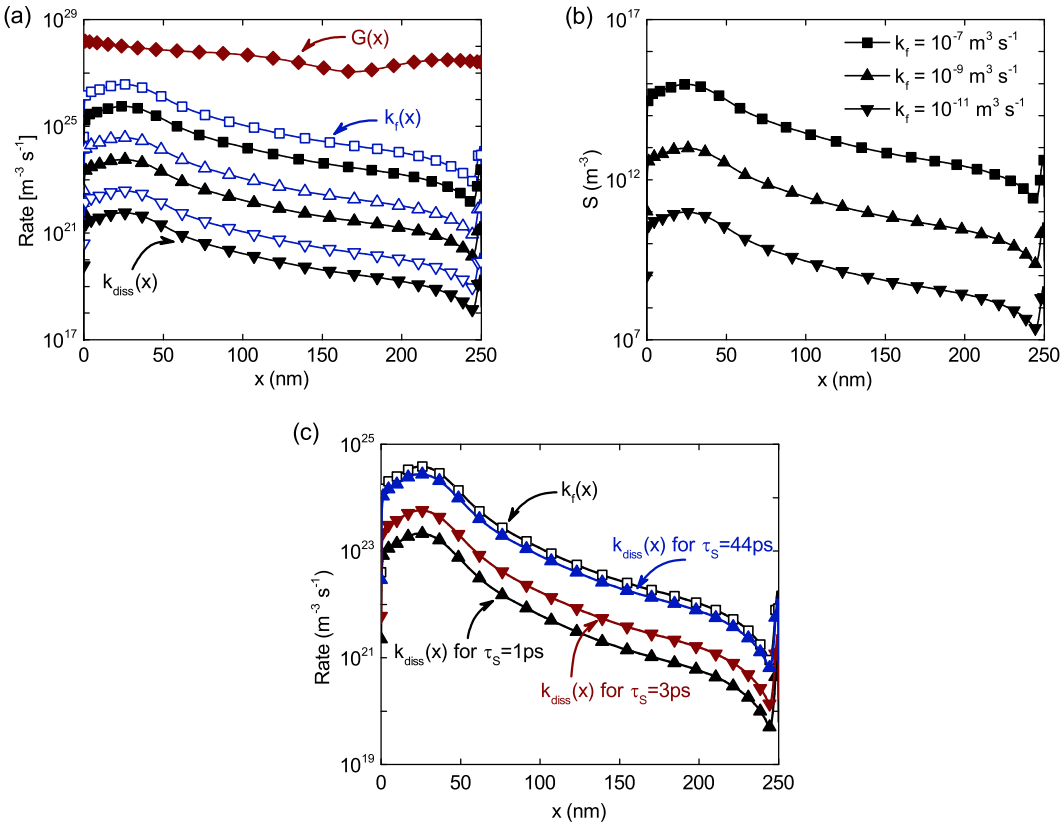

Figure 4.10: Simulation results for short–circuit current (J_{sc}) at 80 K. a) Exciton formation, dissociation and charge carrier generation rates, b) exciton density distribution. The diamond symbols indicate the rate of charge carriers generation. Squares, upper triangles and lower triangles denote the exciton formation rates (k_f) equal to $10^{-7}, 10^{-9}$ and 10^{-11} m^3 s^{-1}, respectively. c) Upper triangle, lower triangle and diamonds represent spatial distributions of $k_d \times S(x)$ rate for 1, 3 and 44 ps exciton decay times, respectively, all for k_f equal to 10^{-9} m^3 s^{-1}. Squares denote a spatial distribution of $k_f \times n(x)p(x)$ rate which does not change for different τ_s. The closed symbol is used for the formation rate and open symbol represents the dissociation rate of excitons.

rise when finding experimental values of k_f at low temperatures as it has not been measured in perovskite materials yet. In general the bimolecular formation rate depends strongly on temperature and it increases by orders of magnitude when lowering the lattice temperature of semiconductor [130, 138–140]. Therefore, we have decided to choose wider range of exciton formation rate which represent overall tendency observed in semiconductors. For low temperature simulation k_f is equal to 10^{-7}, 10^{-9} and 10^{-11} m^3 s^{-1}, called in this paragraph high, intermediate and low exciton formation rates, respectively. In the absence of experimental data (κ and η parameters) for $CH_3NH_3PbI_3$ material at low temperature, the generation profile has been used the same as at room temperature, see Figure 4.1(b). Other parameters, which are presented in Table 4.2, have been adopted from literature for the perovskite material (80 K).

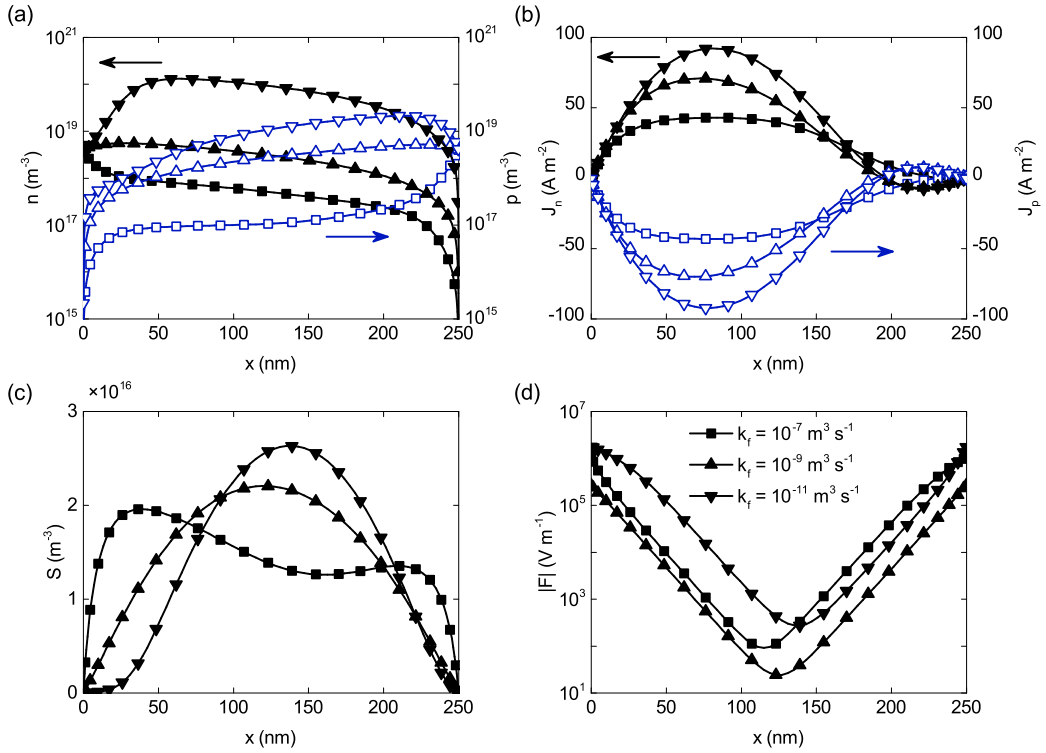

Figure 4.11: Simulation results for open–circuit (V_{oc}) at 80 K. Spatial distribution for a) electrons (closed symbol) and holes (open symbol) concentrations, b) electron (closed symbol) and hole (open symbol) photocurrents, c) exciton concentration, and d) electric field. Squares, upper triangles and lower triangles denote the exciton formation rates (k_f) equal to $10^{-7}, 10^{-9}$ and 10^{-11} m^3 s^{-1}, respectively.

Figure 4.9(a) shows J–V characteristics calculated using the values of k_f from above. First, it should be noticed that V_{oc} is shifted about 0.35 V, if a temperature changes from 295 K to 80 K for the same exciton formation rate equal to 10^{-11} m^3 s^{-1}. The same tendency has been observed by Shao et al. [141] for the PSC, where a decreasing temperature (from 295 K to 140 K) has increased V_{oc} by about 0.15 V. Second, the impact of exciton formation rate is the same as for tetragonal phase, where the rise of k_f causes that a value of V_{oc} increases but J_{sc} is the same. The Saha relation once again shows a flat distribution in space, see Figure 4.9(b). For a low value of the exciton formation rate, electrons and holes dominate in the PSC. However, for the intermediate k_f, we observe an equilibrium between free charge carriers and excitons which means that there is no dominant part. Therefore, even a small increase of the formation rate would lead to dominance of excitons in the $CH_3NH_3PbI_3$ absorber layer, as observed for high k_f.

Figure 4.10(a) shows a comparison of the generation, dissociation and exciton formation rates calculated for SC condition. It is clearly seen that the probability of a generation process is around two orders of magnitude higher than for formation and dissociation mech-

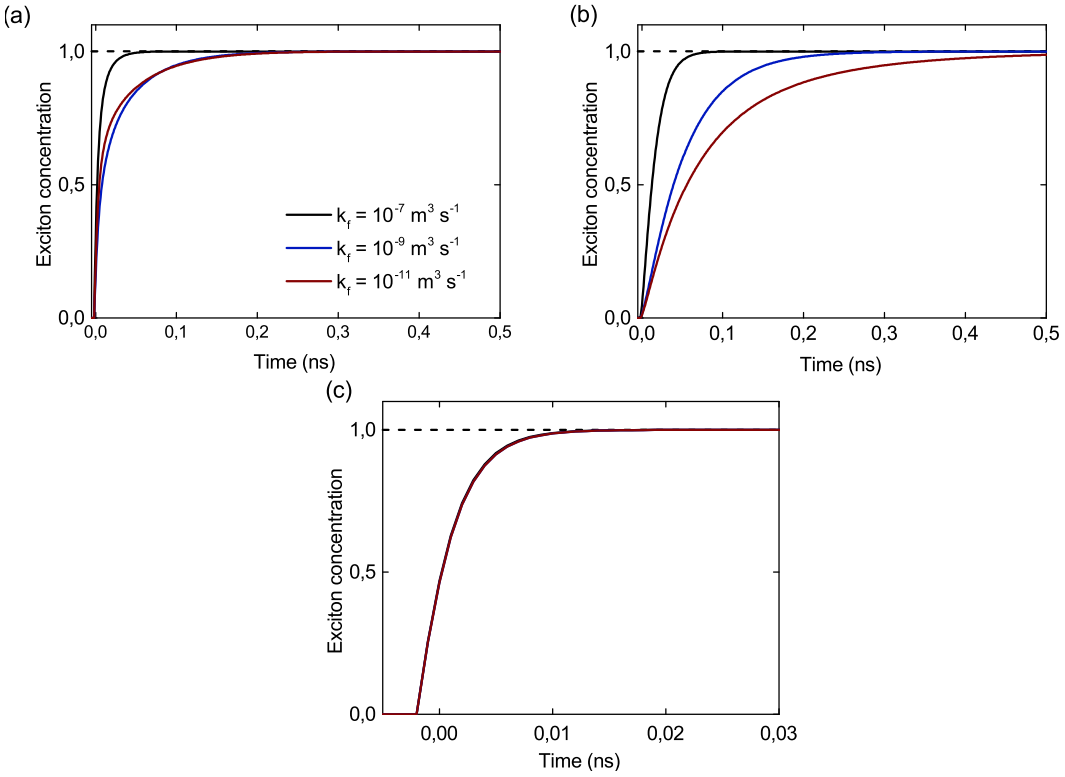

Figure 4.12: Simulation results at 80 K. Transient results for exciton concentration a) at the position close to the anode, and b) in the middle of sample. Transient results for exciton concentration for short–circuit (J_{sc}) in the middle of sample (c). Black, blue and red lines denote the exciton formation rates (k_f) equal to 10^{-7}, 10^{-9} and 10^{-11} m^3 s^{-1}, respectively. All results are normalized.

anisms. Therefore, we can conclude that excitons prevail in the perovskite solar cell at the orthorhombic phase (at low temperature). It is also possible that the formation rate could be even higher for lower temperatures, however to formulate final conclusion there is a need for experimental confirmation which is not an aim of these studies. In Figure 4.10(a), we can also observe that the rates of the exciton formation and the dissociation, presented as a function of a distance from the electrode, both follow the distribution of excitons, see Figure 4.10(b). However, the rates are not equal and the formation process is more possible than a dissociation due to a much higher monomolecular recombination of excitons which is inversely proportional to exciton lifetime. For a high value of τ_S almost all free electrons and holes are produced back from excitons, see Figure 4.10(c). Although, for smaller τ_S, the recombination competes with other processes and, as a consequence, not all excitons dissociate. This conclusion supports the statement that excitons are dominant in the PSC at low temperature and the excitonic mechanisms influence the operation of the low temperature devices.

Figure 4.11 illustrates spatial results presented for different exciton formation rates calcu-

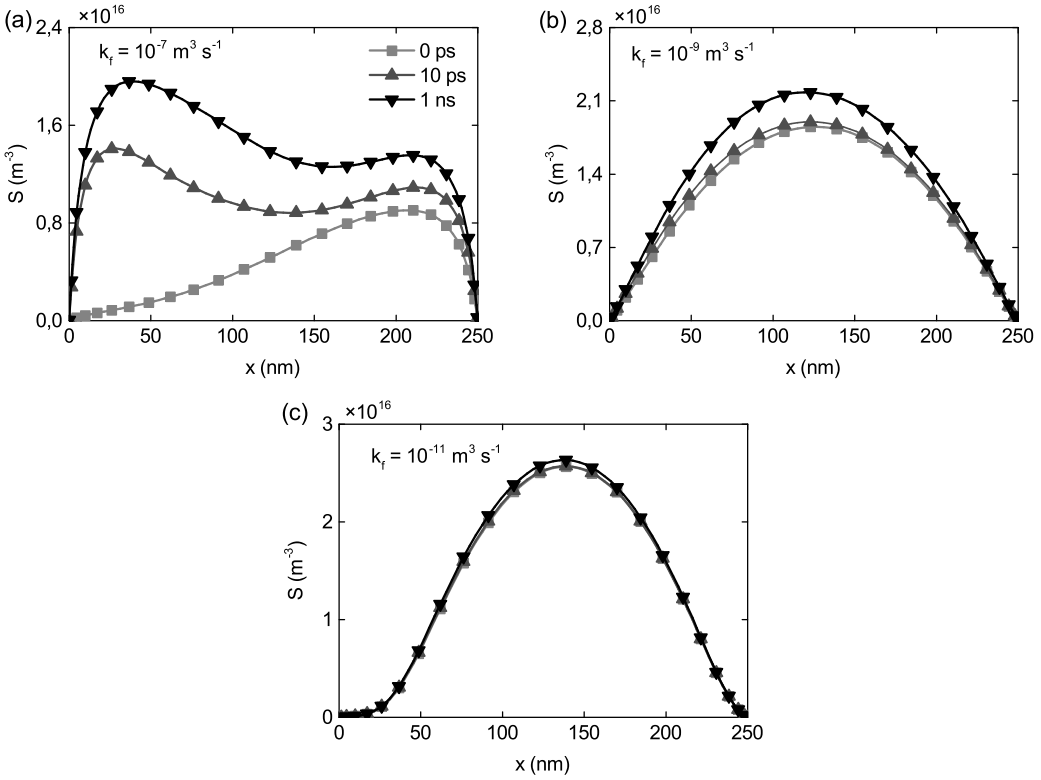

Figure 4.13: Simulation results for open–circuit (V_{oc}) at 80 K. Spatial distributions for exciton formation rate (k_f) equal to a) 10^{-7}, b) 10^{-9}, and c) 10^{-11} m^3 s^{-1}. Squares, upper triangles and lower triangles denote spatial distributions for 0 ps, 10 ps and 1 ns, respectively, which is a time since generation was turned on ($G \neq 0$).

lated for OC. We can see that the electron and hole concentrations are the highest in the middle of the sample for a low formation rate. The boundary conditions clearly show that the density of carriers near electrodes should decrease for lower temperatures. For higher values of k_f, the total concentrations of n and p are lower in the bulk of the sample relatively to the position which is closer to the metal electrode. As shown in Figure 4.11(b), the formation rate also affects the spatial distribution of photocurrents J_n and J_p. It can be noticed that the both photocurrents decrease for higher k_f. This is directly influenced by a change of charge carrier concentration and also by an electric field distribution ($|F|$). An absolute value originates from the negative electric field values due to relation $V_{oc} > V_{built}$, as shown in Figure 4.11(d). As illustrated in Figure 4.11(c), the shape of excitons distribution spreads more uniformly across the sample and a total density of excitons slightly increases only for higher formation rate. The observed shape of S is most likely due to the drastic decrease of charge carrier concentration in the middle of PSC.

Figure 4.12 illustrates transient results of the exciton concentration obtained for two spatial points, meaning close to the anode and in the middle of the $CH_3NH_3PbI_3$ absorber layer (both for V_{oc}). It can be noticed that the observed dynamics at low temperature is about or-

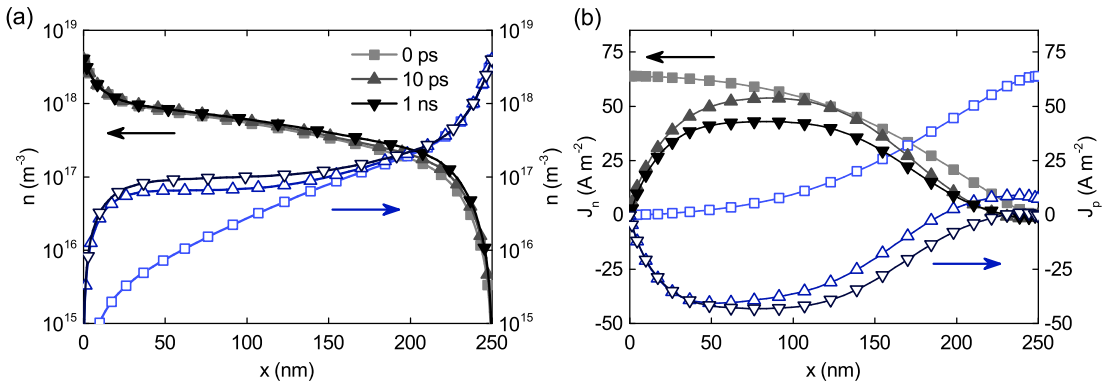

Figure 4.14: Simulation results for open–circuit (V_{oc}) at 80 K. Spatial distributions of a) electrons (closed symbol) and holes (open symbol) concentrations, and b) electron (closed symbol) and hole (open symbol) currents. Squares, upper triangles and lower triangles denote spatial distributions for 0 ps, 10 ps and 1 ns, respectively, which is a time since generation was turned on ($G \neq 0$). The exciton formation rate (k_f) is equal to 10^{-7} m^3 s^{-1}.

der of magnitude faster than for room temperature. This effect originates because the processes of exciton formation and monomolecular recombination need shorter times for the orthorhombic phase, see Table 4.2. We also observe that the steady–state condition is reached much faster for the position closer to the electrode than in the middle of the sample. In Figure 4.12(a), it is visibly seen that the higher formation rate drastically increases dynamics. However, for intermediate and low values, we obtained approximately the same results. In the bulk of the $CH_3NH_3PbI_3$ layer, the dynamics is getting higher with the exciton formation rate, illustrated in Figure 4.12(b). Therefore, in contrast to simulations at room temperature, a rise of the concentration S depends not only on the rate k_f but also on the position in the device. At the SC state, the observed dynamics is really high and independent of the exciton formation rate and the position, as shown in Figure 4.12(c). For this reason transient analysis in SC condition is skipped for this chapter.

Figure 4.13 shows spatial distributions of excitons calculated for three times equal to 0 ps, 10 ps and 1 ns after illumination (OC condition). It is observed that without illumination (0 ps), the maximum density of excitons is shifted toward the cathode for higher exciton formation rate, and to the middle of the sample for the lower rate. When the generation (G) is turned on, there is a visible increase in exciton density observed only for high and intermediate values of k_f. Figure 4.13(a) illustrates that a concentration S drastically increases close to the anode for the high k_f. For the low and intermediate exciton formation rates, an impact of illumination is smaller. Similarly to results reported for a room temperature, this effect is due to a higher hole density which influences the creation of electron–hole pairs after illumination, as shown in Figure 4.14(a). When the generation is turned on, the average value of exciton density increases in the bulk of the $CH_3NH_3PbI_3$ absorber layer, imitating the shape of a hole density. It suggests that holes, which are less mobile in the PSC, take a crucial part in the process of the excitons creation. In Figure 4.14(b), we can see the photocurrent dis-

tributions of J_n and J_p obtained for V_{oc}. For the case when the generation is turned on, both currents are distributed symmetrically about the zero value.

4.2 Ionic conductivity studies of perovskite material

Here, the experiment for $CH_3NH_3PbI_{3-x}Cl_x$ is presented. This part is organized as follows. First, a synthesis of the material and studies of its structural properties are described. Next, the measurement of electrical conductivity as a function of temperature and the analysis of obtained results are reported.

4.2.1 The material preparation and an experimental procedure

The perovskite $CH_3NH_3PbI_{3-x}Cl_x$ precursor was prepared with the following procedure. The commercial Methyloamine (33 wt % in ethanol) from Sigma Aldrich, hydroiodic acid (57 wt % in water) from Alfa Aesar, lead (II) chloride ($PbCl_2$) (99 %) from Acros Organics, ethanol, dimethylformamide (DMF) and diethyl ether have been used. To obtain methylammonium iodide (MAI) powder, methyloamine and hydroiodic acid were mixed in round–bottom flask in 1:1 molar ratio with 100 mL of ethanol. The stirring has been continued for 2 hours in the ice bath due to the exothermic nature of reaction, and evaporated at 50°C afterwards. The precipitate was washed with diethyl ether three times and dried overnight. The readily synthesized MAI and $PbCl_2$ were mixed in 3:1 molar ratio in DMF. After optimization procedures, the most stable films in measurements conditions have been fabricated from 60 wt % precursor concentration.

The 15×20 mm glasses have been cleaned by sonication (10 minutes) with solution of Hellmanex 1 % and later rinsed with hot distilled water. Next, the substrates were placed in ultrasonic bath with isopropyl alcohol and later dried in air. The volume of 60 μL perovskite 60 wt % precursor has been spin–coated with 2100 rpm for 30 s onto the precleaned glasses. The film was annealed for 60 min in air at 100°C. At the substrate with perovskite layer, Al electrode has been thermally evaporated under vacuum 2×10^{-2} Torr with thickness of 50 nm. The mask was used to define two 3 mm electrodes with 3 mm width and 0.5 mm space in between which was an active area of the sample. Finally, the film has been covered with glass cover slips with epoxy resin to prevent the degradation process by contact with air and water during the process of measurements. The resin was placed in a way it did not contact an active area of the sample.

The structural characterization included X–ray diffraction (XRD) and Scanning Electron Microscope (SEM) measurements. XRD have been performed for samples spin–coated on the glass substrate in air using the X–Pert Pro MPD Philips diffractometer at room temperature with $Cu_{K\alpha}$ (1.542 Å). The accelerating voltage and electrical current were 40 kV and 30 mA, respectively. XRD data have been recorded from 10° to 60° for 2θ with the step size of 0.027°. To analyze the surface morphology and average crystallite size of perovskite films, the FEI Quanta FEG 250 SEM was used, operating with secondary electron detector in a high

vacuum mode with the accelerating voltage of 20 kV. The actual thickness of a spin–coated perovskite layer on the substrate with the aluminum electrodes has been measured with the use of surface Tencor Alpha Step 500 Profiler.

The temperature dependence of conductivity has been studied by DC two–wire (2W) method in a temperature range of 77–420 K. In order to perform the DC Hebb–Wagner polarization technique, the thick and dense layer of ion–blocking electrode (a carbon paste from Leit C Conducting Carbon Cement) has been covered on the aluminum electrodes. For the non ion–blocking electrode, a porous silver paste was used as a current collector which was previously reported by Maeda et al. [142]. The platinum wires were used as electrical connections. To control the temperature, K–type thermocouple (Keysight 34970A) has been placed right beside the sample in the holder. In the first part of the experiment, the measurement cell was located in the tube immersed in a liquid nitrogen. Then the temperature slowly increased. At a high temperature regime (above a room temperature), the tube was heated on the hot–plate as it reached aimed temperature. We did not illuminate our samples during experiment (dark conditions). Performing the electrical measurements (Keithley 2401), the current–voltage characteristics have been taken under steady–state conditions. The conductivities were calculated from the J–V linear relations at low–voltage region.

In order to analyze the crystal structure and phase composition of the samples, the XRD measurements were conducted. In Figure 4.15(a) there is shown X–ray diffraction pattern for the $CH_3NH_3PbI_{3-x}Cl_x$ film on glass substrate which exhibits tetragonal structure with a *I4cm* symmetry [29]. The following diffraction peaks corresponding to (110), (200), (211), (220), (310), (312), (224), (330) and (440) planes of perovskite material were observed [143, 144]. The highest intensity of 13.93° peak suggests that the orientation of the polycrystalline perovskite film is (110) [145]. In the diffraction pattern, there is no secondary phase from PbI_2 at 12.3° which suggests high purity of the sample [146]. The degradation effect with the XRD has been measured for one sample, results are shown in Figure 4.15(b). After three weeks from preparing of the sample, there are no visible impurities from PbI_2.

The active area of samples is defined in between two parallel electrodes. From the observation of the surface morphology, we can clearly see a percolation path for charge carriers between crystallites, Figure 4.15(c). Therefore, the method of spin–coating for a film formation is good enough for the purpose of the work. The grain size of the polycrystalline material (3.3 ± 0.6) μm has been estimated from the analysis of SEM image. The thickness of the sample obtained from profilometer is (1.80 ± 0.07) μm. The ratio of grain sizes to grain boundaries is very high, therefore we may ignore the influence of partial grain boundary conductivity on total conductivity in the further part of the studies.

4.2.2 Experimental studies of ionic conductivity

In order to check the electrical properties of the $CH_3NH_3PbI_{3-x}Cl_x$ material, the temperature dependence of total and partial surface conductivities have been measured. The total conductivity (σ_{tot}) of material is defined as a sum of electronic and ionic conductivities

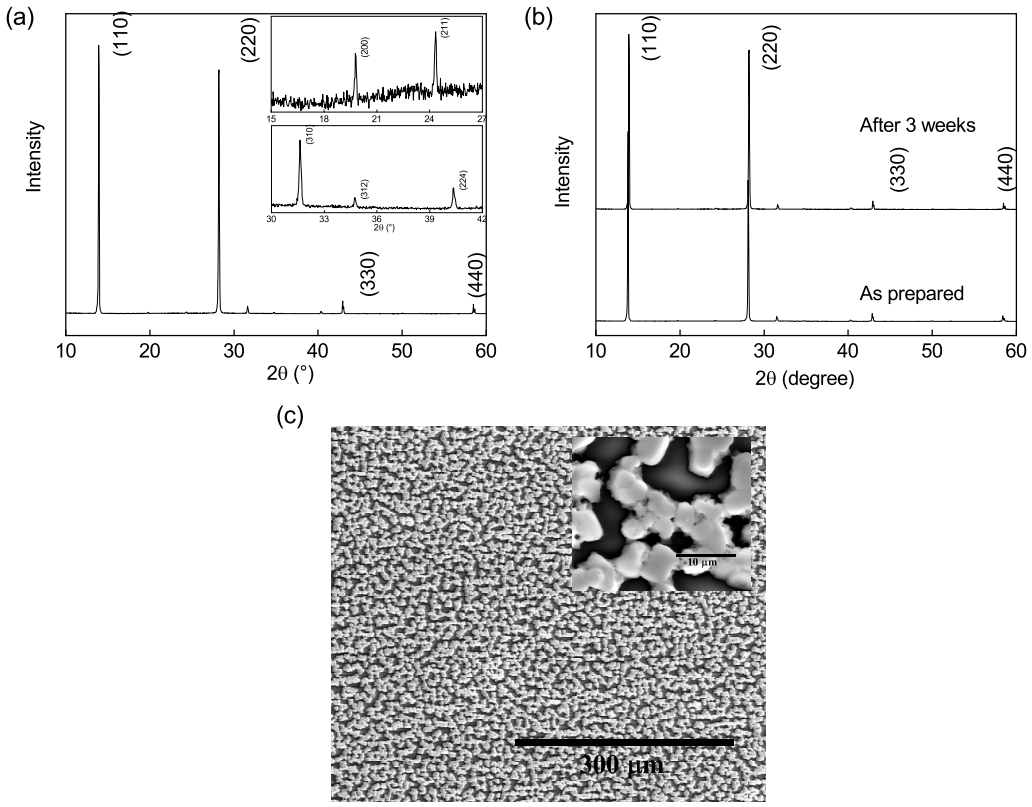

Figure 4.15: Structural results for $CH_3NH_3PbI_{3-x}Cl_x$ sample. a) X–ray diffraction pattern, b) X–ray diffraction pattern with degradation results measured just after the sample was prepared and after three weeks, and c) Scanning Electron Microscopy (SEM) image.

$$\sigma_{tot} = \sigma_{el} + \sigma_{ion}, \tag{4.6}$$

where electronic conductivity (σ_{el}) is associated with electrons and holes, and ionic conductivity (σ_{ion}) relates, in general, to anions and cations.

It should be mentioned that $CH_3NH_3PbI_{3-x}Cl_x$ perovskite is a material with addition of chloride salts to precursor for film fabrication. It is known, that the addition of chloride ions improves the stability against humidity [147]. However, only small amount of Cl atoms are present in mixed–halide film [148] and, the chloride doping has a small impact on transport properties [149]. Therefore, only iodide ions are considered in partial conductivity of the studied material.

The technique for measuring total conductivity possible to use only when steady–state condition of the sample is reached. Therefore, in Figure 4.16 it is shown J–V characteristics which have been taken before immersing the sample to liquid nitrogen (part a), and just after the room temperature has been reached (part b). The stability analysis were also done in low

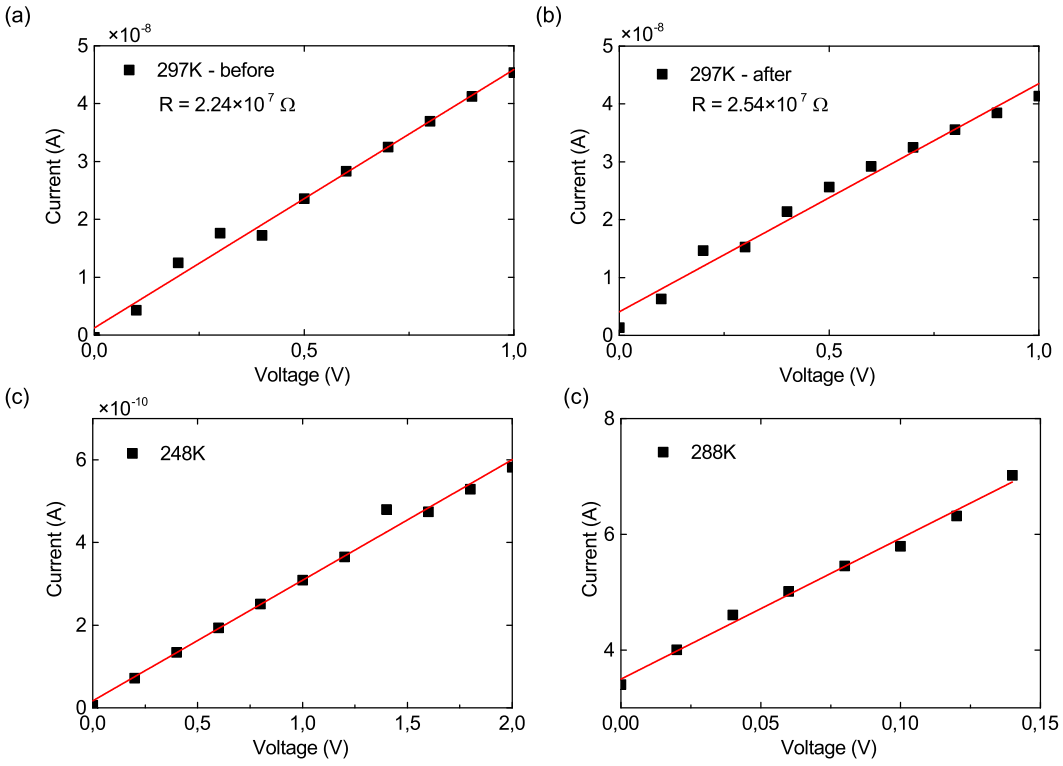

Figure 4.16: J-V curves for $CH_3NH_3PbI_{3-x}Cl_x$ sample. a) before immersing to liquid nitrogen, b) instantly as room temperature has been reached, c) in 248K, and d) 288K absolute temperature. The corresponding linear fitting red line is shown.

temperature for a few hours (results not shown here). The lack of differences support the conclusion that the steady-state is obtained for every point of measurements. The conductivity has been calculated from linear fitting of J–V characteristics. In Figure 4.16(c,d), there are presented two example measurements for different applied voltage ranges which show linear relation with current. The two–points method is used instead of the four–point (4W) due to the large resistance of the sample in the contrast to wires. All of the measurements exhibit the same tendency, thus only one representative result is presented in this work.

Figure 4.17(a) shows the result of the total conductivity in 80–420 K temperature range. Ten samples were measured in the same conditions with 2W method. At low temperature, we notice a value of conductivity characteristic for insulator materials: 1.77×10^{-6} S m^{-1}. The drastic rise of the total electrical conductivity level is observed at 230 K and at 300 K. It reaches 2.4×10^{-2} S m^{-1} which is of the same order of magnitude as previously reported for trihalide perovskite by Maeda et al. [142]. It should be also mentioned that the significant increase of total conductivity, by about four orders of magnitude, for transition from orthorhombic to tetragonal phase has been also observed by Khenkin et al. [150] and Peng et al. [151]. Slightly over the room temperature, the conductivity decreases up to 340 K and continues to increase

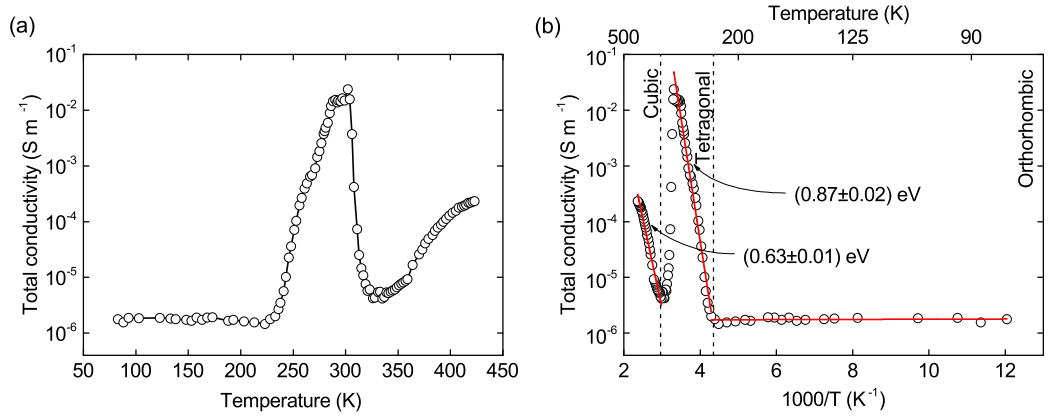

Figure 4.17: The temperature dependence of total electrical conductivity for $CH_3NH_3PbI_{3-x}Cl_x$ sample. (a) Conductivity as a function of temperature in absolute scale, and (b) Arrhenius plot of total conductivity with activation energy given for each crystallographic phases.

afterwards. Such a significant change in electrical conductivity as a function of temperature may be explained by the phase transition which occurs in the sample.

In order to calculate an activation energy (E_a) for conductivity with temperature, we use the Arrhenius equation

$$\sigma = \sigma_0 \exp\left(-\frac{E_a}{k_B T}\right), \tag{4.7}$$

where σ is a conductivity of the sample and σ_0 represents a pre–exponential factor. Figure 4.17(b) illustrates the total conductivity vs 1000 T^{-1} for the analyzed sample. As can be seen, the linear fitting is in a good agreement with Equation 4.7, what proves the validity of thermally active conductivity model. Moreover, the three characteristic regimes can be visible in Figure 4.17(b). These regimes are related to the phase transitions and, in a consequence, to different crystal forms of the same sample. For the seek of this chapter, the orthorhombic, tetragonal and cubic phases are also called α, β and γ, respectively.

At low temperatures, we notice a negligible change of the total electrical conductivity as the temperature increases, see Figure 4.17(b). Therefore, a very small (even close to zero) activation energy for mixed conductivity has been obtained at α phase. The drastic increase of conductivity occurs at the transition from α to β phase which leads to higher activation energy (0.87 $\pm$ 0.02) eV. The transition for trihalide perovskite is expected at 160 K. However, Li et al. [152] have presented that the increasing of sample thickness (a distance between electrodes for the volume electrical conduction) from 30 nm to 400 nm can drastically change the temperature of the transition for about 40 K. The distance between both electrodes for our samples (a case of the surface conduction) is around 0.5 mm, what should lead to higher temperature of the phase transition (in our case $\sim$230 K). It is known that the electronic conductivity depends on the mobility of charge carriers. However, Milot et al. [24] have re-

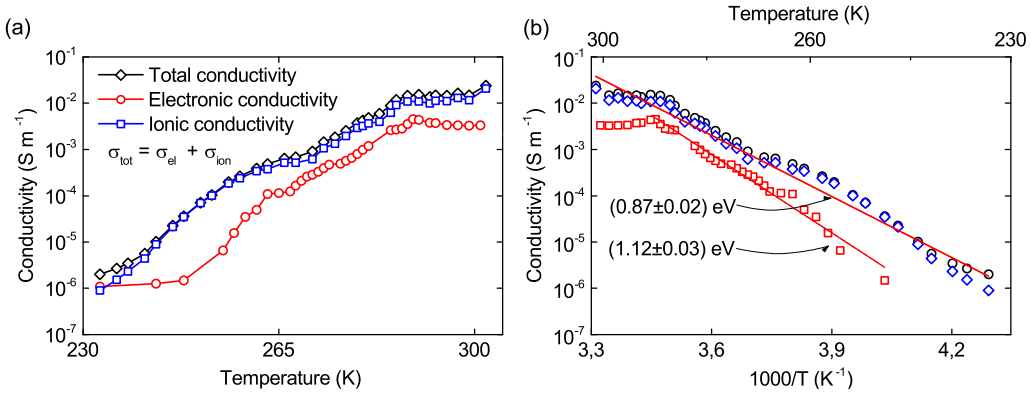

Figure 4.18: The total conductivity and partial electronic and ionic conductivities presented for β phase of $MAPbI_{3-x}Cl_x$ sample. (a) Conductivities as a function of temperature in absolute scale, (b) Arrhenius plot for partial ionic and electronic conductivities.

ported that the mobility decreases for the transition from orthorhombic to tetragonal phase. Therefore, the change of conductivity should be related to the change of charge carriers concentration. The α and β phases are characterized by the symmetries *Pnma* and *I4cm*, respectively. A change of the symmetry in phase transition could explain the increase of electrons and holes concentration [153]. For higher temperature, we have recorded a phase transition from β to γ associated with the decrease of activation energy (0.63 ± 0.01) eV. Additionally, the total conductivity drops by about two orders of magnitude, illustrated in Figure 4.17(b). It also seems that the change of perovskite phase is spread over a wide range of temperature. Therefore, it may suggest presence of two phases in temperature between 300K to about 340K [25, 63, 154].

It is possible to separate the ionic and the electronic conductivities using the modified DC Hebb–Wagner polarization method under the steady–state condition. The temperature dependences of σ_{tot}, σ_{el} and σ_{ion} for tetragonal phase are shown in Figure 4.18. The representative results for the total and electronic conductivities are presented without and with the ion–blocking electrode, respectively. For β phase the ionic conductivity takes over the dominance in $CH_3NH_3PbI_{3-x}Cl_x$ perovskite, Figure 4.18(a). Then, the partial conductivity of iodide ions is one order of magnitude higher than electronic conductivity at room temperature. In case of an intrinsic semiconductor with wide band–gap, the electronic conductivity should be close to zero at 300K. This could be explained with unintentional doping level (E_c-E_f) which according to Kim et al. [155] is shallow as 0.34 eV below conduction band (E_c) for $CH_3NH_3PbI_3$. The electron concentration generated by unintentional doping is given by Boltzmann statistics

$$n_0 = N_c \exp\left(-\frac{E_c - E_f}{k_B T}\right), \tag{4.8}$$

where N_c is an effective density of states in conduction band equal to 8.1×10^{24} m^{-3} [48].

Equation 4.8 gives n_0 concentration equal to 1.57×10^{19} m^{-3} and with electron mobility equal to 35 cm^2 V s^{-1} [24], the electron conductivity is 8.83×10^{-3} S m^{-1} which is about the experimental data at 300K, see Figure 4.18. In reference to these results, it can be stated that $CH_3NH_3PbI_{3-x}Cl_x$ is a mixed ionic–electronic conductor with predominant iodide ions conductivity at tetragonal phase. We suggest that the domination of ions at room temperature may explain the observed effect of hysteresis in trihalide perovskites.

The activation energies for both partial conductivities have been calculated from Equation 4.7. The linear correlation coefficient for Arrhenius plot is 0.97. Figure 4.18(b) shows that, for tetragonal phase, the activation energy drastically increases for both ionic and electronic charge carriers to the values of (0.87 $\pm$ 0.02) eV and (1.12 $\pm$ 0.03) eV, respectively. The obtained result of the activation energy for migration of iodide ions is similar to previous reports for the halide inorganic perovskites with anion vacancy transportation mechanism [120, 156, 157] and for the methylammonium lead iodide perovskite [122]. We can see that the ionic conductivity dominates for β phase. However, its activation energy is lower in respect to the electronic conductivity. Eames et al. [122] have assumed that the only possible mechanism for transport of ions in $CH_3NH_3PbI_{3-x}Cl_x$ perovskite is by hopping between the neighbouring vacancies which needs low activation energy. Motta et al. [149] have proposed that the bottom of conduction band and the top of valence band for $CH_3NH_3PbI_{3-x}Cl_x$ originate from p orbitals of Pb atom and p orbitals of I atom, respectively. Therefore, the creation of electrons and holes and, as a consequence, also their transport (the bandpass transportation mechanism) require a higher thermal energy. That may explain the higher value of activation energy observed for the electronic conduction in comparison to the ionic conduction mechanism.

Chapter 5

Studies of surface recombination in perovskite solar cells at the interface of HTL/$CH_3NH_3PbI_3$

The theoretical calculations have shown that the highest power conversion efficiency of perovskite solar cells could be around 31% [158]. Although it can be found that the best cells have already reached a maximum of a short–circuit photocurrent (J_{sc}) [159], there are still observed losses in a fill–factor (FF) and an open–circuit voltage (V_{oc}) related to the optical losses, the recombination processes and the transport of charges within different layers and through the interfaces. Therefore, further studies are required to specify which dominant recombination mechanism limits all photovoltaic parameters (J_{sc}, FF and V_{oc}) in order to control them.

In the PSCs, a radiative recombination of charge carriers seems not to play a dominant role in comparison to a nonradiative recombination mechanism [160, 161]. The nonradiative recombination takes place when the trapped electron (or hole), which is located at the energy level within the band–gap, recombines with an opposite charge carrier. However, the traps could be accumulated either at the grain boundaries of the polycrystalline perovskite material [162] or at the interface between the perovskite and an electron transporting layer (ETL) or a hole transporting layer (HTL) [163]. It seems that both types of accumulation should exist in the PSCs and impact the final performance [160, 164].

In general, an interface (dead) recombination is well known to impact the properties of the solar cells [165, 166]. However, only recent studies have reported the importance of this type of recombination in PSCs [167–169]. The presence of surface recombination is inherent to a perovskite material as perovskite crystals grow depends on the quality of the layer which is underneath. Nakane et al. [170] have shown that a growth of the perovskite on TiO_2 could result in the creation of a "dead layer" which is parasitic for the perovskite with a very high recombination leading to decrease of J_{sc} and, as a consequence, lowering the final performance of PSCs. Fortunately, several techniques have been already presented to reduce the surface

recombination by e.g. temperature treatment [171], chemical passivation [172, 173] or laser treatment [174].

The aim of this chapter is to investigate and understand the role of recombination processes which occur at the interface of HTL/perovskite. Therefore, the experimental part is firstly described, where we study two types of PSCc with and without interface recombination layer. Further, the representative cells are simulated with the drift–diffusion model to deeply understand the nature of the aforementioned recombination process.

This chapter is partially based on [D. Głowienka, D. Zhang, F. D. Giacomo, M. Najafi, S. Veenstra, J. Szmytkowski, Y. Galagan *Role of Surface Recombination in the Interface of Cu:NiO_x/$CH_3NH_3PbI_3$ Perovskite Solar Cells*, submitted].

5.1 Device fabrication

The precursor for perovskite $CH_3NH_3PbI_3$ phase was prepared as described below. Commercial lead iodide (PbI_2) (99.99%, TCI), methylammonium iodide (MAI) (GreatCell Solar), dimethylformamide (DMF) solvent (99.8%, Sigma-Aldrich) and 1-methyl-2-pyrrolidinone (NMP) solvent (99.5%, ACROS Organics), were used as received. The powders of MAI and PbI_2 were mixed in 1:1 molar ratio and dissolved in DMF:NMP (9:1 volume ratio) solution by stirring overnight at room temperature. Three precursors solutions with 1 M, 1.2 M and 1.4 M equimolar concentrations were used in experiment. Patterned glass/ITO substrates were ultrasonically cleaned with soap water, deionized water, and ethanol, followed UV–ozone treatment for 30 min. All the solar cells preparation processes were carried out inside the nitrogen–filled glove–box with oxygen and moisture levels about 1 ppm. The HTL of Cu:NiO_x was prepared from 0.95 mmol $Ni(NO_3)_2 \cdot 6\,H_2O$ and 0.05 mmol $Cu(NO_3)_2 \cdot 3\,H_2O$ powders mixed in 9:1 volumetric ratio of 2-methoxyethanol solution and acetyloaceton solutions, recpectively. The Cu:NiO_x was spin–coated at 1500 RPM for 60 s with acceleration 1500 RPM s^{-1}. It was dried on hot–plate for 5 min at 150°C in N_2 environment, and further for 15 min at 300°C in air. The surface passivation of Cu:NiO_x has been done with poly(triaryl amine) (PTAA) (Sigma-Aldrich) solution in toluene with the concentration of 2 mg mL^{-1}. The solution was spin–coated at 5000 RPM for 35 s with the acceleration of 5000 RPM s^{-1}. Then samples were annealed at 100°C in N_2 for 10 min. Subsequently, the perovskite solution was dynamically spin–coated with the following gas quenching [175]. The 100 μL precursor was spin–coated on glass substrate in two steps. First, at 2000 RPM for 10 s with acceleration 200 RPM s^{-1} and, then at 5000 RPM for 30 s with 2000 RPM s^{-1}. After 15 s of spin–coating, the N_2 gun was used for quenching the perovskite layer for 15 s at 6 bars pressure with 10 cm vertical position from the substrate. Afterwards, the samples were immediately placed on the hot–plate at 100°C for 10 min. The ETL solution was prepared by dissolving 20 mg mL^{-1} of [6,6]-phenyl C61 butyric acid methyl ester (PCBM) (99%, Solenne) in chlorobenzene, the solution which was stirred overnight at 60°C. ETL layer was spin-coated at 1500 RPM for 55 s with the acceleration of 3000 RPM s^{-1} and followed by spin–coating of bathocuproine (BCP) (99.99%, Sigma-Aldrich) solution of 0.5 mg mL^{-1} in

ethanol at 3000 RPM for 50 s with the acceleration of 3000 RPM s^{-1}. Subsequently, the cleaning of ITO contacts from HTL, the perovskite and ETL layers was done in air with the use of DMF:chlorobenzene solution in 1:6 volume ratio. Finally, Au electrodes were thermally deposited with a thickness of 100 nm under the pressure of 1×10^{-6} mbar through a shadow mask on top of the ETLs.

5.2 Characterization methods

The film thickness of each layer was measured with Bruker XT Dektak profilometer giving for the $CH_3NH_3PbI_3$ perovskite material 375±5 nm, 470±2 nm and 575±4 nm for 1 M, 1.2 M and 1.4 M molar concentrations, respectively. The crystal structure characterization was performed using X-ray diffractometer (PanAlytical Empyrean; referred as XRD). The morphology was investigated with atomic force microscope (Park NX-10 tool; referred as AFM). The optical properties of the samples were measured with UV–vis spectrophotometer (Agilent Cary 5000) by measuring the transmittance (T) and the reflectance (R). Steady–state photoluminescence spectrum (Horiba Labram Aramis system; referred as PL) was measured with an excitation laser beam at 532 nm and Si detector. The current–voltage (J–V) characteristics of solar cells were measured in N_2 filled glove–box under a white light halogen lamp using illumination mask of 0.09 cm^2, to define the active area of the sample. The light intensity was calibrated to 100 mW cm^{-2} with a silicon reference cell. However, for obtaining different illuminations, the set of filters have been used to obtain 1, 0.83, 0.53, 0.33, 0.1, 0.01 and 0.001 sun intensities. The J–V curves were measured with Keithley 2400 with a scanning rate of 0.165 V s^{-1} with 20 mV step. The scanning was performed in forward (from -0.1 V to 1.1 V) and reverse (from 1.1 V to -0.1 V) bias to show the effect of hysteresis. The measurements of J–V characteristics were done without preconditioning with light soaking or UV treatment. The maximum power point tracking (MPPT) was performed for approximately 2 minutes with continuous illumination, and control of voltage and current at maximum power point. The external quantum efficiency (EQE) was measured with setup from Rera Solutions.

5.3 Experimental results

The optical analysis performed with UV–vis and PL measurements is shown in Figure 5.1(a,b). For the UV–vis experiment, the transmittance (T) and reflectance (R) of the samples have been measured and recalculated to the absorbance using a relation of 100%=A+T+R, the resulted absorbance is shown in Figure 5.1(a). Using the tauc–plot, the optical band–gaps (E_g) have been obtained, which values were further applied in the simulation. The E_g values of 1.601 eV, 1.595 eV and 1.591 eV were obtained for the thicknesses of 375 nm, 470 nm and 575 nm, respectively. The same shift of the band–gap is observed in PL measurements when a film thickness increases, see Figure 5.1(b). The possible explanation of the effect is

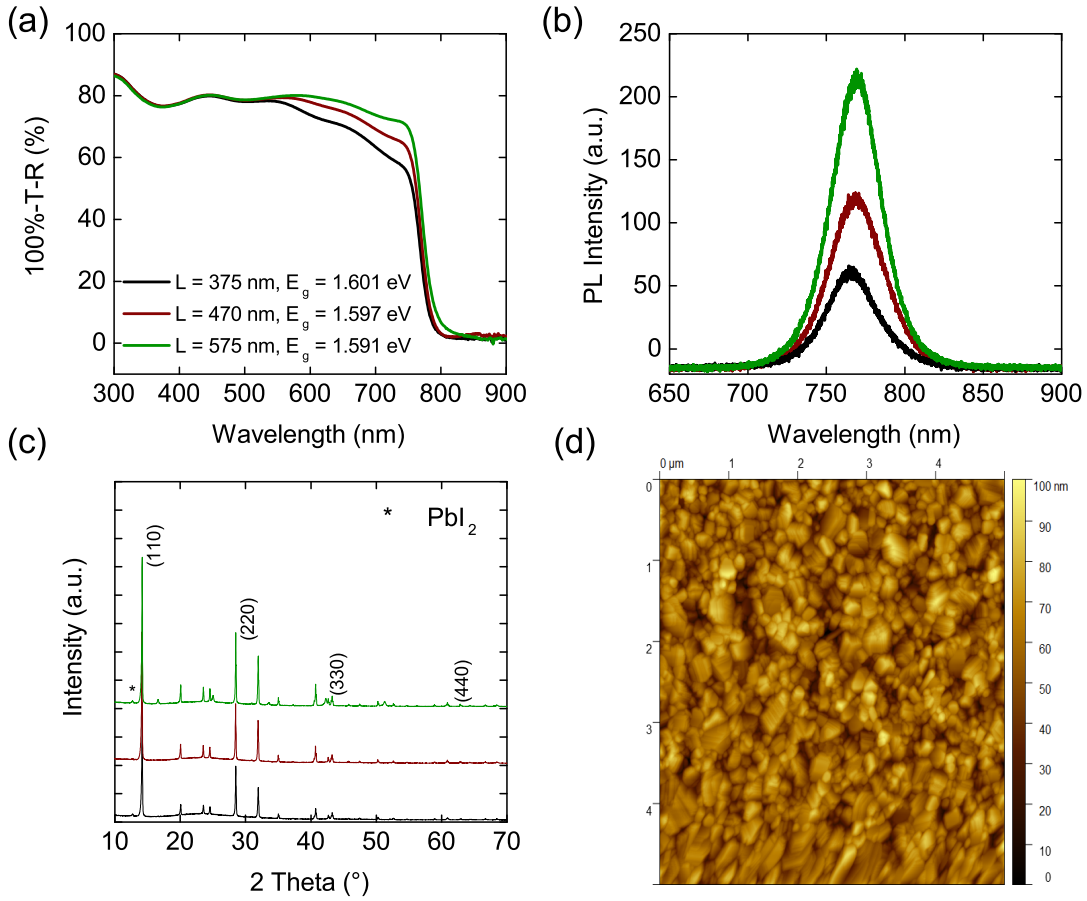

Figure 5.1: Experimental results for the perovskite layer on glass, a) UV-vis, b) PL, c) XRD, and d) AFM measurement. The perovskite thickness is equal to 375 nm (black line), 470 nm (red line) and 575 nm (green line). Only 375 nm perovskite layer is shown for AFM analysis.

in–plane tensile strain perpendicular to the substrate which increases with film thickness and may impact the band–gap [176].

In order to characterize a crystal structure of the perovskite layer, the XRD measurements have been performed. Figure 5.1(c) illustrates the XRD results of the perovskite which show negligible differences for three different thicknesses. The samples exhibit tetragonal phase with *I4cm* symmetry, which is confirmed by the diffraction peak with highest intensity of (110) [115]. Most importantly, in all three samples, we can see a very small diffraction peak observed at about 13° related to a secondary PbI_2 phase. The morphology of $CH_3NH_3PbI_3$ material is analyzed on the glass substrate with AFM measurements, see Figure 5.1(d). The result is only shown for 375 nm perovskite layer due to negligible differences. The layers exhibit a very good coverage with the large grains of approximately 215 nm, 226 nm and 239 nm (statistics done on about 150 grains) for 375 nm, 470 nm and 575 nm thick layers, respectively.

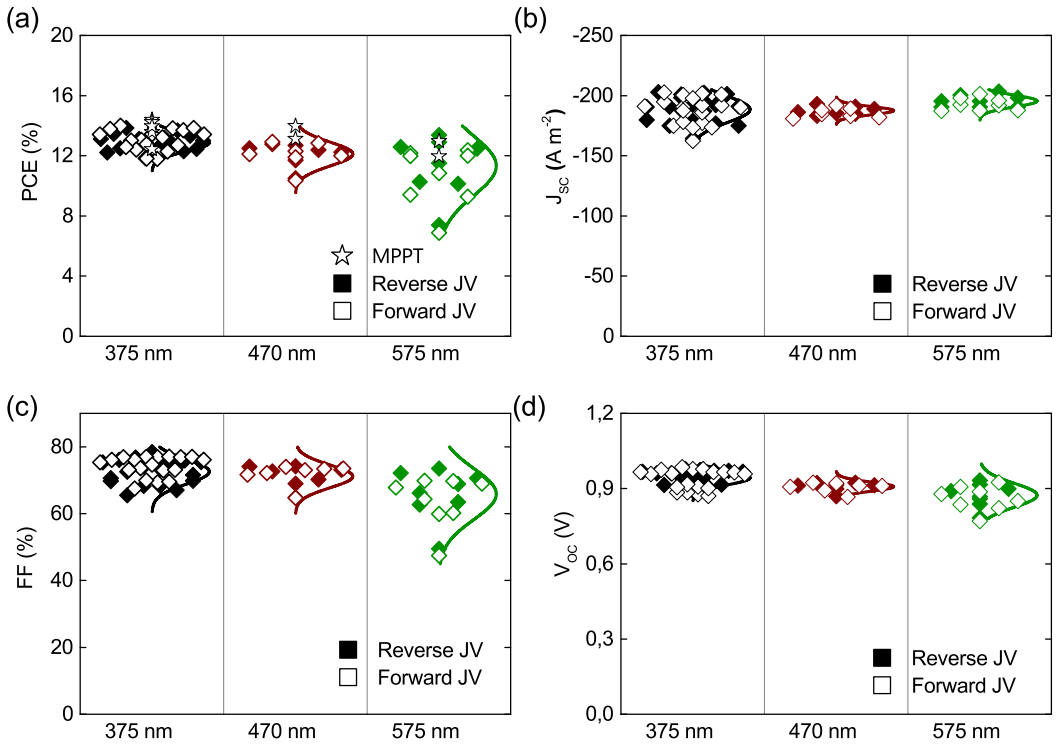

Figure 5.2: Photovoltaic parameters for PSCs, a) PCE, b) J_{sc}, c) FF, and d) V_{oc}. The solar cell structure with Cu:NiO_x as HTL. The perovskite thickness equals to 375 nm (black), 470 nm (red) and 575 nm (green).

The PSCs have been measured under AM1.5 conditions. Figures 5.2–5.3 show the results for the PSCs with the perovskite thickness of 375 nm, 470 nm and 575 nm for structure with Cu:NiO_x and Cu:NiO_x/PTAA, respectively. It has been observed that the sample without PTAA material has PCE lower by about 2–3%, as shown in part (a). This behavior is mostly due to 1 mA cm^{-2} losses of J_{sc} and 100 mV of V_{oc}, see part (b and d), while FF remains the same for both devices [part (c)]. The same effect could be observed for the samples with thicker absorber layer of 470 nm and 575 nm. However, the losses on V_{oc} and J_{sc} increase with increasing the thickness of perovskite absorber. For the samples with perovskite thick-

Table 5.1: Photovoltaic parameters for the PSCs representative cells

	Cu:NiO_x		Cu:NiO_x/PTAA	
	Forward	Reverse	Forward	Reverse
J_{sc} [A m^{-2}]	-194.24	-194.92	-204.25	-204.48
V_{oc} [V]	1.00	1.00	1.07	1.08
FF [%]	76.20	75.13	75.75	75.88
PCE [%]	14.84	14.66	16.58	16.71

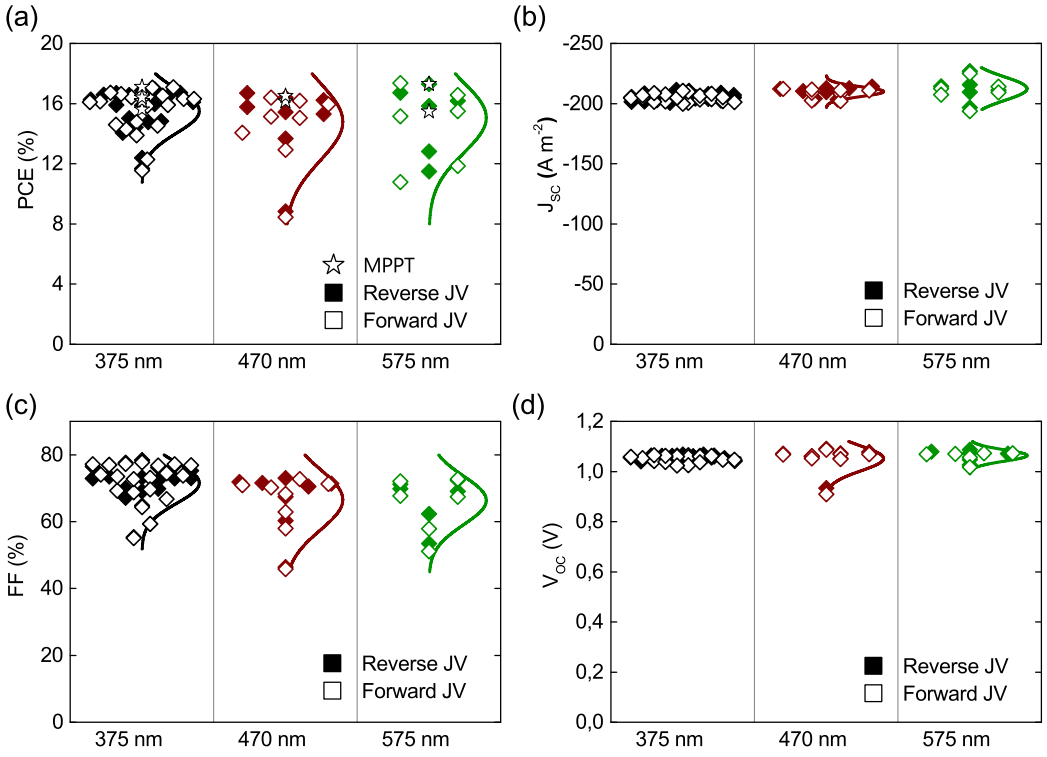

Figure 5.3: Photovoltaic parameters for PSCs, a) PCE, b) J_{sc}, c) FF, and d) V_{oc}. Solar cell structure with Cu:NiO_x/PTAA as HTL. The perovskite thickness equals to 375 nm (black), 470 nm (red) and 575 nm (green).

ness of 575 nm, the V_{oc} and J_{sc} drops are about 200 mV and 2 mA cm^{-2}, respectively, which results in approximately 4% of PCE losses. The PSCs with modified HTL maintain high PCE with slight increase in efficiency with increasing the perovskite layer thickness. This originates mostly due to higher J_{sc} which increases with increasing the absorber thickness due to higher absorption of light in the red part of the spectrum [177]. The observed parasitic phenomenon is likely related with surface recombination at HTL/$CH_3NH_3PbI_3$ interface as the only Cu:NiO_x has been modified. Such an effect has been already reported for perovskite solar cells [164]. However, for a high surface recombination, it is expected that FF also should be affected. In this study, we further demonstrate that the concept of a dead layer with a very high trap recombination is able to explain the losses in photocurrent and voltage with small impact on FF.

The representative J–V curves and External Quantum Efficiency (EQE) of the two types of devices with the perovskite absorber thickness of 375 nm are shown in Figure 5.4. For both cells, we can see relatively small hysteresis effect which suggests a good quality of the perovskite layer, see Table 5.1. This is very important for further simulation analysis, because it has been reported that the hysteresis is smaller for p–i–n structure which should be related to the interface defects that influence different rates of ion migration [160, 178]. Therefore,

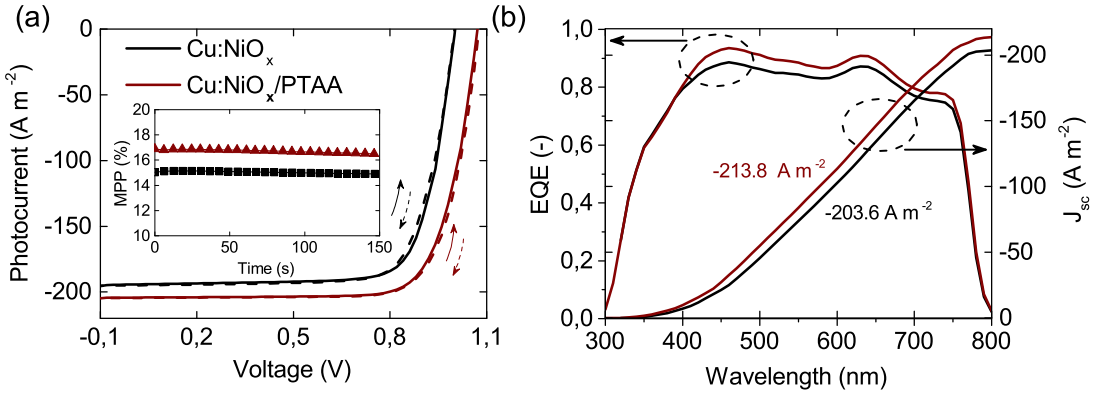

Figure 5.4: The experimental results for two PSCs. a) J–V characteristics for forward (solid line) and reverse (dashed line) scans with the inset of MPPT for the cells. b) EQE and integrated photocurrent of the cells. The absorber thickness equals to 375 nm. Red and black lines represent Cu:NiO_x with and without PTAA layer, respectively.

in the presented device configuration we can neglect the impact of ions. The result of maximum power tracking (MPPT) shows good light stability of the cells during 150 s of measurements under AM1.5 light spectrum [Figure 5.4(a-inset)]. Figure 5.4(b) illustrates the EQE for the same perovskite solar cells. It is observed that the EQE follows the absorbance from UV–vis measurements showing approximately the same absorption peaks. The differences could result from reflection effects. The total EQE is higher by about 5% for cell with PTAA layer which leads to increase of approximately 1 mA cm^{-2} (J_{sc}).

5.4 Theoretical model and parameters for the investigated devices

In this part, we explore the idea of surface recombination with the concept of a dead (recombination) layer which appears between Cu:NiO_x/$CH_3NH_3PbI_3$ and has a direct parasitic influence on J_{sc} and V_{oc}, and therefore on the efficiency of PSCs. Also, it is shown that a chemical modification of Cu:NiO_x with PTAA material reduces the parasitic effect in the absorber layer. The experimental results with different illumination conditions are used in the simulation to qualitatively verify the existence of a dead layer and explain its role in the PSC operation. For the simulation purposes, the drift–diffusion model has been applied. Finally, we show the influence of different thicknesses and surface recombination velocities on the operation of PSCs.

The drift–diffusion model used in this work describes generation, transport and recombination of charge carriers for the given stack. It also includes continuous equations to quantitatively describe the behavior of electrons

$$\frac{\partial n}{\partial t} = G - R_m - R_b - R_t + \frac{1}{q}\frac{\partial J_n}{\partial x}, \tag{5.1}$$

and holes

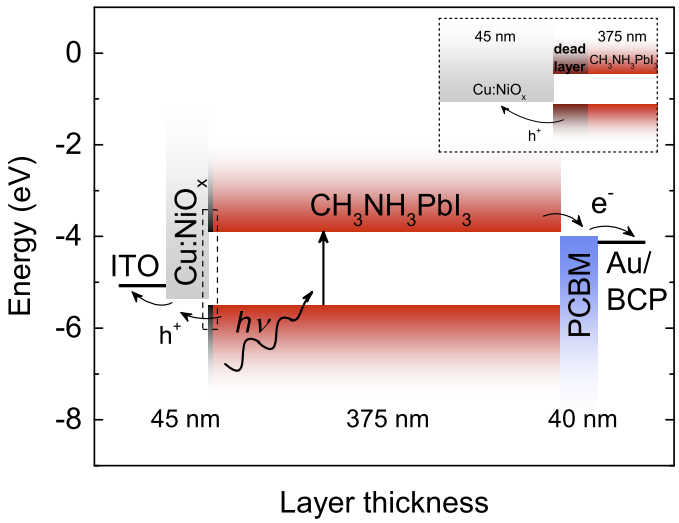

Figure 5.5: Device structure of PSC. After photon absorption, free electrons and holes are generated in the perovskite layer and transported to respective electrodes through ETL and HTL. The dead (recombination) layer is shown in the inset.

$$\frac{\partial p}{\partial t} = G - R_m - R_b - R_t - \frac{1}{q}\frac{\partial J_p}{\partial x}, \tag{5.2}$$

where $J_{n(p)}$ are electron and hole current densities given in Equations 2.8 and 2.9, respectively. The total generation G is calculated from the transfer–matrix method (Section 2.1.5). The sum of all recombination accounts for monomolecular (R_m) recombination with SRH model (Equation 2.25), bimolecular (R_b) recombination defined with Langevin model (Equation 2.36) and trimolecular (R_t) recombination described with Auger mechanism (Equation 2.38). In this study, the surface recombination is not two–dimensional as it is usually assumed. Instead, we take into account the existence of a three–dimensional parasitic layer with the same properties as the absorber, see Section 2.1.7.2. To simulate the dead layer, we put the surface recombination rate R_s (see Equation 2.34) instead of R_m within dead layer. The Poisson equation to calculate the electric field and potential

$$\frac{\partial^2 \varphi}{\partial x^2} = -\frac{q}{\varepsilon_0 \varepsilon_r}\left(p - n + N_D - N_A\right), \tag{5.3}$$

where the parameters N_D and N_A represent donor and acceptor concentrations in ETL and HTL layers, respectively.

In the simulation of the PSCs structure, the drift–diffusion model has been extended to simulate both transporting layers (ETL and HTL). The interfaces between the layers in the p–i–n structure lead to numerical difficulties, therefore the change in the permittivity has

Table 5.2: Parameters used in simulation of the perovskite solar cells. For better readability, parameters for holes and electrons are written in the brackets and without brackets, respectively.

	unit	ETL	perovskite	HTL
L	nm	40	375	45
N		20	60	20
ε_r		3.75	63	2.1
$\mu_{n(p)}$	$cm^2\ V^{-1}\ s^{-1}$	2×10^{-3}	24 (1)	(10^{-2})
$C_{n(p)}$	$10^{-14}\ m^3\ s^{-1}$	10^{-4}	5.56 (4.35)	(1)
N_t	m^{-3}	10^{22}	10^{21}	10^{22}
$\Gamma_{n(p)}$	$10^{-40}\ m^6\ s^{-1}$	4	1.55	(4)
ξ		10^{-4}	10^{-2}	10^{-4}
$E_{c(v)}$	eV	-4.0	-3.9 (-5.5)	(-5.35)
$N_{A(D)}$	m^{-3}	10^{20}	0 (0)	(1.4×10^{23})
$N_{c(v)}$	m^{-3}	2.5×10^{25}	8×10^{24}	(2.5×10^{25})

been included in the Poisson equation [82]. Also, the energy levels for electron and hole transporting layers are not aligned creating injection barriers (see Figure 5.5), which drastically influences the final performance of the solar cell. Therefore the method of generalized potentials has been used to include these variations, as shown in Section 2.3.

Figure 5.5 shows a band diagram of the investigated PSC, with the following layers sequence ITO/HTL/$CH_3NH_3PbI_3$/ETL/Au, where HTL is Cu:NiO_x with or without PTAA, and ETL is PCBM/BCP. In the current study, two variations of HTL so called Cu:NiO_x and Cu:NiO_x/PTAA were used. However, we treat PTAA as a passivation layer, and therefore it is not included in the electrical simulation model. Its influence is visible in the presence of a dead layer which grows only on pure Cu:NiO_x but not on PTAA passivated layer, Figure 5.5(inset).

Table 5.2 shows all parameters (if not specified otherwise) used for simulation of HTL, ETL and perovskite layer in PSCs. The thickness (L) is an experimental value because each layer was measured with a profilometer. The spatial grid was discretized with Chebyshev polynomials to reduce the number of grid points (N) needed for fast convergence of numerical simulations, Section 2.4.1. Relative permittivities (ε_r) for ETL and HTL have been calculated from optical η and κ parameters. For the perovskite material, Lin et al. [113] have shown that a dielectric constant is much higher than obtained from ellipsometry measurements, therefore we have decided to use a literature value [25]. Asymmetric mobilities for opposite charge carriers were chosen close to reference values with more mobile electrons (24 $cm^2\ V^{-1}\ s^{-1}$) than holes (1 $cm^2\ V^{-1}\ s^{-1}$) [21, 26]. Charge carrier capture coefficients ($C_{n(p)}$) used in the Shockley–Read–Hall recombination are close to literature values and they are equal to $5.56 \times 10^{-14}\ m^3\ s^{-1}$ and $4.35 \times 10^{-14}\ m^3\ s^{-1}$ for electrons and holes, respectively [47, 179]. The density of traps (N_t) is adopted from the literature [47]. The energy trap level has been fixed in the middle of an energy band–gap, which seems to be the most efficient [66].

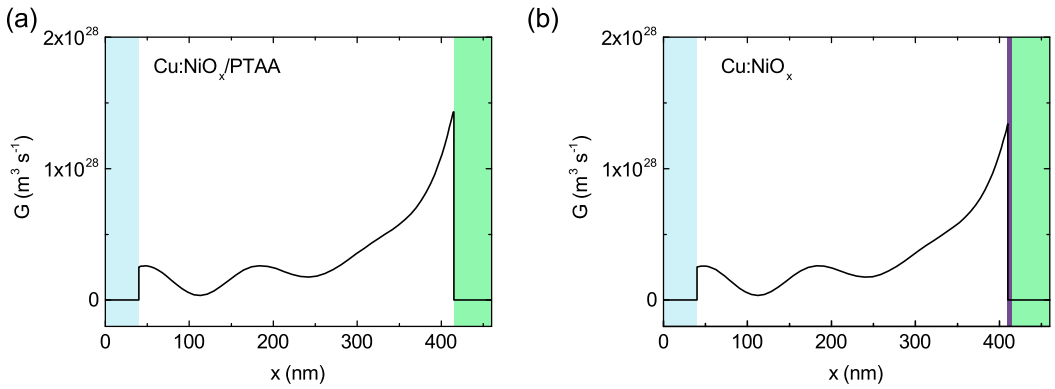

Figure 5.6: Generation (G) profile calculated using the transfer matrix model for the device architecture with a) Cu:NiO_x/PTAA (without dead layer), and b) Cu:NiO_x (with dead layer). Solar cell structure with PCBM (blue area), the perovskite (white area), dead layer (violet area) and Cu:NiO_x (green area). The perovskite thickness equals to 375 nm.

The bimolecular recombination is based on the Langevin model with reduction prefactor (ξ) adopted from the literature [47]. Although, the Auger recombination is the least dominant in perovskite materials, it has been used for clarity in the simulation tool with symmetric values of $\Gamma_{n(p)}$ adopted from the literature [24]. Energy levels for the bottom of the conduction band (E_c) and the top of the valence band (E_v) for the $CH_3NH_3PbI_3$ are aligned to the energy band–gap equal to 1.6 eV acquired from UV–vis and PL measurements, as shown in Figure 5.1 [180]. The injection barriers are associated with the Schottky contacts at the cathode/ETL and HTL/anode with values equal to 0.1 eV and 0.15 eV, respectively. The ITO material represents the anode contact, whereas BCP/Au acts as the cathode contact. BCP is used as a tunneling transport layer which adjusts the energy level of gold to reduce the contact losses. Therefore, we could simulate these two layers as one with fixed energy alignment [181]. In the perovskite layer, there is assumed no doping ($N_{A(D)} = 0$). The values of the effective density of states $N_{c(v)}$ have been adopted from the literature [164]. The simulation properties of ETL and HTL have been chosen to resemble PCBM [67, 164, 182–184] and Cu:NiO_x [185–188] materials. The simulation temperature of the solar cells has been used the same as in the experiment (295 K). The built–in voltage equals to 1.13 V is similar to the values from literature [50, 164].

5.5 Numerical results

The experimental J–V characteristics [see Figure 5.4(a)] have been used for the simulation process with the parameters given in the Table 5.2. The profile of charge carriers generation (G) has been calculated with the transfer matrix model, see Section 2.1.5. The obtained carriers generation profiles for both PSC structures with Cu:NiO_x and Cu:NiO_x/PTAA are presented in Figure 5.6. It should be mentioned that there is no charge carriers generation within a recombination layer [170]. Therefore, when integrating the generation profiles over

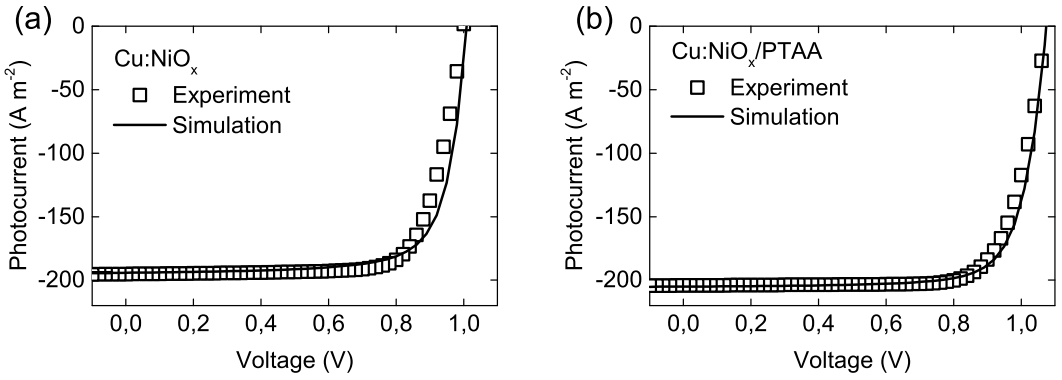

Figure 5.7: Photocurrent–voltage characteristics for experimental (square symbol) and simulation (solid line) results for a) Cu:NiO_x with 5 nm dead layer, and b) Cu:NiO_x/PTAA without dead layer. In the dead layer, the surface recombination velocities are equal to 3.75×10^3 and 3.75×10^4 m s^{-1} for electrons and holes, respectively. Other parameters used in simulations are the same for both devices and they are specified in Table 5.2.

the space dimension, we would acquire the loss of 1 mA cm^{-1} in simulated PSCs. Validation of the simulation model, which shows an excellent agreement with the experimental results is presented in Figure 5.7 for both PSCs structures. The shape of the J–V curve is not affect but shifted toward higher V_{oc} for sample with PTAA layer. Therefore, we will further focus only on open–circuit conditions.

The detailed simulations for both structures at the illumination of 1 sun are presented in Figures 5.8. At the open–circuit voltage (V_{oc}), we can see that high recombination in the dead layer drastically impacts on the charge carriers distribution not only at the interface but also in the bulk, see Figure 5.8(a). As a result of the shift in charge carrier densities, the electric field distribution has changed throughout the sample. It is due to a higher value of $|E|$ at the interfaces between perovskite/ETL and HTL/perovskite. However, the most relevant impact of the dead layer is visible on the photocurrent distribution which clearly shows the role of this recombination layer, as shown in Figure 5.8(c). It is observed that the electron and hole photocurrents reach high values at HTL/perovskite interface, however, very high recombination in the dead layer leads to abrupt loss of current. This effect is not visible in the sample without dead layer. Also, it should be pointed out that the photocurrent distribution in the PSC with the dead layer is reversible in comparison to a sample without this layer. This will be later explained in more details.

The well known fact is that the same shape of a fitting curve could be obtained for different sets of parameters. Therefore, simulation results are more precise when more physical variations are applied. For this reason, the range of measurements has been extended for the representative samples using light filters. Figure 5.9 shows the simulation results of the cell with Cu:NiO_x. These results are in excellent agreement with experimental results using the same set of parameters (Table 5.2) for a very wide range of the illumination profiles (0.001–1 suns). It should be mentioned that only the chosen parameters could simultaneously explain

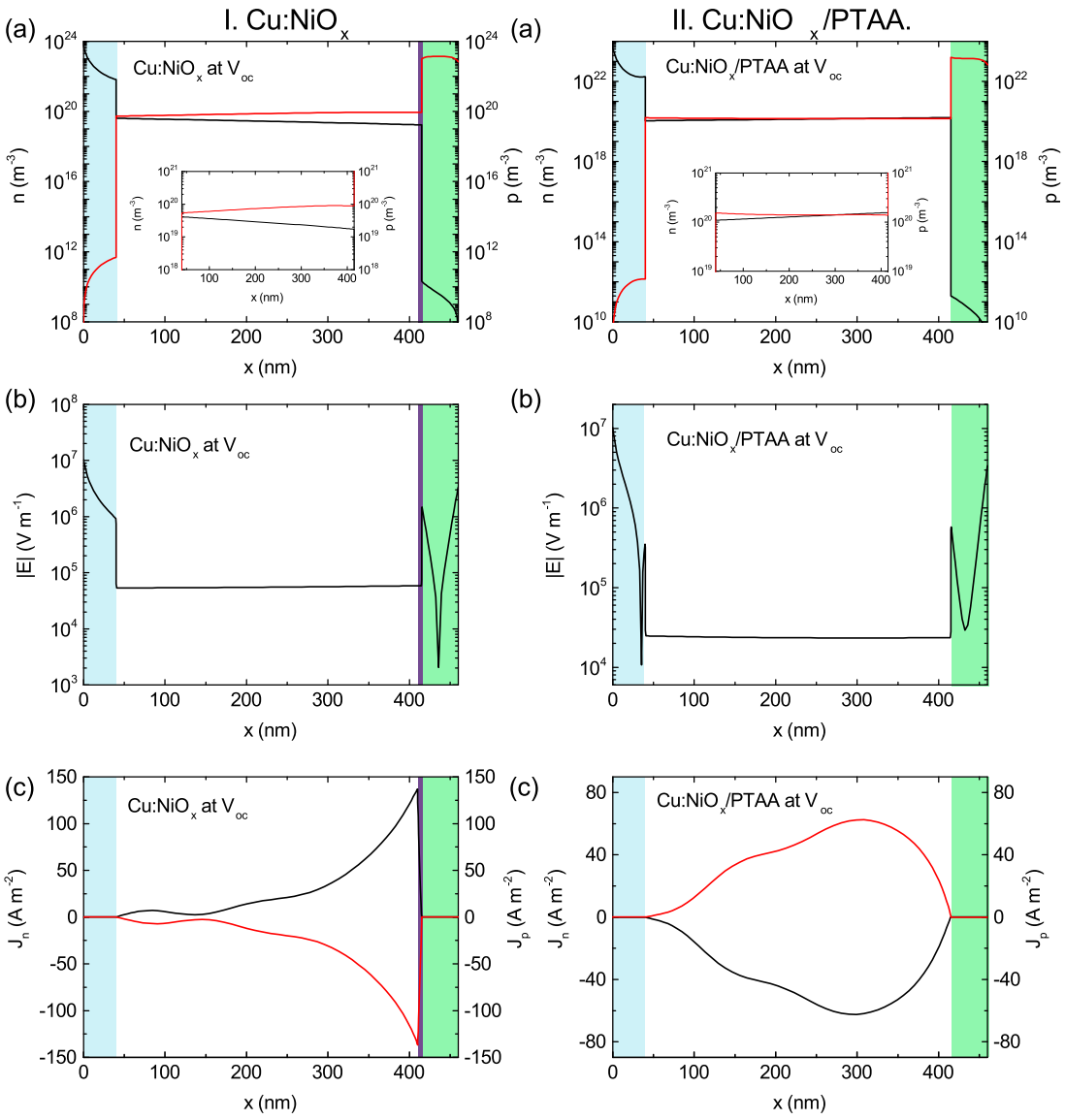

Figure 5.8: Spatial simulations carried for I) Cu:NiO_x (with dead layer), and II) Cu:NiO_x/PTAA (without dead layer). Spatial simulation results for an open–circuit voltage (V_{oc}) at 1 sun illumination, a) electron (black line) and hole (red line) density distributions, b) an absolute electric field distribution, and c) electron (black line) and hole (red line) photocurrents. Solar cell structure with PCBM (blue area), the perovskite (white area), dead layer (violet area) and Cu:NiO_x (green area). The parameters for part (I) and (II) are the same as used in Figure 5.7(a) and Figure 5.7(b), respectively.

all the variations including the surface passivation, the absorber thickness and the light intensity. Simulations have shown that the best fit for the dead (recombination) layer has been obtained if the thickness of dead layer is 5 nm and with the surface recombination velocities

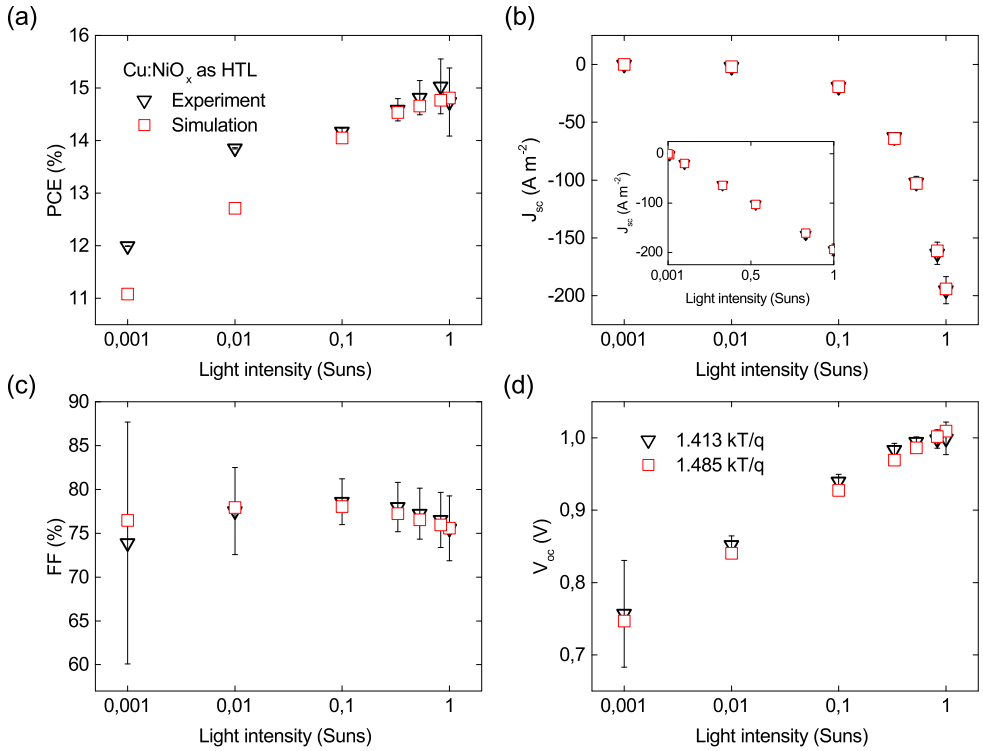

Figure 5.9: Photovoltaic experimental (black triangle symbol) and simulation (red square symbol) results for different illuminations. a) PCE, b) J_{sc} with the inset presented the same result using linear scale of the light intensity, c) FF, and d) V_{oc}. Solar cell structure with Cu:NiO$_x$ as HTL. Parameters are the same as used in Figure 5.6(a). 1 sun = 100 mW cm^{-2}.

equal to 3.75×10^{3} and 3.75×10^{4} m s^{-1} for electrons and holes, respectively. It is observed that holes recombine mostly in the dead layer. This effect originates from a location of the interface between the perovskite and HTL where more holes are present. Figure 5.9(a) shows the PCEs in respect to illumination. It should be noticed that the highest efficiency is reached at a light intensity of about 0.8 suns and starts to decrease for higher light intensities. The simulation results are in slight disagreement with the experiment at lower illuminations which are associated with almost dark conditions. In the Figure 5.9(b), the J_{sc} follows exactly the same trend for simulation and the experiment, which confirms a linear relationship between the current and light intensity in PSCs [189] and suggests that monomolecular recombination is dominant at a short–circuit [190]. The FF is the most sensitive photovoltaic parameter in simulation of solar cells. Even a slight change of any parameter in the numerical model may drastically change the final shape of the curve with different illumination intensities, Figure 5.9(c). Also, the general shape of FF suggests a competition of two dominant recombinations in the PSCs. We can see that the FF decreases monotonically above 0.1 suns which is related to bimolecular recombination or surface recombination. However, below 0.1 suns, the FF drops with a decreasing value of light intensity which should occur for a pure trap–

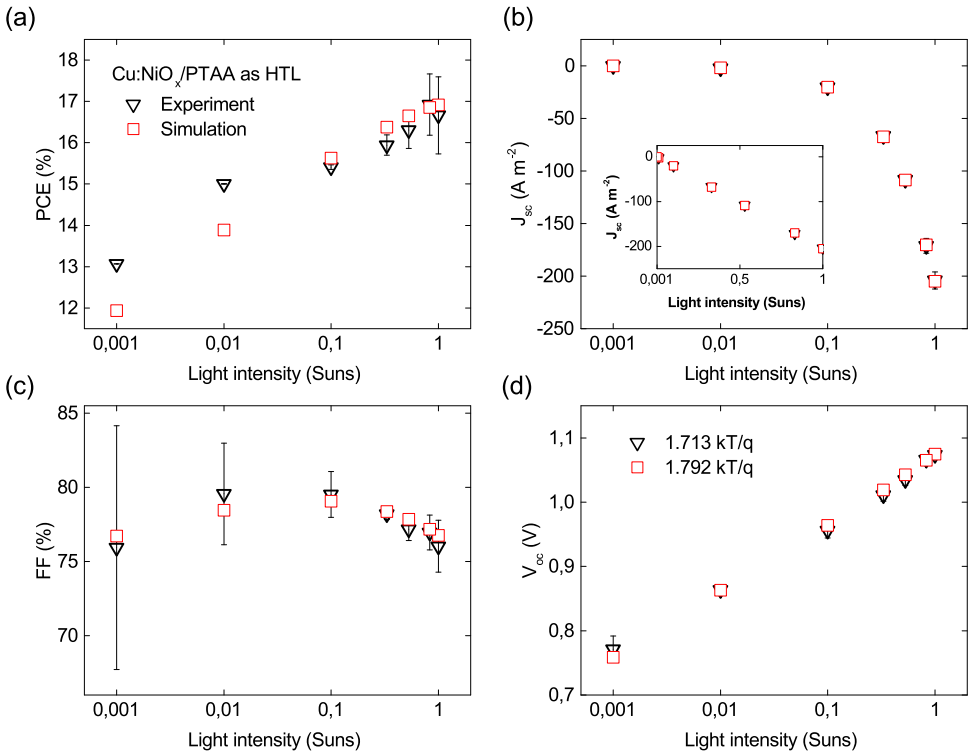

Figure 5.10: Photovoltaic experimental (black triangle symbol) and simulation (red square symbol) results for different illuminations. a) PCE, b) J_{sc} with the inset presented the same result using linear scale of the light intensity, c) FF, and d) V_{oc}. Solar cell structure with Cu:NiO_x/PTAA as HTL. Parameters are the same as used in Figure 5.7(b). 1 sun = 100 mW cm^{-2}.

assisted recombination [160]. Therefore, it is expected that charge carriers recombination is monomolecular for the low illumination. Also, a spread of the statistical bar at 0.001 suns should be related to the leakage current which has a higher impact on FF at low intensities [191]. Figure 5.9(d) shows the V_{oc} dependence from light intensity. The calculated ideality factors (n_{id}) for the experimental and simulation results are very similar suggesting a good choice of dominant recombination channel. According to Tress et al. [192], the surface recombination dominates if the ideality factor is closer to 1, which is mainly observed for lower built–in voltage in a perovskite material. Therefore, the acquired value of $n_{id} \approx 1.4$ proves the idea of a high recombination at Cu:NiO_x/$CH_3NH_3PbI_3$ interface. The small flattening of V_{oc} at high intensities should be also related to high surface recombination in the dead layer.

Figure 5.10 shows photovoltaic parameters as a function of light intensity for Cu:NiO_x/PTAA in the perovskite solar cell. The passivation with PTAA is assumed to reduce the surface recombination. Therefore in the simulation, we have used the same set of parameters but with a removed dead layer. The simulated and experimental results show a very good

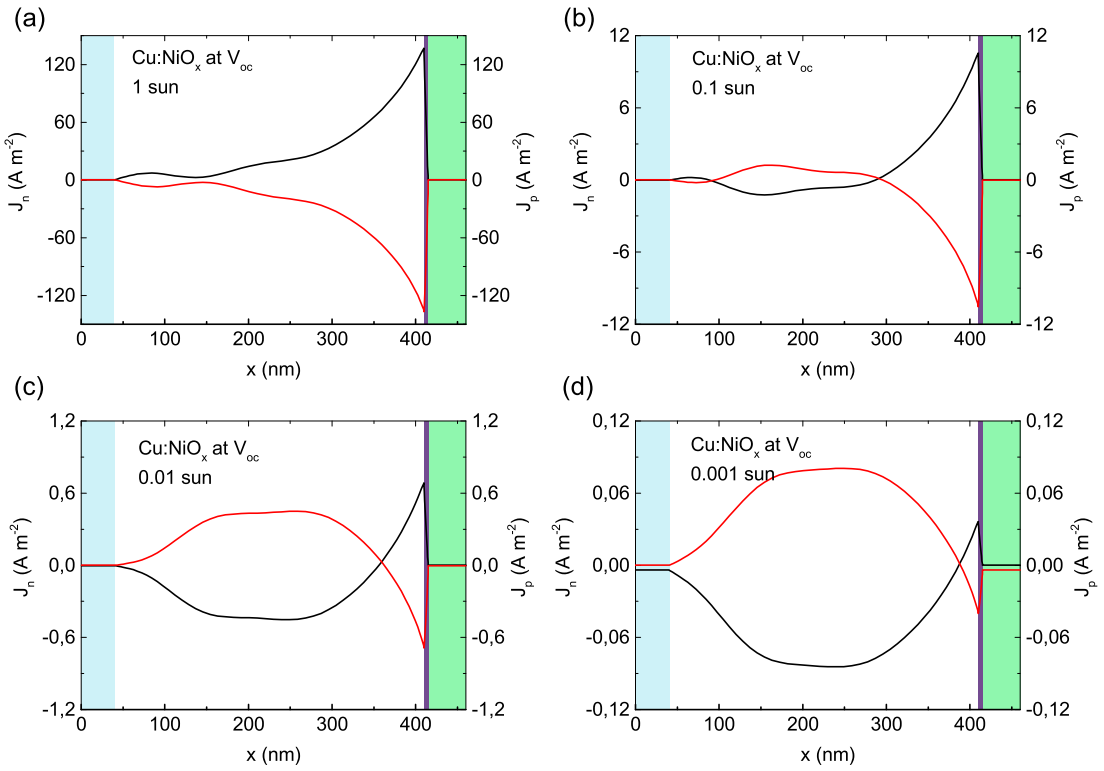

Figure 5.11: Spatial distributions of electron (black line) and hole (red line) photocurrents calculated for an open–circuit voltage (V_{oc}) at illumination equal to a) 1 sun, b) 0.1 sun, c) 0.01 sun, and c) 0.001 sun. All simulations are done for solar cell structure with dead layer (violet area) at the interface, and also with PCBM (blue area) and the perovskite (white area). All the parameters are the same as used in Figure 5.7(a).

agreement, which finally proves the existence of the dead layer at Cu:NiO_x. It appears to be the simplest way to improve the interface and remove the parasitic recombination. The PCE results for different illuminations are similar to the previous ones, however, lowered by about 2%, see Figure 5.10(a). Figure 5.10(b-inset) presents a linear trend of J_{sc} as a function of light intensity. It suggests monomolecular recombination as a dominant mechanism in this region. The FF in respect to the light intensity shows very similar behavior as PSC with the dead layer, as seen in Figure 5.10(c). However, there is no surface recombination in this system. Therefore the region above 0.1 suns, where FF starts to increase, should be associated with bimolecular recombination. At low illumination, monomolecular recombination still dominates. In Figure 5.10(d), n_{id} is approximately 1.7 at the open–circuit voltage. A value of the ideality factor closer to 2 confirms the existence of the trap–assisted SRH recombination as a dominant recombination channel in the bulk.

Figure 5.11 illustrates the simulation results for the PSC at different illumination intensities. The results are presented only for the current distribution which is a representative variable for the analysis of a dead recombination layer. It should be mentioned that the total

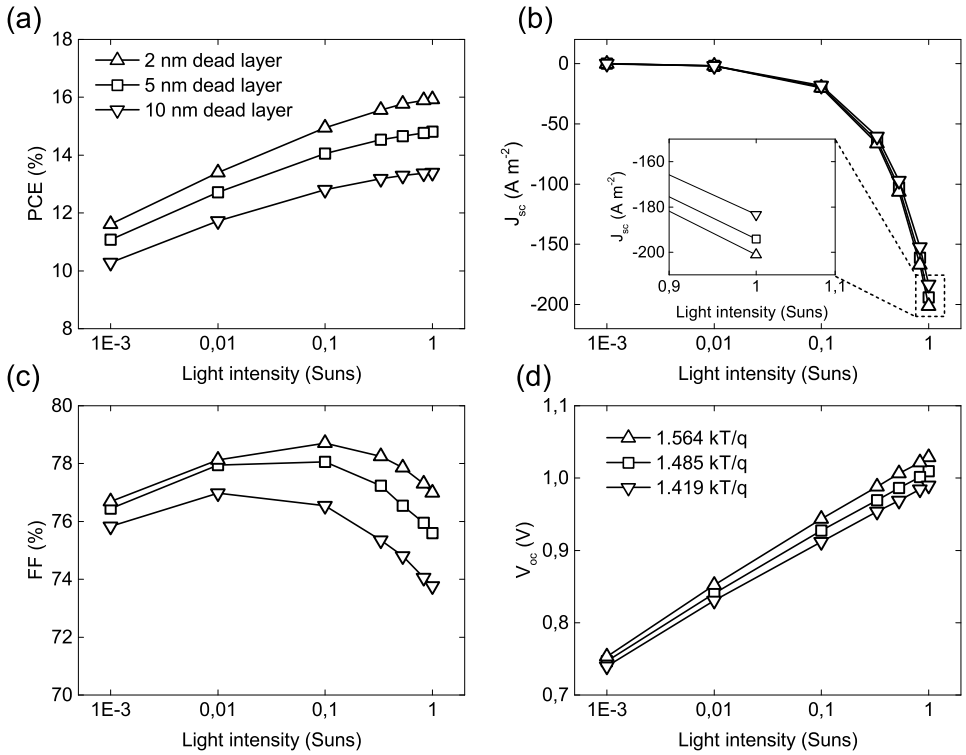

Figure 5.12: Photovoltaic parameters for different illuminations. a) PCE, b) J_{sc} with inset presented results at 1 sun, c) FF, and d) V_{oc}. Solar cell structure includes dead layer with 2 nm (triangle up symbol), 5 nm (square symbol) and 10 nm (triangle down symbol) thicknesses. Surface recombination velocities equal to 3.75×10^{3} and 3.75×10^{4} m s^{-1} for electrons and holes, respectively. 1 sun = 100 mW cm^{-2}.

current in each simulation is always about zero, because the open–circuit condition is used in the simulation. However, the amplitude of current within the simulated sample decreases proportionally with decreasing the light intensity. Figure 5.11(a) shows the PSC simulated at 1 sun illumination. It has been already noticed that the current distribution is reversed at the interface of the dead layer [Figures 5.8(c)]. However, the current distribution gets back to the normal distribution at the HTL interface for lower light intensity, see Figure 5.11(b-c). The explanation of this effect is related to a high asymmetric recombination in the dead layer. If light intensity increases, the total charge carrier concentration has a higher value. Therefore, the dominant recombination should be proportionally higher in the parasitic layer. As the surface recombination is asymmetric, it leads to inversion of a total distribution of photocurrent. However, at very low light intensities, where almost dark conditions are observed, the charge carrier density is much lower. Thus, the surface recombination is not strongly influencing the shape of photocurrent distribution. As a consequence, it starts to resemble the sample without a dead layer, see Figure 5.11(d) and Figure 5.8(II-c).

Further, the influence of dead layer thickness on illumination intensities is analyzed. Fig-

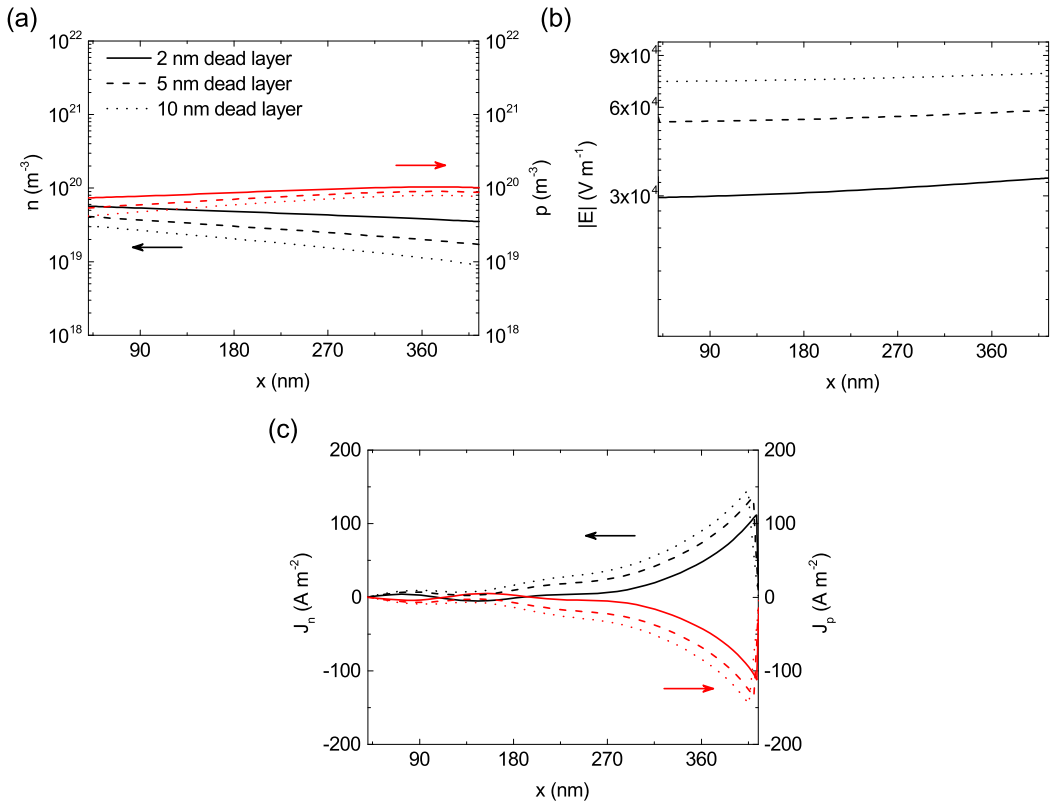

Figure 5.13: Spatial simulation results for an open–circuit voltage (V_{oc}) at 1 sun illumination only for the perovskite layer. a) Electron (black line) and hole (red line) density distributions, b) absolute electric field distribution, and c) electron (black line) and hole (red line) photocurrents. The simulation distance is in respect to cathode (Au) electrode. The parameters used are the same as in Figure 5.11.

ure 5.12 shows photovoltaic parameters for the PSCs with 2 nm, 5 nm (as a reference) and 10 nm dead layer with a constant surface recombination velocity. The Figure 5.12(a) demonstrates that the PCE is decreasing with increasing the thickness of the recombination layer. This trend is especially visible at high illumination intensities. The efficiency decreases mostly due to the loss of short–circuit photocurrent, see Figure 5.12(b). This occurs due to the fact that no charge carriers are generated within the recombination layer and due to small losses in the generation profile from an illumination side. Figure 5.12(c) illustrates the resulted FF. It should be noticed that the thicker the parasitic layer is, the more visible is a monotonic rise of the FF above 0.1 suns. This effect originates from the higher domination of the surface recombination. Recently, it has been reported that the fill–factor monotonically decreases in the whole range of illumination when the surface recombination is the only recombination mechanism [164]. From V_{oc} analysis, it is clear that the ideality factor gets closer to 1 for a higher thickness of the recombination layer, as shown in Figure 5.12(d). The same trends were obtained for the different surface recombination velocities with a constant thickness of

the dead layer (results are not shown here). The reason is that the recombination rate depends both on the thickness and the surface recombination velocity. Therefore, the same rate could be acquired with different parameters. However, a thickness of the dead layer also influences the photocurrent in contrast to a surface recombination velocity, which finally confirms our choice of recombination mechanisms.

Figure 5.13 shows spatial dependencies for different dead layer thicknesses. For clarity, the distributions are only presented for the perovskite (absorber) layer. It is observed that, for the higher surface recombination rates, the smaller values of a total charge carriers density within the absorber were obtained, see Figure 5.13(a). The difference between electron and hole concentrations rises with increasing the thickness of dead layer. This leads to the fact that the electric field increases linearly, see Figure 5.13(b). However, these changes in the concentrations and the electric field impact the diffusion and drift currents. Therefore, the total photocurrent is also varying with different recombination layer thicknesses, see Figure 5.13(c). The average current approaches zero for the open–circuit conditions, however the amplitude increases with increasing a thickness of the dead layer.

Chapter 6

The studies on the effect of different source of bromide on perovskite $Cs_{0.18}FA_{0.82}Pb(I_{0.94}Br_{0.06})_3$ solar cells

The perovskite solar cells are evolving rapidly but still the problem lies in instability at high temperature and humidity which pose to be daunting in a view of upscaling and application. Therefore, the recent research has led to the conclusion that perovskite solar cells with a mixed dual A–cation (2C) consists of formamidinium and cesium ions in perovskite layer have much better stability and efficiency [18]. In the same kind of perovskite with sufficient cesium content, it has been reported that its charge carrier properties are not reduced when increasing the bromide concentration [193]. Therefore, the 2C perovskite seems to be a good candidate for application in tandem solar cells with possibility to tune the band–gap by changing bromide and cesium content [194]. However, this raises a question which salt should be used to introduce bromide ions.

Here, we investigate the three sources of bromide in the $Cs_{0.18}FA_{0.82}Pb(I_{0.94}Br_{0.06})_3$ perovskite absorption layer, meaning lead bromide ($PbBr_2$), formamidinium bromide (FABr) and cesium bromide (CsBr). Using the same ion and mass concentration in the precursor, we have been able to compare the same perovskite composition made from the three different bromide sources. We analyze the perovskite layers prepared in the p-i-n device structure.

The goal of the following chapter is to understand the effect of different source of bromide on operation of solar cell. The obtained experimental results of photovoltaic parameters are analyzed with a special attention on the crystallizationn process which impacts the recombiantion via trap states. The numerical simulations have been used to study the role of different recombination rates. This chapter is partially based on [D. Głowienka, F. D. Giacomo, M. Najafi, J. Szmytkowski, Y. Galagan *The Effect of Different Source of Bromide on Perovskite $Cs_{0.18}Fa_{0.82}Pb(I_{0.94}Br_{0.06})_3$ Solar Cells*, in preparation].

6.1 Synthesis of perovskites and device fabrication

The precursor for a perovskite $Cs_{0.18}FA_{0.82}Pb(I_{0.94}Br_{0.06})_3$ layer was prepared in the following manner. A commercial lead iodide (PbI_2) (99.99%, TCI), formamidinium iodide (FAI) (GreatCell Solar), cesium iodide (CsI) (99.999%, Sigma-Aldrich), lead bromide ($PbBr_2$) (TCI), formamidinium bromide (FABr) (GreatCell Solar), cesium bromide (CsBr) (99.9%), dimethylformamide (DMF) solvent (99.8%, Sigma-Aldrich) and 1-methyl-2-pyrrolidinone (NMP) solvent (99.5%, ACROS Organics) were used as received. For the batch to test bromide compounds with possible impurities, the commercial $PbBr_2$ (99.999%, Sigma-Aldrich), FABr (>98.0%, TCI) and CsBr (99.9%, Sigma-Aldrich) were used. The three perovskite materials were prepared, called $PbBr_2$, FABr and CsBr based on the single bromide source. Therefore, the $PbBr_2$ was obtained by mixing the powders of 1.2M PbI_2, 1.1M FAI, 0.24M CsI and 0.12M $PbBr_2$, while the FABr by adding 1.33M PbI_2, 0.85M FAI, 0.24M CsI and 0.24M FABr together. The CsBr was prepared with 1.33M PbI_2, 1.1M FAI and 0.24M CsBr. The powders were dissolved in DMF:NMP (9:1 volume ratio) solution by stirring overnight at a room temperature. For the batch with heating of the solution, the stirring temperatures were kept constant at 60°C, 80°C and 100°C during stirring overnight. Then, the solutions were cooled down to a room temperature before spin–coating of the precursor.

Patterned glass/ITO substrates were ultrasonically cleaned and UV–ozone treated. The solar cells were prepared inside the glove–box filled with nitrogen and with oxygen and moisture levels about 1 ppm. First, the HTL was prepared with poly(triaryl amine) (PTAA)(Sigma-Aldrich) solution in toluene with the concentration of 2 mg mL^{-1}. The PTAA solution was spin–coated at 5000 RPM for 35 s with the acceleration of 5000 RPM s^{-1} followed with annealing at 100°C for 10 min. Subsequently, the perovskite, PCBM and BCP layers were spin–coated with the same procedure described in Chapter 5. Afterwards, the cleaning of ITO contacts was accomplished in air with DMF:chlorobenzene solution in 1:6 volume ratio to remove all the layers. At last, the Au electrodes were thermally deposited with a shadow masks on top of the ETLs. The deposition was accomplished under the vacuum pressure of 1×10^{-6} mbar to acquire a thickness of 100 nm.

6.2 Methods of characterization

The film thickness, XRD, AFM, UV–vis and PL measurements were carried on the perovskite film with the same apparatus and methods as described in Chapter 5. The structure analysis was also performed with an energy–dispersive X–ray (EDX) spectroscopy and scanning electron microscopy (Jeol JSM-6010LA IntouchScope; referred as SEM). The solar cells were measured with J–V characteristics, MPPT and EQE techniques, more details can be found in Chapter 5. The solar simulator is under AM1.5 but also sun filters were used to acquire photovoltaic parameters in the function of light illumination. The dynamic light scattering (DLS) (Malvern Zetasizer μV) has been used to measure the hydrodynamic diameter of perovskite particles in solution. The measurements were done in plastic cuvettes at

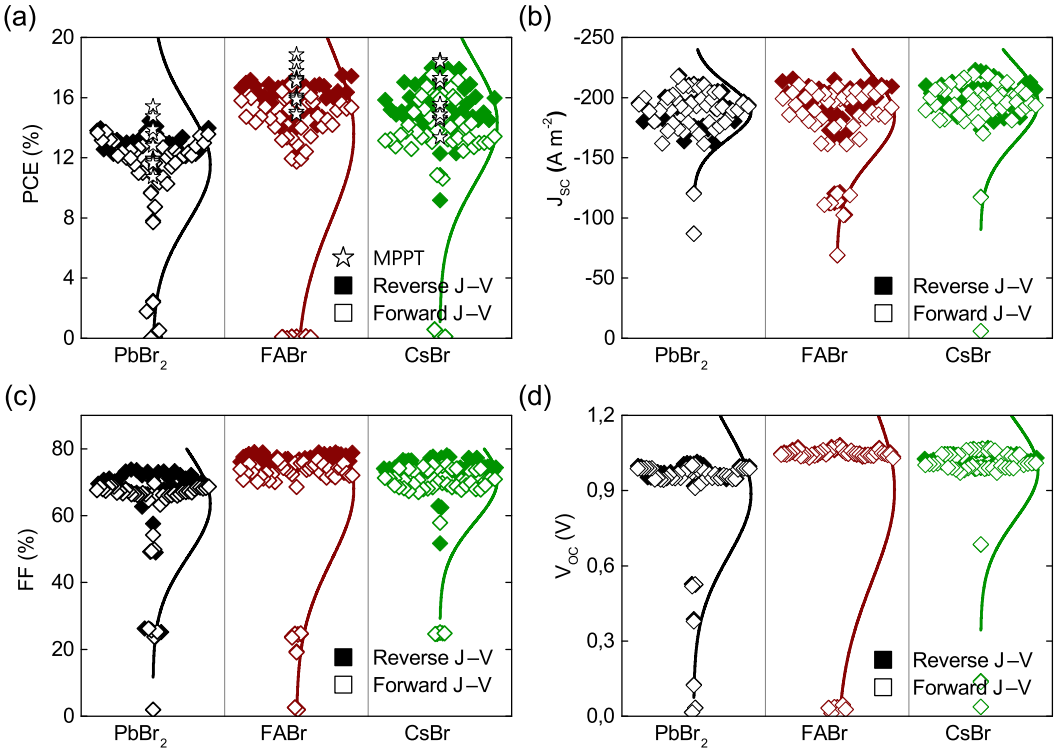

Figure 6.1: Photovoltaic parameters for PVSCs with the effect of different bromide source, a) PCE, b) J_{sc}, c) FF, and d) V_{oc}. The perovskite with $PbBr_2$ (black points), FABr (red points) and CsBr (green points) source of bromide.

20°C with the 832 nm laser wavelength. The scattering angle for the measurements was 90°. DLS measures the hydrodynamic diameter for non–spherical particles. The mean particle size was calculated by integrating the intensity distribution [195].

6.3 Experimental results

The three different bromide sourced perovskites $Cs_{0.18}FA_{0.82}Pb(I_{0.94}Br_{0.06})_3$ have been prepared in the same way but with different sources of bromide. Therefore, one perovskite is prepared with only $PbBr_2$ compound as the source of bromide atoms, second with FABr material, and third with CsBr. As there is assumed to be no other differences, for clarity the three perovskite materials are called in this chapter $PbBr_2$, FABr and CsBr, respectively.

The double–cation PSCs have been firstly measured with a sun simulator at AM1.5 condition. Figure 6.1 shows results for 144 devices measured in reverse and forward directions to observe the effect of hysteresis. The MPPs were obtained until steady–state conditions to reach for the best operating solar cells. Figure 6.1(a), shows that the efficiency of $PbBr_2$ is about 3% worse in comparison to FABr and CsBr. Interestingly, the hysteresis is different for each type of 2C perovskite solar cells, and it is the highest for FABr samples. The MPPT

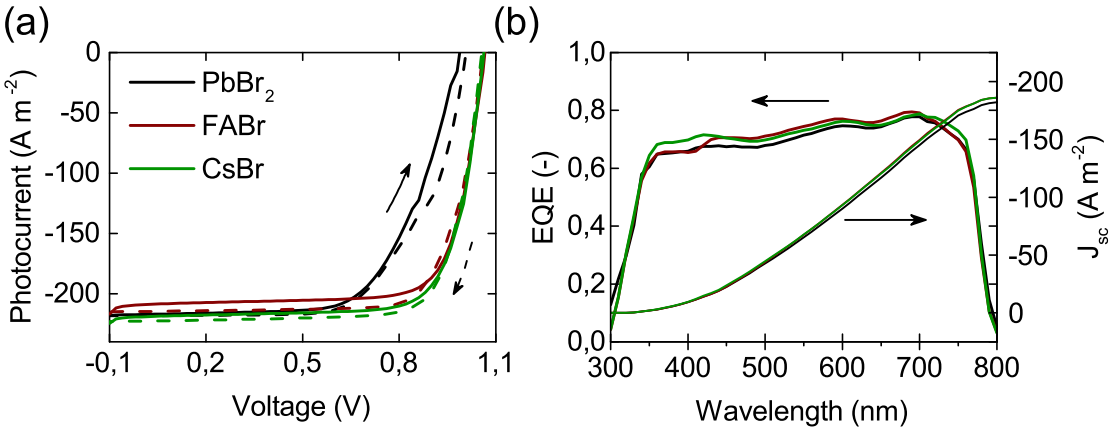

Figure 6.2: The experimental results for three PSCs. a) J–V characteristics for forward (solid line) and reverse (dashed line) scans, b) EQE and integrated photocurrent of the cells. Black, red and green lines represent perovskite solar cells with $PbBr_2$, FABr and CsBr bromide source, respectively.

has a higher value for FABr which suggests the long time stability of the samples. However, the photocurrent of the three types of perovskite solar cells are about to be the same, see Figure 6.1(b). Thus, the FF and V_{oc} should influence the observable differences in the efficiency. Figure 6.1(c) clearly illustrates the 6% and 5% average losses in FF for $PbBr_2$ cells in respect to FABr and CsBr ones, respectively. Also, the V_{oc} is lower for about 70 mV of $PbBr_2$ solar cells, see Figure 6.1. The visible effect suggests the influence of bromide source on electrical properties of the solar cells. It would be further discussed in this chapter.

To understand the PV effect more closely, the J–V characteristics are analyzed for the different bromide source perovskites measured for the hero solar cells, see Figure 6.2(a). The photovoltaic parameters are also written in Table 6.1. These cells exhibit a low hysteresis effect and a very similar short–circuit photocurrent. The J_{sc} is more related to optical than electrical properties of the material [196]. The V_{oc} of FABr and CsBr is approximately the same and 70 mV higher than for $PbBr_2$ solar cell. The same effect has been observed for FF of the $PbBr_2$ sample which is 12% lower than FABr and CsBr solar cells. This is in total accounts for approximately 4% increase of PCE by using different source of bromide.

The explanation could be related to possible impurities in the $PbBr_2$, FABr and CsBr com-

Table 6.1: Photovoltaic parameters for the $PbBr_2$, FABr and CsBr PSCs hero cells

	$PbBr_2$		FABr		CsBr	
	Forward	Reverse	Forward	Reverse	Forward	Reverse
J_{sc} [A m^{-2}]	-217.31	-218.26	-209.19	-214.78	-219.28	-222.82
V_{oc} [V]	0.99	1.01	1.07	1.06	1.06	1.06
FF [%]	63.24	62.70	75.62	75.05	75.15	76.32
PCE [%]	13.57	13.79	16.87	17.10	17.52	17.97

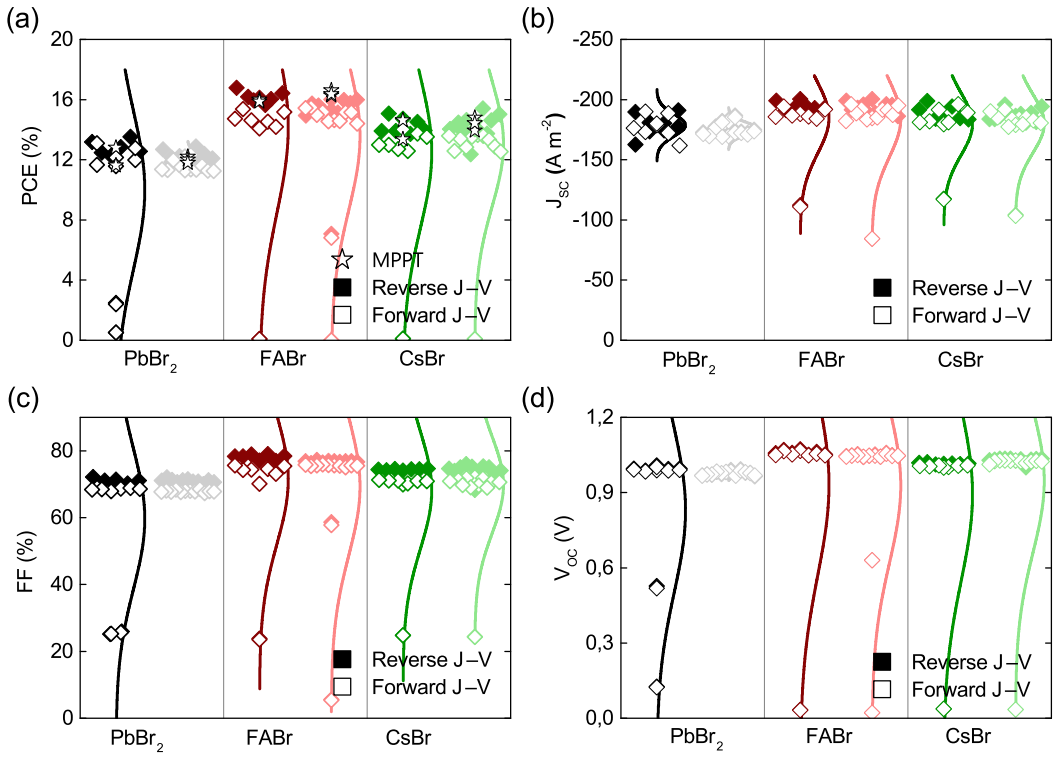

Figure 6.3: Photovoltaic parameters for PVSCs, a) PCE, b) J_{sc}, c) FF, and d) V_{oc}. Solar cells with the different bromide source and the alternative producer to exclude possible impurities effect. The perovskite with $PbBr_2$ (black points), FABr (red points) and CsBr (green points) source of bromide. The darker colors correspond to regular producer and the lighter in respect to new producer.

pounds which would influence the observed effect in solar cells. Therefore, the different producers of the same compounds have been tested. Figure 6.3 shows results for PCE, J_{sc}, FF and V_{oc}. It is observed that the tendencies are the same as previously, making the $PbBr_2$ worst in about 4% in efficiency comparing to FABr and approximately 2% lower PCE than CsBr. More importantly, there are no observed differences between the two producers when analyzing the efficiency and other photovoltaic parameters. This confirms that the observed effect is related to physical phenomena taking place in solar cell. Further discussion should illustrate this problem more closely.

The mass concentration of all 2C perovskites is the same for all perovskite layers, therefore the profilometer measurements gave the comparable thicknesses equal to 550±8 nm. The thicknesses of PTAA, PCBM and BCP layers are equal to 4.78±0.47 nm, 40.95±1.83 nm and 5.16±0.68 nm. Figure 6.4 shows the results of structural analysis. The single layer of perovskite has been analyzed on the glass substrate with XRD measurements, see Figure 6.4(a). The three perovskite layers do not show any differences in diffraction patterns suggesting that the perovskite crystals have the same crystallographic phase. The XRD results of the double–

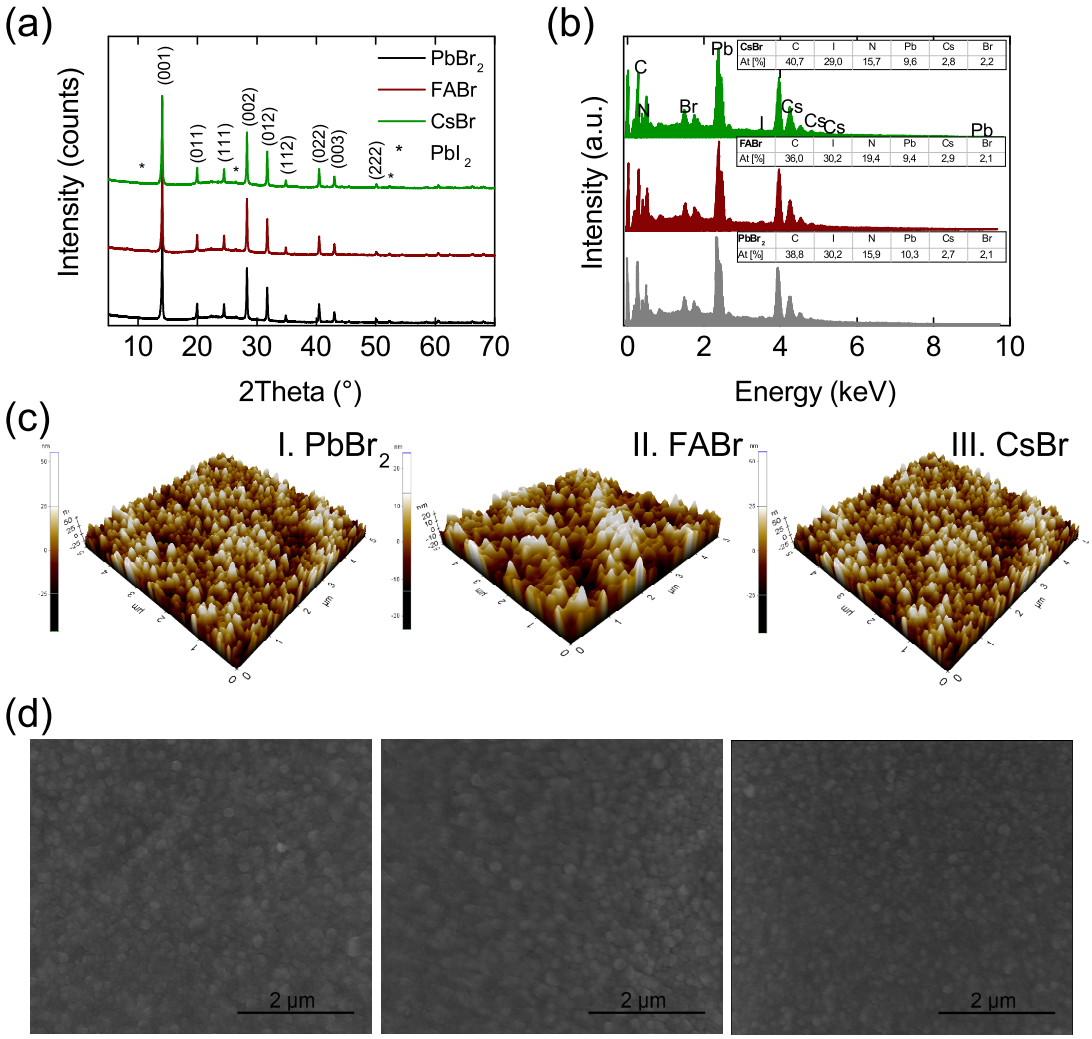

Figure 6.4: Experimental results for the perovskite layer on glass, a) XRD, b) EDX, c) AFM, and d) SEM measurements. The perovskite with $PbBr_2$ (black line), FABr (red line) and CsBr (green line) source of bromide.

cation (2C) perovskite exhibit the regular pattern for perovskite material with the highest intensity peaks at 14.1° and 28.3° in (001) and (002) directions [197]. The phase impurities are observed at 11.5°, 26.5° and 52.4° which are related to PbI_2, and also to non–perovskite γ phase [198]. In general, an incorporation of the FA in perovskite into A–cation leads to improvements of its electrical properties. However, the non–perovskite hexagonal phase is thermodynamically more favorable than a cubic phase in the room temperature [199]. It has been shown that an addition of Cs atoms into the perovskite stabilizes the perovskite phase [18]. Therefore, we observe perovskite layers with negligible secondary phase. The atomic concentrations for all three $Cs_{0.18}FA_{0.82}Pb(I_{0.94}Br_{0.06})_3$ perovskites are prepared with 18% of

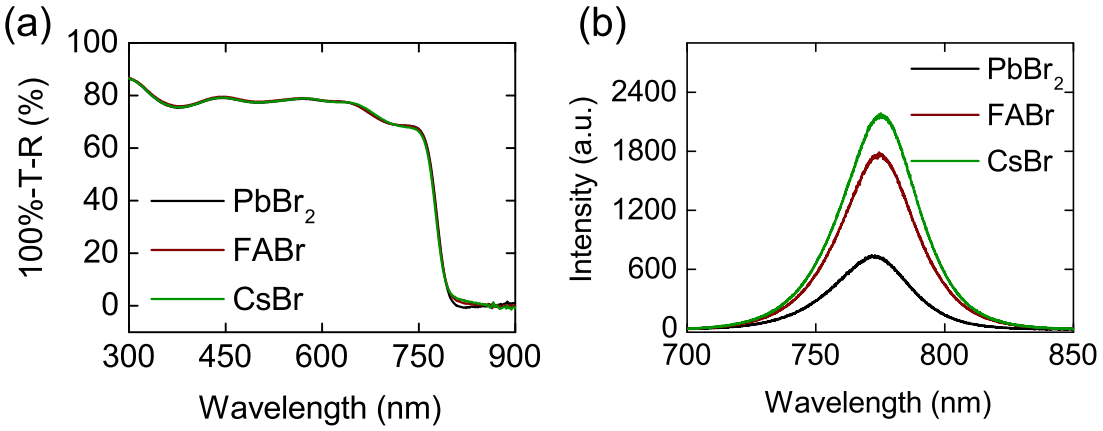

Figure 6.5: Experimental results for the perovskite layer on glass, a) UV-vis, b) PL measurements. The perovskite with $PbBr_2$ (black line), FABr (red line) and CsBr (green line) source of bromide.

Cs, 82% of FA in A–cation, 94% of I and 6% of Br in the anion site. Figure 6.4(b) shows the EDX results giving the atoms concentration present in the 2C perovskite. As it is expected, all three perovskites have about the same atoms concentration. However, the samples exhibit slightly lower Cs concentration (2.1% instead of 3.6%) which suggests that not all cesium has been built in the perovskite structure. There is also found an excess of FA but the bromide and iodide atoms are totally built into the structure. Figure 6.4(c) illustrates AFM pictures of surfaces which exhibit negligible differences with roughness equal to 11.2 nm, 10.4 nm and 12.8 nm, and also the average grain size equal to 125.9 nm, 113.6 nm and 125.3 nm for $PbBr_2$, FABr and CsBr perovskites, respectively. Figure 6.4(d) presents the SEM images which gives grain size equal to 156.9 nm for $PbBr_2$, 120.8 nm in FABr and 116.8 nm for CsBr perovskite layers. Therefore, as it has been assumed, the structures of all three 2C perovskites do not show much differences.

Figure 6.5(a) illustrates optical analyzes with UV–vis measurements of single perovskite layers on the glass. It has been already shown that J_{sc} does not change much in the solar cell with different bromide source. Here, we can see that the absorption properties are very similar to all three types of perovskite materials. Also, the results calculated from the tauc–plot give an energy band–gap values equal to 1.581 eV, 1.583 eV and 1.584 eV for $PbBr_2$, FABr and CsBr, respectively. Therefore, further in the chapter the approximated value of 1.58 eV for the band–gap is used for simulation purposes. Figure 6.5(b) shows the PL plots with the highest peak intensity for CsBr, FABr and $PbBr_2$, respectively. Photoluminescence is a process where semiconductor absorbs a photon of energy higher than a band–gap which excites electron from the valence band to the conduction band. Subsequently, as a result of the recombination, it radiates a photon when the electron returns to a valence band. Meaning, the mechanism is partially related to a bimolecular recombination rate, see Chapter 2. Thus, the emitted photon possess an energy equal to the band–gap and the maximum of the peak in function of energy gives values equal to 1.605 eV, 1.601 eV and 1.599 eV for $PbBr_2$, FABr and

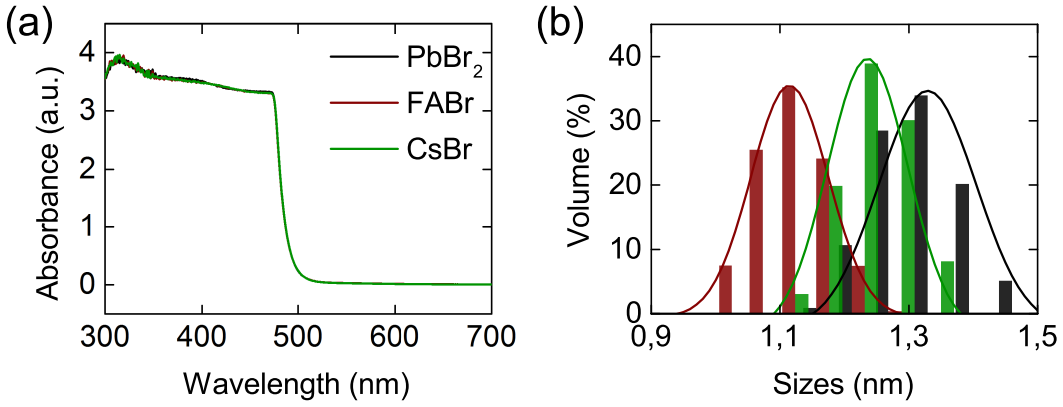

Figure 6.6: The experimental results for three perovskite solutions. a) UV–vis, b) DLS measurements. Black, red and green colors represent perovskite solutions with $PbBr_2$, FABr and CsBr bromide source, respectively.

CsBr, respectively. As from the UV–vis analysis, the values are close to each other. Therefore, the optical properties of both materials are very similar with no observed differences measured so far. It has been also shown that a higher PL intensity in the perovskite material is related to a higher lifetime of charge carriers, and therefore lower the recombination rate [200]. This may suggest that $PbBr_2$ has the highest recombination rate comparing to CsBr and FABr.

It is obvious that by changing the three bromide source materials the electrical properties of 2C perovskite solar cells are influenced. Before deeper analysis of the effect, its origin should be first investigated. Therefore, as the analysis of the perovskite layer does not reveal the answer, the next step is to focus on the perovskite precursor. First, the regular precursors are analyzed with UV–vis and DLS measurement methods, see Figure 6.6. It is already found that the perovskite precursor solution are not fully dissolved colloidal dispersions [201]. It has been shown that the colloids are made of organic, inorganic and coordination compounds (complex compounds created from the formation of both organic and inorganic materials). The size and properties of the colloids determine the quality of the produced perovskite layer. The red–shift of the UV–vis absorption spectrum would suggest an increase of the colloidal size. However, the PbBr2, FABr and CsBr perovskite precursor spectra are not shifted, see Figure 6.6(a). Also, the DLS results show only a slight difference in the size of the observed particles, as presented in Figure 6.6(b). Therefore, the conclusion is that the size of colloids in perovskite precursors are approximately the same. The particle size would change if concentration of the precursor would be different.

Further, we analyze the compounds dissolution in the precursor. It is well known that a heating of the perovskite solution influences the photovoltaic performance of PSC [202–205]. It has been also shown that a precursor heating may lead to the reduction of defect–mediated recombination [204]. Therefore, we have heated $PbBr_2$, FABr and CsBr perovskite solutions up to 60°C, 80°C and 100°C before spin–coating of the solar cells. Basically, the

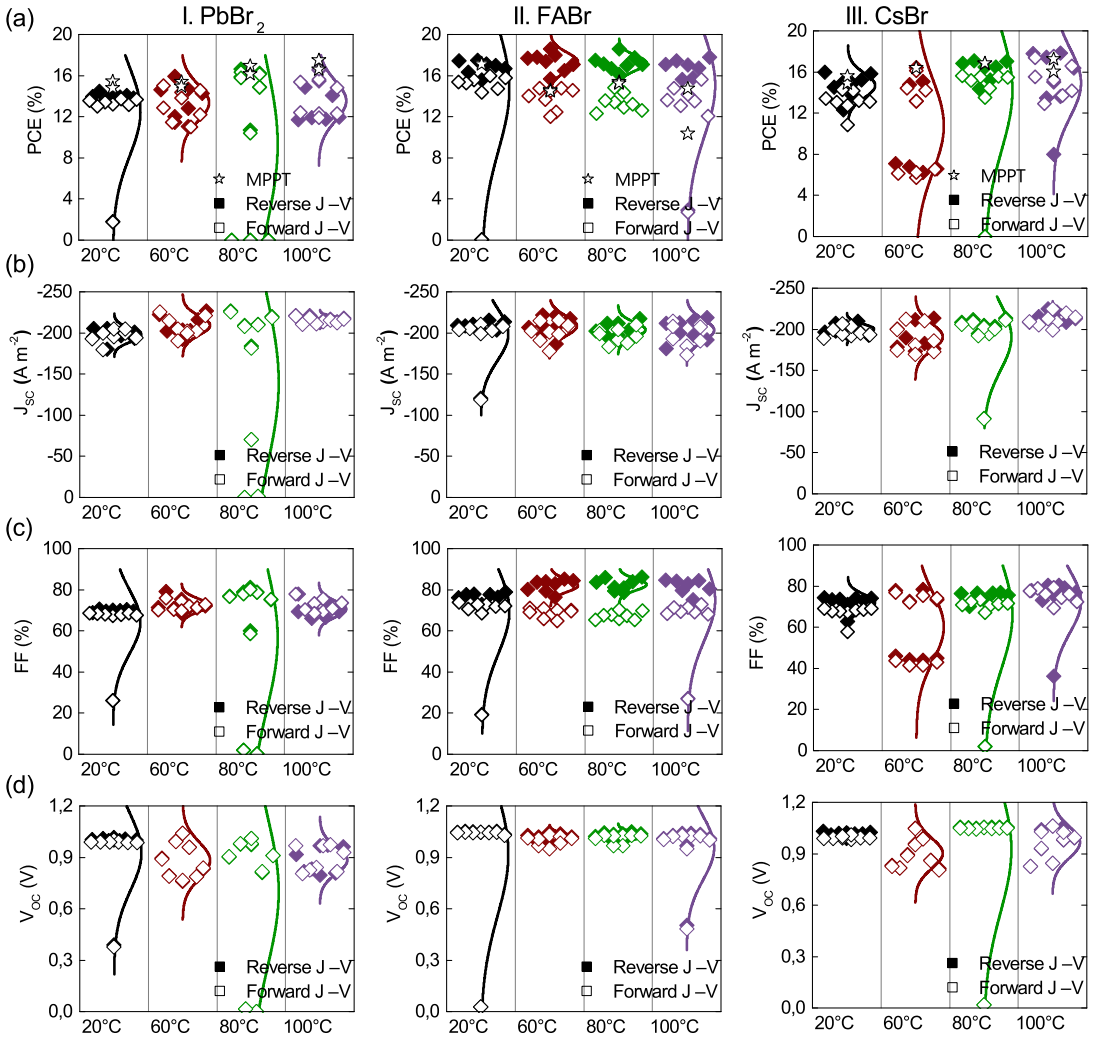

Figure 6.7: Photovoltaic parameters for PVSCs, a) PCE, b) J_{sc}, c) FF, and d) V_{oc}. Solar cells with heating of the solution overnight in 20°C (black points), 60°C (red points), 80°C (green points) and 100°C (violet points). The perovskite with $PbBr_2$ (section I), FABr (section II) and CsBr (section III) source of bromide.

heating was done overnight at a given temperature but before spin–coating of the precursor, the solution was cooled down to a room temperature. Figure 6.7(a) shows the PV results for the aforementioned heating procedure for $PbBr_2$ perovskite solar cell. It is observed that the heating to 60°C increases the efficiency by about 1% by mostly increasing the FF. Further rise to 80°C in temperature leads to improve of FF to about 80% but with a negligible decrease of V_{oc}. It seems that for 80°C it has reached the maximum efficiency and starts to decrease at higher temperature which effect has been also observed in the literature [204]. Figure 6.7(b–c) shows a similar behavior for FABr and CsBr. Surprisingly, the FABr samples seem to pos-

sess a higher hysteresis effect when rising the temperature of the precursor. However, most importantly, the PCE of all three types of perovskite have reached the same efficiency after heating of the precursors to 80°C. The observed effect leads to conclusion that the lower efficiency of $PbBr_2$ solar cells is related with properties of the colloids which are creating complex compounds from different particles in the precursor. It is suggested that different source of bromide influences the type of complex compounds that are created. The colloids are nucleation seeds, thus their properties are of great importance in the crystallization process. For a higher temperature the solubility of all compounds is higher which leads to more favorable situation and colloids have the same properties for all materials. The crystallization of perovskite layer has a great impact on their efficiency [206–208]. Here, it is suggested that using $PbBr_2$ for preparation of 2C perovskite solar cell without heating of the precursor leads to an increase of defect states in the absorber during crystallization process. This is related to the rising of the trap–assisted recombination rate which lowers the operation efficiency of the devices. To confirm it, the last part of this chapter is focused on the simulations which would help in understanding of the role of the recombination process.

6.4 The model for simulations with parameters for the investigated devices

In this part of the chapter, the trap–assisted recombination is investigated for the $PbBr_2$, FABr and CsBr perovskite solar cells. It has been experimentally observed that the use of different source of bromide leads to change of electrical properties due to a crystallization process of the perovskite layer. Thus, the hypothesis should be proved by modeling the cells to find the recombination rates. Simulating J–V characteristics may lead to an overestimation of the parameters due to a number of possible fitting parameters. Therefore, we use the experimental results obtained for different illumination rates which narrows the fitting procedure to much less possibilities.

The drift–diffusion used in this chapter is in general the same as presented in the Chapter 5 but with the difference in the recombination models. The continuous equations are given for electrons

$$\frac{\partial n}{\partial t} = G - R_m - R_b - R_t + \frac{1}{q}\frac{\partial J_n}{\partial x}, \tag{6.1}$$

and holes

$$\frac{\partial p}{\partial t} = G - R_m - R_b - R_t - \frac{1}{q}\frac{\partial J_p}{\partial x}, \tag{6.2}$$

where G is a generation rate described with the transfer–matrix model (see Section 2.1.5), R_m represents a monomolecular recombination rate given this time with the DOS of trapped states (Section 2.1.7.1), R_b is a Langevin recombination rate (Equation 2.36) and R_t represents a trimolecular recombination mechanism (Equation 2.38). The interfaces were not

Table 6.2: Parameters used in simulation of the PSCs. For better readability, parameters for holes and electrons are written in the brackets and without brackets, respectively. The parameters in (a) marked with $\times$ symbol are given in (b).

(a) Parameters used in the simulation for all used layers of the solar cells.

	unit	ETL	perovskite	HTL
L	nm	40	550	5
N		20	100	20
ε_r		3.75	63	2.67
$\mu_{n(p)}$	$cm^2\ V^{-1}\ s^{-1}$	2×10^{-3}	$\times$	$6 \times (10^{-3})$
$C_{nc(\nu)}$	$m^3\ s^{-1}$	10^{-18}	$\times$	(5.88×10^{-18})
$C_{pc(\nu)}$	$m^3\ s^{-1}$	10^{-4}	$\times$	(5.88×10^{-18})
$N_{tn(p)}$	m^{-3}	10^{22}	$\times$	(10^{20})
$\Gamma_{n(p)}$	$10^{-40}\ m^6\ s^{-1}$	4	1.55	(4)
ξ		10^{-4}	10^{-2}	10^{-4}
$E_{c(\nu)}$	eV	-4.0	-3.9 (-5.48)	(-5.35)
$E_{tn(p)}$	eV	-5.0	-4.69 (-4.69)	(-4.33)
$N_{D(A)}$	m^{-3}	10^{20}	0 (0)	(10^{20})
$N_{c(\nu)}$	m^{-3}	2.5×10^{25}	8×10^{24}	(2.5×10^{25})

(b) Parameters for the simulation of the different bromide sourced perovskite layers.

	unit	$PbBr_2$	FABr	CsBr
$\mu_{n(p)}$	$cm^2\ V^{-1}\ s^{-1}$	6(1)	1(0.5)	6(1)
$C_{nc(\nu)}$	$10^{-14}\ m^3\ s^{-1}$	10(5)	0.85(8.5)	6(25)
$C_{pc(\nu)}$	$10^{-14}\ m^3\ s^{-1}$	0.5(1.7)	8.5(0.85)	2(2)
$N_{tn(p)}$	$10^{20}\ m^{-3}$	10(20)	2(2)	4(4)

modified during the experiment by changing the bromide source in the perovskite precursor. Therefore, it is assumed to be no surface recombination in the PSCs to simplify the model. $J_{n(p)}$ are electron and hole current densities given by Equations 2.8 and 2.9, respectively. The Poisson equation for calculating the electric potential includes only electric charge carriers

$$\frac{\partial^2 \varphi}{\partial x^2} = -\frac{q}{\varepsilon_0 \varepsilon_r} \left(p - n + N_D - N_A\right), \tag{6.3}$$

where the parameters N_D and N_A are donor and acceptor concentration densities in ETL and HTL layers, respectively.

Table 6.2(a) shows the parameters presented for each layer in the PSCs stack. The layer thickness (L) of ETL (PCBM material), perovskites and HTL (PTAA material) are measured experimentally with a profilometer. In general, all the parameters for PCBM are the same as in Chapter 5. The same are also the dielectric constant (ε_r), trimolecular recombination constants ($\Gamma_{n(p)}$), Langevin recombination reduction factor (ξ), doping densities ($N_{D(A)}$)

and effective density of states ($N_{c(v)}$) for perovskite layers, see Table 5.2 (Chapter 5). The given thicknesses are discretized with a specified number of points (N) using the Chebyshev polynomial, as described in Section 2.4.1. The ε_r of PTAA is measured experimentally using the optical κ and η constants at infrared range. The charge carrier mobility ($\mu_{n(p)}$) for HTL is adopted from the literature [209]. The traps densities ($N_{tn(p)}$ and trapping rates from conduction ($C_{nc(v)}$) and valence ($C_{pc(v)}$) bands are symmetrical and located (E_t) in the middle of the band–gap for PTAA layer [210, 211]. There have been not found any literature data for ξ, $\Gamma_{n(p)}$, $N_{D(A)}$ and $N_{c(v)}$ for HTL, therefore there are assumed to be the same as ETL. The energy distribution for the Gaussian function in both layers is assumed to be very narrow and equal to a 0.01 eV to simulate single energy level. However, the trap DOS for perovskite layers has been fixed to 0.1 eV width. The energy level of PTAA is close to the literature [212]. The perovskite energy bands are shifted to adjust to the band–gap acquired from the UV–vis experimental results, see Figure 6.5(a).

Table 6.2(b) shows the parameters that are varying for different bromide source in PSCs. The mobilities are assymetrical and within the range of literature values [213]. It has been found that the mobility in FABr perovskite sample is lower than in $PbBr_2$ and CsBr. However, this might be related to only this batch, therefore no further conclusion is made for it. The trap densities and capture rates are obtained as a result of fitting. These values would be further discussed in the text. The injection barriers are the Schottky barriers at the cathode/ETL and HTL/anode with values equal to 0.1 eV and 0.17 eV, respectively. The ITO material represents the anode contact, whereas BCP/Au acts as in the cathode contact, the same as in Chapter 5. The simulation temperature is the same as the experiment and equal to 295 K. The built–in voltage equals to 1.01 V which is close to the literature values [214].

6.5 Numerical results

The J–V characteristics have been recorded under illumination between 1 sun (AM1.5) to 0.001 suns (0.1% of AM1.5). There have been measured 24 devices with the following method but only the representative are presented here, see Figure 6.8. The simulated PSCs have a conversion efficiency equal to 13.65%, 16.13% and 14.51% for $PbBr_2$, FABr and CsBr, respectively. Figure 6.8 illustrates that the PCE decreases almost linearly with illumination. Figure 6.8(b–inset) also shows that the linear tendency of PCE is mostly due to the same relation of photocurrent. Linear relation of J_{sc} in a function of light illumination suggests the monomolecular recombination as the dominant mechanism in SC condition [215]. The behavior of solar cell at MPP is best described with FF versus illumination intensity which is still the least understood photovoltaic parameter. Figure 6.8(c), shows the general shape of the FF which implies a competition of two dominant recombination mechanisms. Below 1 sun, the FF increases slightly for all three PSCs which may suggest it is intrinsically related to the device. However, it monotonically decreases below 0.1 suns which should be associated with the trap–assisted recombination [160]. Figure 6.8(d) illustrates V_{oc} results plotted in a function of sun illumination. It shows logarithmic dependence on the light illumina-

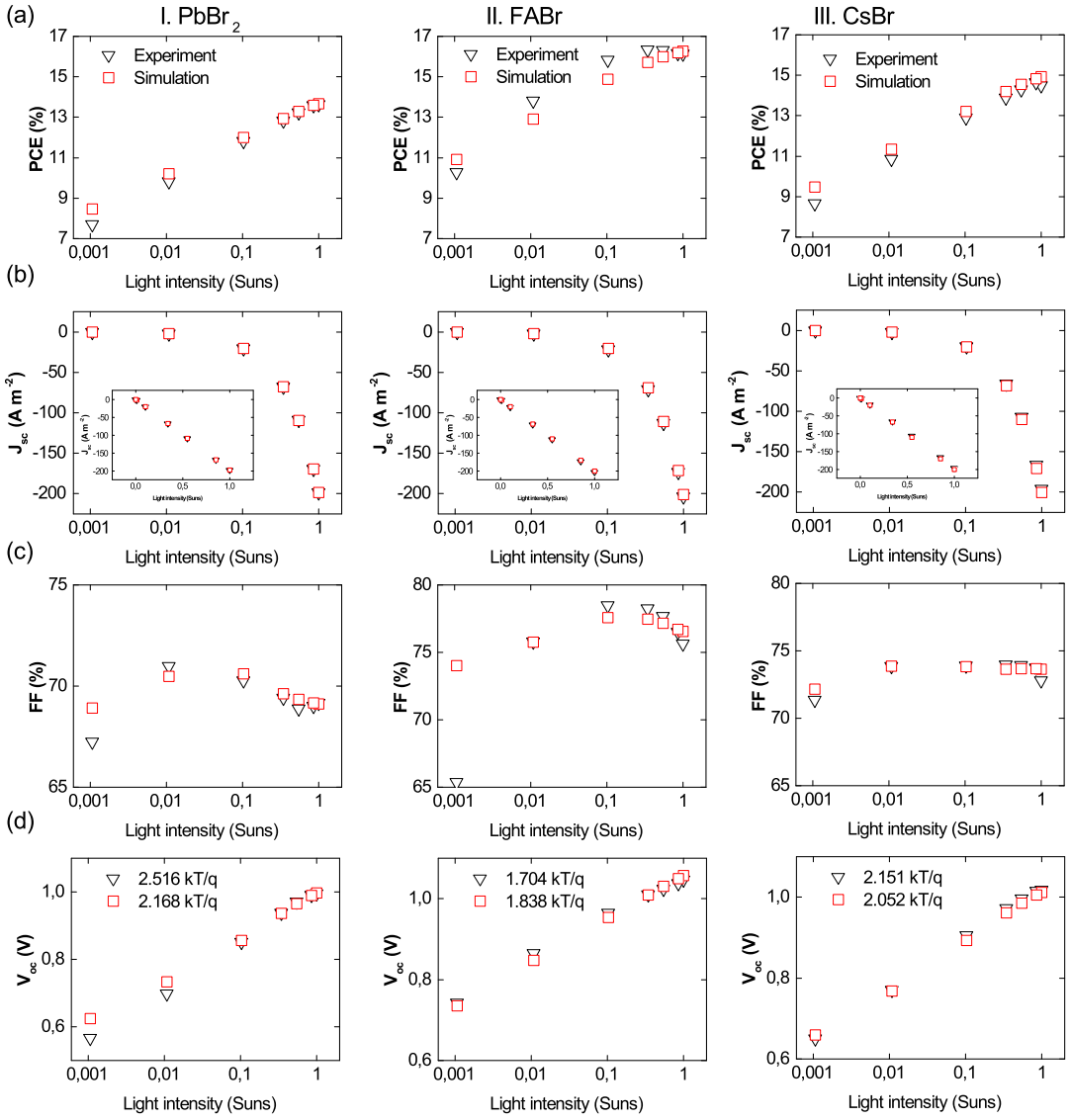

Figure 6.8: Photovoltaic experimental (black triangle symbol) and simulation (red square symbol) results for different illuminations. a) PCE, b) J_{sc} with the inset presented the same result using linear scale of the light intensity, c) FF, and d) V_{oc}. Solar cell structure with $PbBr_2$ (section I), FABr (section II) and CsBr (section III) bromide source. The parameters used for simulation are shown in Table 6.1. 1 sun = 100 mW cm^{-2}.

tion which can be used to calculate a diode ideality factor (n_{id}) using the analytical model for V_{oc} [216]. Based on this factor, the dominant recombination mechanism can be found at an open–circuit condition. For PSC with $PbBr_2$, n_{id} is equal to 2.516 kT/q. Such a high value could be only explained with a multiple–trapping or the trap distributions [192]. The ideality factor seems to be lower for FABr and CsBr solar cells but still around 2 which suggests

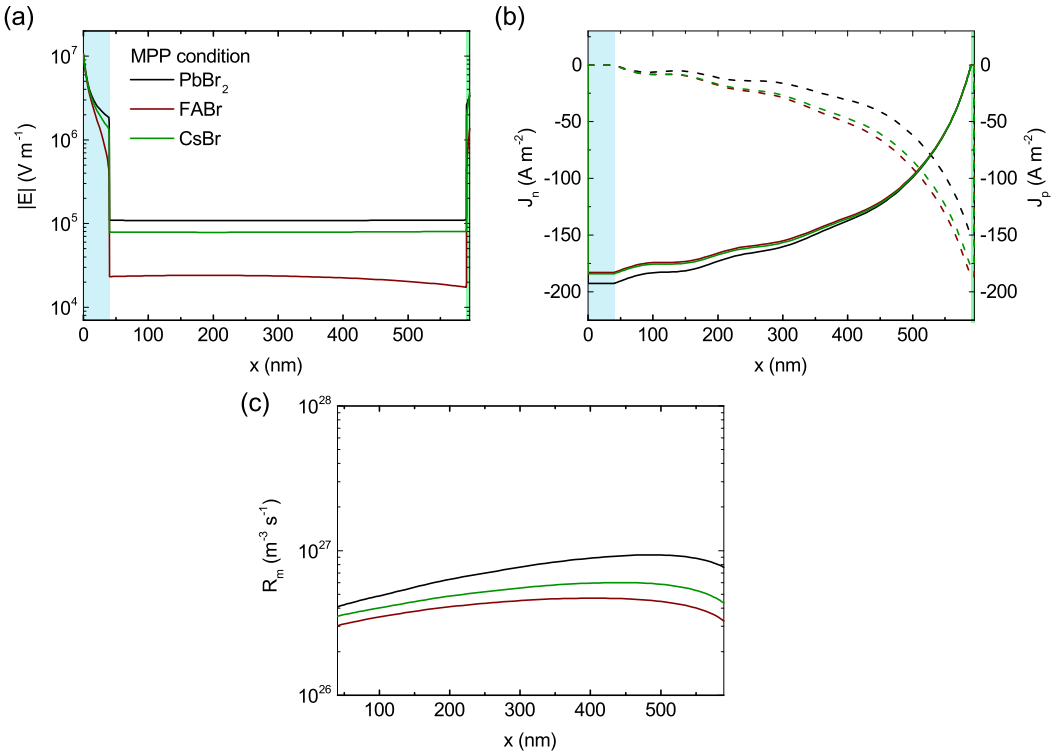

Figure 6.9: Spatial simulation results for a maximum power point (MPP) at 1 sun illumination. a) Absolute electric field distribution, b) electron (solid line) and hole (dash line) photocurrents, and c) monomolecular recombination rates. The simulation distance in (c) is in respect to cathode (Au) electrode. Black, red and green lines represent perovskite solar cells with $PbBr_2$, FABr and CsBr bromide source, respectively. The parameters used for simulation are shown in Table 6.1.

trap–assisted recombination as the dominant recombination mechanism.

Figure 6.8 also illustrates the simulation results for all three PSCs. The very good agreement between experimental and simulation results has been shown for the parameters from Table 6.2. For all samples, we can observe a small discrepancy at 0.001 suns illumination. This effect could be explained with a leakage current which has the higheest impact at low intensities [191]. From the simulations for $PbBr_2$, it is concluded that the rate of monomolecular (8.16×10^{27} m^{-3} s^{-1}) recombination is about three orders of magnitude higher than a

Table 6.3: Monomolecular recombination rates (m^{-3} s^{-1}) for the perovskite solar cells.

	$PbBr_2$	FABr	CsBr
SC	8.16×10^{27}	2.71×10^{27}	4.12×10^{27}
MPP	7.06×10^{28}	3.93×10^{28}	4.88×10^{28}
OC	4.38×10^{29}	3.24×10^{29}	3.89×10^{29}

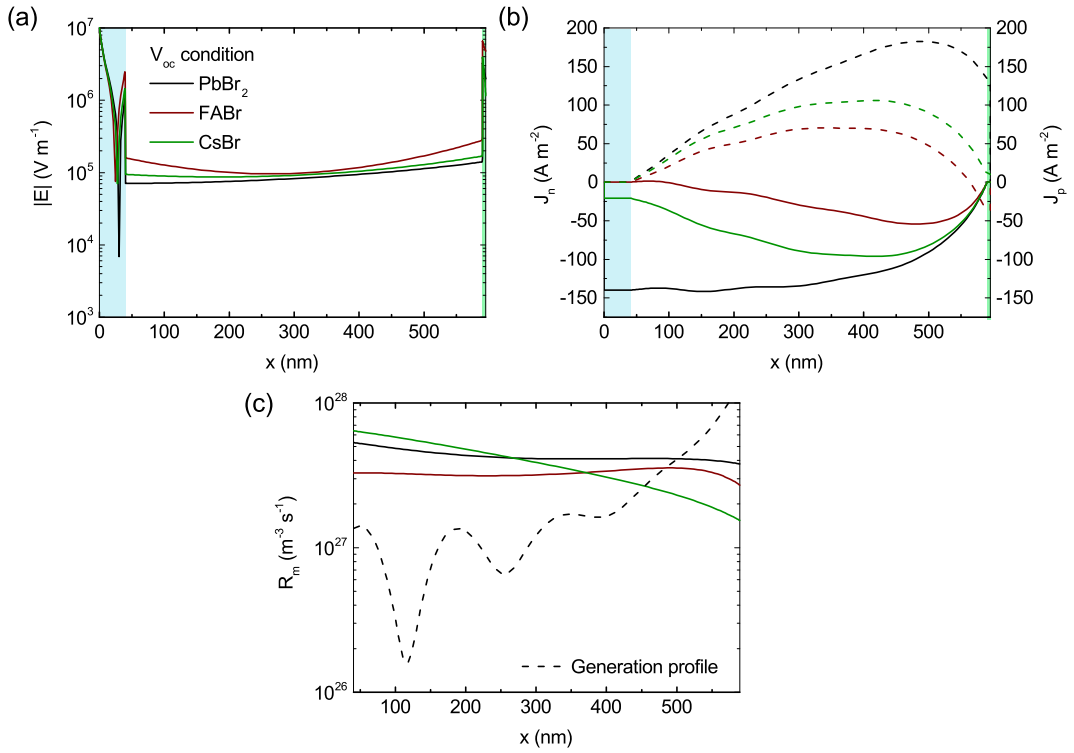

Figure 6.10: Spatial simulation results for a open–circuit voltage (V_{oc}) at 1 sun illumination. a) Absolute electric field distribution, b) electron (solid line) and hole (dash line) photocurrents, and c) monomolecular recombination rates. The simulation distance in (c) is in respect to cathode (Au) electrode. Black, red and green lines represent perovskite solar cells with $PbBr_2$, FABr and CsBr bromide source, respectively. The parameters used for simulation are shown in Table 6.1.

bimolecular rate (1.49×10^{24} m^{-3} s^{-1}) and about ten orders than a trimolecular recombination rate (9.34×10^{17} m^{-3} s^{-1}) at SC. For OC, there are obtained 4.38×10^{29} m^{-3} s^{-1}, 1.42×10^{28} m^{-3} s^{-1} and 1.08×10^{24} m^{-3} s^{-1} for monomolecular, bimolecular and trimolecular recombination rates, respectively. Therefore, as the monomolecular recombination was found to be dominant in all characteristics points, we further focus only on this recombination mechanism.

It has been already shown experimentally that the effect of using different bromide sources is mostly visible for FF and V_{oc} which has been attributed to the trap–assisted recombination rate. Figure 6.9 shows simulation results at MPP with 1 sun illumination. It is clearly visible that an electric field within the absorber layer is the highest for $PbBr_2$, see Figure 6.9(a). This is a consequence of the highest traps density which are due to the concentration of defect states created in the perovskite during the crystallization process. Therefore, the electric field impact the total photocurrent by changing the drift of charge carriers, as shown in Figure 6.9(b). This effect is mostly visible in the hole partial currents which are the lowest for $PbBr_2$. It could be explained with the behavior of the total monomolecular recombination

rate in function of space in the device. Figure 6.9(c) shows that this rate is the highest at HTL side when comparing $PbBr_2$ to two other solar cells. The total recombination rate, when integrating over space at MPP, is about two times higher for $PbBr_2$ than FABr or CsBr, as shown in Table 6.3.

At OC, the electric field distributions are negative as we are close to built–in voltage, see Figure 6.10(a). Therefore, the absolute electric fields are misleadingly showing the highest values for FABr perovskite solar cell. However, the values are not much different so these are negligible variations. Thus, the observable differences in photocurrent should be related to the diffusion instead of drift currents, see Figure 6.10(b). It is expected to have a zero current flowing out of the cell at OC condition which is self consisted from simulation. However, the internal distribution may be still interrupted due to a high net generation and recombination rates of charge carriers, as shown in Figure 6.10(c). Therefore, as the $PbBr_2$ and CsBr have both a higher monomolecular recombination rate than a total generation rate (3.39×10^{29} m^{-3} s^{-1}) it may influence the internal total currents, see Table 6.3.

The $PbBr_2$, FABr and CsBr source of bromides in perovskite solar cells are influencing the properties of colloidal dispersion which could be overwhelmed by increasing of the precursor temperature before spin–coating. It directly impacts the crystallization process and as a result changes the density of defect states in the perovskite absorber. This effect is enough significant to influence the efficiency of PSCs by about 3%. The simulations has proved that the observed phenomena influences the monomolecular recombination rate which impacts the operation of the solar cell. The following studies show how sensitive the crystallization process of perovskite might be and that the control of it is the key for achieving high efficiency solar cells.

Summary and conclusions

The carbon dioxide concentrations in the atmosphere are rapidly increasing, and the emissions are caused mostly due to the burning of fossil fuels. Therefore, the energy sector needs to start using renewable energy resources. Harvesting energy directly from the sun is potentially a very attractive way but it needs expensive devices to generate electricity or heat. The organic and perovskite solar cells are very prospective, however more studies are needed before commercialization to overcome the problems with efficiency and long time stability. Therefore, the aim of this thesis was to analyze in details the processes related to an increasing (or decreasing) of efficiency of the organic and perovskite solar cells with the use of experimental and numerical techniques.

The first studies were concerning the mechanism of excitons annihilation on charge carriers. The calculations based on the one–dimensional transient drift–diffusion model have been done. We have studied an influence of the excitons interaction with charge carriers on photovoltaic parameters (the short–circuit current, the open–circuit voltage, the fill factor and the power conversion efficiency). A visible decreasing of the organic photocells efficiency with the annihilation process has been observed for $\gamma_{cs} > 10^{-15}$ m^3 s^{-1}, a similar value to an experimental result for P3HT. The effect of exciton annihilation has been observed not only in spatial and photovoltaic results but also in the transient simulations. This fact confirms that the exciton annihilation mechanism should play a significant role in structures applied in organic solar cells. Also, the simulations for a nonuniform generation profile (calculated based on the transfer–matrix model) has been shown for the same organic solar cell structure. For this reason, the numerical results have illustrated that the exciton distribution follows the generation profile but it does not give much difference in the final operation of organic solar cell. Therefore, the conclusion is that the use of an uniform generation is a good approximation in modeling and gives the same explanation of the role of exciton annihilation in the organic device. Also, the total structure of organic solar cell has been simulated, including all layers and interfaces. It has been shown that the introduction of interfaces leads to drastic changes of current–voltage characteristics mostly at open–circuit conditions. Also, we have proved that high exciton annihilation, and therefore the high concentration of excitons may cause a characteristic S–shape in J–V curve when modeling with interface effects. More detailed simulations have shown that simulation of the whole device gives much different charge carrier distributions. Therefore, the use of interfaces is critical in a deeper analysis of organic solar

cells.

Later, we have focused on an impact of excitons in the organometal trihalide perovskite $CH_3NH_3PbI_3$ solar cell for tetragonal and orthorhombic phases. The studies have been carried out based on the validated space and time numerical model. A very good agreement has been found between theoretical and experimental J–V characteristics for several thicknesses of the device. We have shown that excitons cannot dominate in the material at room temperature but they might be in an equilibrium with free electrons and holes. However, the excitons can prevail in the perovskite material at an orthorhombic phase. We have also confirmed that the impact of excitons formation is mostly observable for a case of an open circuit. The excitonic effects are clearly visible by lowering charge carrier concentrations in the middle of sample which causes decreasing of V_{oc}. This work provides new facts about photophysical processes in the lead halide perovskite, which might be useful for the photovoltaics especially for low temperature operation in space environment for powering satellites. In addition, the temperature dependence of the total conductivity has been studied for the perovskite $CH_3NH_3PbI_{3-x}Cl_x$ material. The obtained experimental results clearly demonstrate the orthorhombic to tetragonal phase and the tetragonal to cubic phase transitions. Our analysis suggests the domination of ionic charge carriers in the tetragonal phase. We have proposed the explanation based on the hopping mechanism of ions and bandpass mechanism for electronic charge carriers. It is implied that the high partial ionic conductivity at a room temperature might be a possible explanation of the parasitic effect of hysteresis in trihalide perovskite solar cells which is potentially a problem in a wider application of these perovskite materials.

The results of studies on two types of perovskite solar cells with different HTLs. Cu:NiO_x and Cu:NiO_x/PTAA were analyzed with the experimental and numerical methods. The results demonstrate that significant recombination losses are observed in the PV devices without PTAA material. It leads to a photocurrent and voltage drop of 1–2 mA cm^{-2} and 100–200 mV, respectively, which in turn leads to the loss of efficiency by 2–4%, which values are perovskite thickness dependent. The simulations based on the drift–diffusion model have shown the presence of a dead (recombination) layer at the interface of HTL/perovskite in the solar cell with Cu:NiO_x as HTL. The thickness of this recombination layer is estimated to be 5 nm for a 375 nm thick layer of the perovskite absorber. Results of spatial simulations have confirmed that the dead layer influences the charge carrier density and the electric field distribution. However, the most visible impact is observed on the current distribution within the solar cell. The same parasitic recombination phenomenon could be observed in any PSCs with p–i–n configuration. Therefore, the performed analysis could help to further improve the performance and give a better understanding of recombination mechanisms in perovskite solar cells.

The last studies presented in this thesis concerned the three double–cation PSCs with $PbBr_2$, FABr and CsBr bromide source used in the PSCs. The experimental analyses have shown that $PbBr_2$ cells have approximately 3% lower efficiency than FABr and CsBr per-

ovskite solar cells. It has been found out that the different source of bromide influences the properties of colloidal dispersion solutions which changes the defect states during the crystallization of perovskite layers. The results of numerical simulations have shown that the rates of the trap–assisted recombination in $PbBr_2$ solar cells are two times higher. Therefore, the following may find the application in tandem solar cells, where the use of bromide is necessary for tuning the band–gap.

Bibliography

[1] G. Buxton, *Alternative Energy Technologies: An Introduction with Computer Simulations*. CRC Press, 2014.

[2] W. Tress, *Organic Solar Cells: Theory, Experiment, and Device Simulation*. Springer-Verlag Wien, 2014.

[3] V. Smil, *Energy Transitions: Global and National Perspectives*. ABC-CLIO, 2017.

[4] P. Tans and K. Ralph, "NOAA/ESRL." (https://www.esrl.noaa.gov/gmd/ccgg/trends/data.html), Accessed: 2019-04-28.

[5] C. P. Morice, J. J. Kennedy, N. A. Rayner, and P. D. Jones, "Quantifying uncertainties in global and regional temperature change using an ensemble of observational estimates: The hadcrut4 data set," *J. Geophys. Res. Atmos.*, vol. 117, no. D8, 2012.

[6] I. Capellán-Pérez, M. Mediavilla, C. de Castro, Óscar Carpintero, and L. J. Miguel, "Fossil fuel depletion and socio-economic scenarios: An integrated approach," *Energy*, vol. 77, pp. 641 – 666, 2014.

[7] M. R. Allen, D. J. Frame, C. Huntingford, C. D. Jones, J. A. Lowe, M. Meinshausen, and N. Meinshausen, "Warming caused by cumulative carbon emissions towards the trillionth tonne," *Nature*, vol. 458, p. 1163, 2009.

[8] D. P. van Vuuren, H. van Soest, K. Riahi, L. Clarke, V. Krey, E. Kriegler, J. Rogelj, M. Schaeffer, and M. Tavoni, "Carbon budgets and energy transition pathways," *Environ. Res. Lett.*, vol. 11, no. 7, p. 075002, 2016.

[9] P. Erickson, M. Lazarus, and G. Piggot, "Limiting fossil fuel production as the next big step in climate policy," *Nat. Clim. Change*, vol. 8, no. 12, pp. 1037–1043, 2018.

[10] C.-F. Schleussner, T. K. Lissner, E. M. Fischer, J. Wohland, M. Perrette, A. Golly, J. Rogelj, K. Childers, J. Schewe, K. Frieler, M. Mengel, W. Hare, and M. Schaeffer, "Differential climate impacts for policy-relevant limits to global warming: the case of 1.5 °c and 2 °c," *Earth Syst. Dynam.*, vol. 7, no. 2, pp. 327–351, 2016.

[11] J. Rogelj, A. Popp, K. V. Calvin, G. Luderer, J. Emmerling, D. Gernaat, S. Fujimori, J. Strefler, T. Hasegawa, G. Marangoni, V. Krey, E. Kriegler, K. Riahi, D. P. van Vuuren, J. Doelman,

L. Drouet, J. Edmonds, O. Fricko, M. Harmsen, P. Havlík, F. Humpenöder, E. Stehfest, and M. Tavoni, "Scenarios towards limiting global mean temperature increase below 1.5 °c," *Nat. Clim. Change*, vol. 8, no. 4, pp. 325–332, 2018.

[12] S. Sgouridis, M. Carbajales-Dale, D. Csala, M. Chiesa, and U. Bardi, "Comparative net energy analysis of renewable electricity and carbon capture and storage," *Nat. Energy.*, 2019.

[13] National Renewable Energy Laboratory (NREL), "Solar spectra." https://www.nrel.gov/grid/solar-resource/spectra.html, Accessed: 2019-02-22.

[14] P. Würfel, *Physics of Solar Cells: From Principles to New Concepts*. WILEY-VCH Verlag GmbH & Co. KGaA, 2007.

[15] S. Sze and K. N. Kwok, *Physics of Semiconductor Devices*. John Wiley & Sons, 2006.

[16] J. Nelson, *The Physics of Solar Cells*. Imperial College Press, 2003.

[17] W. Brütting, *Physics of Organic Semiconductors*. Wiley-VCH Verlag GmbH & Co. KGaA, 2006.

[18] J.-W. Lee, D.-H. Kim, H.-S. Kim, S.-W. Seo, S. M. Cho, and N.-G. Park, "Formamidinium and cesium hybridization for photo- and moisture-stable perovskite solar cell," *Adv. Energy Mater.*, vol. 5, no. 20, p. 1501310, 2015.

[19] National Renewable Energy Laboratory (NREL), "Chart of best research-cell efficiencies." https://www.nrel.gov/pv/assets/images/efficiency-chart.png, Accessed: 2019-04-29.

[20] L. M. Herz, "Charge-carrier dynamics in organic-inorganic metal halide perovskites," *Annu. Rev. Phys. Chem.*, vol. 67, no. 1, pp. 65–89, 2016.

[21] T. Leijtens, S. D. Stranks, G. E. Eperon, R. Lindblad, E. M. J. Johansson, I. J. McPherson, H. Rensmo, J. M. Ball, M. M. Lee, and H. J. Snaith, "Electronic properties of meso-superstructured and planar organometal halide perovskite films: charge trapping, photodoping, and carrier mobility," *ACS Nano*, vol. 8, no. 7, pp. 7147–7155, 2014.

[22] A. Miyata, A. Mitioglu, P. Plochocka, O. Portugall, J. T.-W. Wang, S. D. Stranks, H. J. Snaith, and R. J. Nicholas, "Direct measurement of the exciton binding energy and effective masses for charge carriers in an organic-inorganic tri-halide perovskite," *Nat. Phys.*, vol. 11, no. 7, pp. 582–587, 2015.

[23] Y. M. Wang, S. Bai, L. Cheng, N. N. Wang, J. P. Wang, F. Gao, and W. Huang, "High-efficiency flexible solar cells based on organometal halide perovskites," *Adv. Mater.*, vol. 28, no. 22, pp. 4532–4540, 2016.

[24] R. L. Milot, G. E. Eperon, H. J. Snaith, M. B. Johnston, and L. M. Herz, "Temperature-dependent charge-carrier dynamics in $CH_3NH_3PbI_3$ perovskite thin films," *Adv. Funct. Mater.*, vol. 25, no. 39, pp. 6218–6227, 2015.

[25] N. Onoda-Yamamuro, T. Matsuo, and H. Suga, "Dielectric study of $CH_3NH_3PbX_3$ (X = Cl, Br, I)," *J. Phys. Chem. Solids*, vol. 53, no. 7, pp. 935–939, 1992.

[26] B. Maynard, Q. Long, E. A. Schiff, M. Yang, K. Zhu, R. Kottokkaran, H. Abbas, and V. L. Dalal, "Electron and hole drift mobility measurements on methylammonium lead iodide perovskite solar cells," *Appl. Phys. Lett.*, vol. 108, no. 17, pp. 1–5, 2016.

[27] C. C. Stoumpos, C. D. Malliakas, and M. G. Kanatzidis, "Organic tin and lead iodide perovskites with organic cations: unique semiconductors, with phase transitions and near-infrared photoluminescent properties," *Inorg. Chem.*, vol. 52, no. 15, pp. 9019–9038, 2013.

[28] Y. Kawamura, H. Mashiyama, and K. Hasebe, "Structural study on cubic-tetragonal transition of $CH_3NH_3PbI_3$," *J. Phys. Soc. Jpn.*, vol. 71, no. 7, pp. 1694–1697, 2002.

[29] T. Baikie, Y. Fang, J. M. Kadro, M. Schreyer, F. Wei, S. G. Mhaisalkar, M. Graetzel, and T. J. White, "Synthesis and crystal chemistry of the hybrid perovskite $(CH_3NH_3)PbI_3$ for solid-state sensitised solar cell applications," *J. Mater. Chem. A*, vol. 1, no. 18, pp. 5628–5641, 2013.

[30] H. J. Snaith, A. Abate, J. M. Ball, G. E. Eperon, T. Leijtens, N. K. Noel, S. D. Stranks, J. T. W. Wang, K. Wojciechowski, and W. Zhang, "Anomalous hysteresis in perovskite solar cells," *J. Phys. Chem. Lett.*, vol. 5, no. 9, pp. 1511–1515, 2014.

[31] A. K. Jena, H.-W. Chen, A. Kogo, Y. Sanehira, M. Ikegami, and T. Miyasaka, "The interface between FTO and the TiO_2 compact layer can be one of the origins to hysteresis in planar heterojunction perovskite solar cells," *ACS Appl. Mater. Interfaces*, vol. 7, no. 18, pp. 9817–9823, 2015.

[32] B. Chen, M. Yang, S. Priya, and K. Zhu, "Origin of J-V hysteresis in perovskite solar cells," *J. Phys. Chem. Lett.*, vol. 7, no. 5, pp. 905–917, 2016.

[33] S. Van Reenen, M. Kemerink, and H. J. Snaith, "Modeling anomalous hysteresis in perovskite solar Cells," *J. Phys. Chem. Lett*, vol. 6, no. 19, pp. 3808–3814, 2015.

[34] A. M. A. Leguy, J. M. Frost, A. P. McMahon, V. G. Sakai, W. Kochelmann, C. Law, X. Li, F. Foglia, A. Walsh, B. C. O'Regan, J. Nelson, J. T. Cabral, and P. R. F. Barnes, "The dynamics of methylammonium ions in hybrid organic-inorganic perovskite solar cells," *Nat. Commun.*, vol. 6, p. 7124, 2015.

[35] W. Tress, N. Marinova, T. Moehl, S. M. Zakeeruddin, M. K. Nazeeruddin, and M. Gratzel, "Understanding the rate-dependent J-V hysteresis, slow time component, and aging in $CH_3NH_3PbI_3$ perovskite solar cells: the role of a compensated electric field," *Energy Environ. Sci.*, vol. 8, no. 3, pp. 995–1004, 2015.

[36] L. Meng, J. You, and Y. Yang, "Addressing the stability issue of perovskite solar cells for commercial applications," *Nature Comm.*, vol. 9, no. 1, p. 5265, 2018.

[37] B. A. Gregg and M. C. Hanna, "Comparing organic to inorganic photovoltaic cells: Theory, experiment, and simulation," *J. Appl. Phys.*, vol. 93, no. 6, pp. 3605–3614, 2003.

[38] B. A. Gregg, "Excitonic solar cells," *J. Phys. Chem. B*, vol. 107, no. 20, pp. 4688–4698, 2003.

[39] A. Cheknane, H. S. Hilal, F. Djeffal, B. Benyoucef, and J.-P. Charles, "An equivalent circuit approach to organic solar cell modelling," *Microelectron. J.*, vol. 39, no. 10, pp. 1173 – 1180, 2008.

[40] G. A. Sewvandi, D. Hu, C. Chen, H. Ma, T. Kusunose, Y. Tanaka, S. Nakanishi, and Q. Feng, "Antiferroelectric-to-ferroelectric switching in $CH_3NH_3PbI_3$ perovskite and its potential role in effective charge separation in perovskite solar cells," *Phys. Rev. Applied*, vol. 6, p. 024007, 2016.

[41] L. Meng, Y. Shang, Q. Li, Y. Li, X. Zhan, Z. Shuai, R. G. E. Kimber, and A. B. Walker, "Dynamic monte carlo simulation for highly efficient polymer blend photovoltaics," *J. Phys. Chem. B*, vol. 114, no. 1, pp. 36–41, 2010.

[42] H. Xue, E. Birgersson, and R. Stangl, "Correlating variability of modeling parameters with photovoltaic performance: Monte carlo simulation of a meso-structured perovskite solar cell," *Appl. Energ.*, vol. 237, pp. 131 – 144, 2019.

[43] L. J. A. Koster, E. C. P. Smits, V. D. Mihailetchi, and P. W. M. Blom, "Device model for the operation of polymer/fullerene bulk heterojunction solar cells," *Phys. Rev. B*, vol. 72, p. 085205, 2005.

[44] G. A. Buxton and N. Clarke, "Computer simulation of polymer solar cells," *Model. Simul. Mater. Sci. Eng.*, vol. 15, pp. 13–26, dec 2006.

[45] J. A. Barker, C. M. Ramsdale, and N. C. Greenham, "Modeling the current-voltage characteristics of bilayer polymer photovoltaic devices," *Phys. Rev. B*, vol. 67, p. 075205, 2003.

[46] I. Hwang and N. C. Greenham, "Modeling photocurrent transients in organic solar cells," *Nanotechnology*, vol. 19, p. 424012, sep 2008.

[47] X. Ren, Z. Wang, W. E. I. Sha, and W. C. H. Choy, "Exploring the way to approach the efficiency limit of perovskite solar cells by drift-diffusion model," *ACS Photonics*, vol. 4, pp. 934–942, 2017.

[48] T. S. Sherkar, C. Momblona, L. Gil-Escrig, H. J. Bolink, and L. J. A. Koster, "Improving Perovskite Solar Cells: Insights From a Validated Device Model," *Adv. Energy Mater.*, vol. 7, no. 13, p. 1602432, 2017.

[49] P. Calado, A. M. Telford, D. Bryant, X. Li, J. Nelson, B. C. O'Regan, and P. R. F. Barnes, "Evidence for ion migration in hybrid perovskite solar cells with minimal hysteresis," *Nat. Commun.*, vol. 7, p. 13831, 2016.

[50] G. Richardson, S. O'Kane, R. G. Niemann, T. Peltola, J. M. Foster, P. J. Cameron, and A. Walker, "Can slow-moving ions explain hysteresis in the current-voltage curves of perovskite solar cells?," *Energy Environ. Sci.*, vol. 9, pp. 1476–1485, 2016.

[51] D. Walter, A. Fell, Y. Wu, T. Duong, C. Barugkin, N. Wu, T. White, and K. Weber, "Transient photovoltage in perovskite solar cells: Interaction of trap-mediated recombination and migration of multiple ionic species," *J. Phys. Chem. C*, vol. 122, no. 21, pp. 11270–11281, 2018.

[52] G. F. Burkhard, E. T. Hoke, and M. D. McGehee, "Accounting for interference, scattering, and electrode absorption to make accurate internal quantum efficiency measurements in organic and other thin solar cells," *Adv. Mater.*, vol. 22, no. 30, pp. 3293–3297, 2010.

[53] E. Shaaban, M. Kaid, and M. Ali, "X-ray analysis and optical properties of nickel oxide thin films," *J. Alloy. Comp.*, vol. 613, pp. 324 – 329, 2014.

[54] G. J. Hedley, A. J. Ward, A. Alekseev, C. T. Howells, E. R. Martins, L. A. Serrano, G. Cooke, A. Ruseckas, and I. D. Samuel, "Determining the optimum morphology in high-performance polymer-fullerene organic photovoltaic cells," *Nature Comm.*, vol. 4, pp. 1–10, 2013.

[55] B. Johnev, *Chemical engineering of the electronic properties of ITO-organics interface in Phthalocyanine/C60-Fullerene organic solar cell*. PhD thesis, Freie Universit¨at Berlin, 2005.

[56] L. A. A. Pettersson, L. S. Roman, and O. Inganäs, "Modeling photocurrent action spectra of photovoltaic devices based on organic thin films," *J. Appl. Phys.*, vol. 86, no. 1, pp. 487–496, 1999.

[57] W. P. Su, J. R. Schrieffer, and A. J. Heeger, "Soliton excitations in polyacetylene," *Phys. Rev. B*, vol. 22, pp. 2099–2111, 1980.

[58] D. Głowienka and J. Szmytkowski, "Influence of excitons interaction with charge carriers on photovoltaic parameters in organic solar cells," *Chem. Phys.*, vol. 503, pp. 31–38, 2018.

[59] D. Głowienka and J. Szmytkowski, "Numerical modeling of exciton impact in two crystallographic phases of the organo-lead halide perovskite ($CH_3NH_3PbI_3$) solar cell," *Semicond. Sci. Technol.*, vol. 34, no. 3, p. 035018, 2019.

[60] L. Onsager, "Deviations from ohm's law in weak electrolytes," *J. Chem. Phys.*, vol. 2, no. 9, pp. 599–615, 1934.

[61] C. L. Braun, "Electric field assisted dissociation of charge transfer states as a mechanism of photocarrier production," *J. Chem. Phys.*, vol. 80, no. 9, pp. 4157–4161, 1984.

[62] T. E. Goliber and J. H. Perlstein, "Analysis of photogeneration in a doped polymer system in terms of a kinetic model for electric-field-assisted dissociation of charge-transfer states," *J. Chem. Phys.*, vol. 80, no. 9, pp. 4162–4167, 1984.

[63] V. D'Innocenzo, G. Grancini, M. J. P. Alcocer, A. R. S. Kandada, S. D. Stranks, M. M. Lee, G. Lanzani, H. J. Snaith, and A. Petrozza, "Excitons versus free charges in organo-lead tri-halide perovskites," *Nat. Commun.*, vol. 5, p. 3586, 2014.

[64] S. D. Stranks, G. E. Eperon, G. Grancini, C. Menelaou, M. J. P. Alcocer, T. Leijtens, L. M. Herz, A. Petrozza, and H. J. Snaith, "Electron-hole diffusion lengths exceeding 1 micrometer in an organometal trihalide perovskite absorber," *Science*, vol. 342, no. 2013, pp. 341–344, 2014.

[65] S. Selberherr, *Analysis and Simulation of Semiconductor Devices*. Springer-Verlag Wien, 1984.

[66] J. G. Simmons and G. W. Taylor, "Nonequilibrium steady-state statistics and associated effects for insulators and semiconductors containing an arbitrary distribution of traps," *Phys. Rev. B*, vol. 4, no. 2, pp. 502–511, 1971.

[67] R. C. I. MacKenzie, T. Kirchartz, G. F. A. Dibb, and J. Nelson, "Modeling nongeminate recombination in P3HT:PCBM solar cells," *J. Phys. Chem. C*, vol. 115, no. 19, pp. 9806–9813, 2011.

[68] L. F. Hernández-García, O. Ramírez-Sánchez, V. Cabrera-Arenas, and L. M. Reséndiz-Mendoza, "A gaussian model for recombination via carrier-trap distributions in organic solar cells," *Journal of Computational Electronics*, vol. 15, no. 3, pp. 1103–1109, 2016.

[69] S. A. Hawks, G. Li, Y. Yang, and R. A. Street, "Band tail recombination in polymer:fullerene organic solar cells," *J. Appl. Phys.*, vol. 116, no. 7, p. 074503, 2014.

[70] T. Kirchartz, B. E. Pieters, J. Kirkpatrick, U. Rau, and J. Nelson, "Recombination via tail states in polythiophene:fullerene solar cells," *Phys. Rev. B*, vol. 83, p. 115209, 2011.

[71] H. T. Nicolai, M. M. Mandoc, and P. W. M. Blom, "Electron traps in semiconducting polymers: Exponential versus gaussian trap distribution," *Phys. Rev. B*, vol. 83, p. 195204, 2011.

[72] G. Lakhwani, A. Rao, and R. H. Friend, "Bimolecular recombination in organic photovoltaics," *Annu. Rev. Phys. Chem.*, vol. 65, no. 1, pp. 557–581, 2014.

[73] C. Deibel, A. Wagenpfahl, and V. Dyakonov, "Origin of reduced polaron recombination in organic semiconductor devices," *Phys. Rev. B*, vol. 80, p. 075203, 2009.

[74] J. Szmytkowski, "Analysis of the image force effects on the recombination at the donor–acceptor interface in organic bulk heterojunction solar cells," *Chem. Phys. Lett.*, vol. 470, no. 1, pp. 123 – 125, 2009.

[75] J. Szmytkowski, "Nongeminate recombination in organic bulk heterojunction solar cells: contribution of exciton–polaron interaction," *Phys. Stat. Sol. RRL*, vol. 6, no. 7, pp. 300–302, 2012.

[76] A. Wagenpfahl, "Mobility dependent recombination models for organic solar cells," *J. Phys. Condens. Matter*, vol. 29, no. 37, p. 373001, 2017.

[77] A. R. Beattie and P. T. Landsberg, "Auger effect in semiconductors," *Proc. Royal Soc. A*, vol. 249, no. 1256, pp. 16–29, 1959.

[78] M. Lundstrom and R. Schuelke, "Modeling semiconductor heterojunctions in equilibrium," *Solid-State Electron.*, vol. 25, no. 8, pp. 683 – 691, 1982.

[79] M. S. Lundstrom and R. J. Schuelke, "Numerical analysis of heterostructure semiconductor devices," *IEEE Trans. Electron Devices*, vol. 30, no. 9, pp. 1151–1159, 1983.

[80] M. Gruber, B. Stickler, G. Trimmel, F. Schurrer, and K. Zojer, "Impact of energy alignment and morphology on the efficiency in inorganic–organic hybrid solar cells," *Org. Electron.*, vol. 11, no. 12, pp. 1999 – 2011, 2010.

[81] D. L. Scharfetter and H. K. Gummel, "Large-Signal Analysis of a Silicon Read Diode Oscillator," *IEEE Trans. Electron Devices*, vol. 16, no. 1, pp. 64–77, 1969.

[82] Z. S. Wang, W. E. I. Sha, and W. C. H. Choy, "Exciton delocalization incorporated drift-diffusion model for bulk-heterojunction organic solar cells," *J. Appl. Phys.*, vol. 120, no. 21, p. 213101, 2016.

[83] A. de Mari, *Accurate numerical steady-state and transient one-dimiensional solutions of semiconductor devices*. PhD thesis, California Institute of Technology, 1968.

[84] D. Głowienka and J. Szmytkowski, "Modeling of transient photocurrent in organic semiconductors incorporating the annihilation of excitons on charge carriers," *Acta Phys. Pol. A*, vol. 132, no. 2, pp. 397–400, 2017.

[85] J. Kalinowski, W. Stampor, J. Szmytkowski, D. Virgili, M. Cocchi, V. Fattori, and C. Sabatini, "Coexistence of dissociation and annihilation of excitons on charge carriers in organic phosphorescent emitters," *Phys. Rev. B*, vol. 74, p. 085316, 2006.

[86] S. Reineke, K. Walzer, and K. Leo, "Triplet-exciton quenching in organic phosphorescent light-emitting diodes with ir-based emitters," *Phys. Rev. B*, vol. 75, p. 125328, 2007.

[87] M. Shao, L. Yan, M. Li, I. Ilia, and B. Hu, "Triplet–charge annihilation versus triplet–triplet annihilation in organic semiconductors," *J. Mater. Chem. C*, vol. 1, pp. 1330–1336, 2013.

[88] Q. Wang, I. W. H. Oswald, M. R. Perez, H. Jia, B. E. Gnade, and M. A. Omary, "Exciton and polaron quenching in doping-free phosphorescent organic light-emitting diodes from a Pt(II)-based fast phosphor," *Adv. Funct. Mater.*, vol. 23, no. 43, pp. 5420–5428, 2013.

[89] D. Yuan, L. Niu, Q. Chen, W. Jia, P. Chen, and Z. Xiong, "The triplet-charge annihilation in copolymer-based organic light emitting diodes: through the "scattering channel" or the "dissociation channel"?," *Phys. Chem. Chem. Phys.*, vol. 17, pp. 27609–27614, 2015.

[90] J. S. Price and N. C. Giebink, "Quantum efficiency harmonic analysis of exciton annihilation in organic light emitting diodes," *Appl. Phys. Lett.*, vol. 106, no. 26, p. 263302, 2015.

[91] H. van Eersel, P. A. Bobbert, R. A. J. Janssen, and R. Coehoorn, "Effect of Förster-mediated triplet-polaron quenching and triplet-triplet annihilation on the efficiency roll-off of organic light-emitting diodes," *J. Appl. Phys.*, vol. 119, no. 16, p. 163102, 2016.

[92] A. J. Ferguson, N. Kopidakis, S. E. Shaheen, and G. Rumbles, "Quenching of excitons by holes in poly(3-hexylthiophene) films," *J. Phys. Chem. C*, vol. 112, no. 26, pp. 9865–9871, 2008.

[93] I. A. Howard, J. M. Hodgkiss, X. Zhang, K. R. Kirov, H. A. Bronstein, C. K. Williams, R. H. Friend, S. Westenhoff, and N. C. Greenham, "Charge recombination and exciton annihilation reactions in conjugated polymer blends," *J. Am. Chem. Soc.*, vol. 132, no. 1, pp. 328–335, 2010.

[94] A. J. Ferguson, N. Kopidakis, S. E. Shaheen, and G. Rumbles, "Dark carriers, trapping, and activation control of carrier recombination in neat P3HT and P3HT:PCBM blends," *J. Phys. Chem. C*, vol. 115, no. 46, pp. 23134–23148, 2011.

[95] J. M. Hodgkiss, S. Albert-Seifried, A. Rao, A. J. Barker, A. R. Campbell, R. A. Marsh, and R. H. Friend, "Exciton-charge annihilation in organic semiconductor films," *Adv. Funct. Mater.*, vol. 22, no. 8, pp. 1567–1577, 2012.

[96] J. Szmytkowski, "Four-body recombination in organic bulk heterojunction solar cells: an alternative interpretation," *Semicond. Sci. Technol.*, vol. 28, no. 5, p. 052002, 2013.

[97] L. Tzabari, V. Zayats, and N. Tessler, "Exciton annihilation as bimolecular loss in organic solar cells," *J. Appl. Phys.*, vol. 114, no. 15, p. 154514, 2013.

[98] B. Verreet, A. Bhoolokam, A. Brigeman, R. Dhanker, D. Cheyns, P. Heremans, A. Stesmans, N. C. Giebink, and B. P. Rand, "Reducing exciton-polaron annihilation in organic planar heterojunction solar cells," *Phys. Rev. B*, vol. 90, p. 115304, 2014.

[99] J. Szmytkowski, "High order of nongeminate recombination in organic bulk heterojunction solar cells," *Semicond. Sci. Technol.*, vol. 29, no. 7, p. 075022, 2014.

[100] W. A. Koopman, M. Natali, G. P. Donati, M. Muccini, and S. Toffanin, "Charge–exciton interaction rate in organic field-effect transistors by means of transient photoluminescence electromodulated spectroscopy," *ACS Photonics*, vol. 4, no. 2, pp. 282–291, 2017.

[101] R. Coehoorn, L. Zhang, P. A. Bobbert, and H. van Eersel, "Effect of polaron diffusion on exciton-polaron quenching in disordered organic semiconductors," *Phys. Rev. B*, vol. 95, p. 134202, 2017.

[102] K. C. Kao, "Electrical transport in solids with particular reference to organic semiconductors," *International series in the science of the Solid State*, 1981.

[103] T. Kirchartz, B. E. Pieters, K. Taretto, and U. Rau, "Electro-optical modeling of bulk heterojunction solar cells," *Journal of Applied Physics*, vol. 104, no. 9, p. 094513, 2008.

[104] I. Hwang, C. R. McNeill, and N. C. Greenham, "Drift-diffusion modeling of photocurrent transients in bulk heterojunction solar cells," *J. Appl. Phys.*, vol. 106, no. 9, p. 094506, 2009.

[105] Z. S. Wang, W. E. I. Sha, and W. C. H. Choy, "Exciton delocalization incorporated drift-diffusion model for bulk-heterojunction organic solar cells," *J. Appl. Phys.*, vol. 120, no. 21, p. 213101, 2016.

[106] L. Lu, W. Chen, T. Xu, and L. Yu, "High-performance ternary blend polymer solar cells involving both energy transfer and hole relay processes," *Nature Comm.*, vol. 6, p. 7327, 2015.

[107] Z. He, C. Zhong, X. Huang, W.-Y. Wong, H. Wu, L. Chen, S. Su, and Y. Cao, "Simultaneous enhancement of open-circuit voltage, short-circuit current density, and fill factor in polymer solar cells," *Adv. Mater.*, vol. 23, no. 40, pp. 4636–4643, 2011.

[108] Bouchriha, H., Delacote, G., Delannoy, P., and Schott, M., "Interaction of triplet excitons with trapped and free holes in crystalline anthracene. exciton quenching, current enhancement and magnetic field effects," *J. Phys. France*, vol. 35, no. 7-8, pp. 577–587, 1974.

[109] V. D. Mihailetchi, L. J. A. Koster, J. C. Hummelen, and P. W. M. Blom, "Photocurrent generation in polymer-fullerene bulk heterojunctions," *Phys. Rev. Lett.*, vol. 93, p. 216601, 2004.

[110] L. Zuo, J. Yao, H. Li, and H. Chen, "Assessing the origin of the S-shaped I–V curve in organic solar cells: an improved equivalent circuit model," *Sol. Energy Mater Sol. Cells*, vol. 122, pp. 88 – 93, 2014.

[111] J. Wang, X. Ren, S. Shi, C. Leung, and P. K. Chan, "Charge accumulation induced S-shape J–V curves in bilayer heterojunction organic solar cells," *Org. Electron.*, vol. 12, no. 6, pp. 880 – 885, 2011.

[112] Y. Yamada, T. Nakamura, M. Endo, A. Wakamiya, and Y. Kanemitsu, "Photoelectronic responses in solution-processed perovskite $CH_3NH_3PbI_3$ solar cells studied by photoluminescence and photoabsorption spectroscopy," *IEEE J. Photovolt.*, vol. 5, no. 1, pp. 401–405, 2015.

[113] Q. Lin, A. Armin, R. C. R. Nagiri, P. L. Burn, and P. Meredith, "Electro-optics of perovskite solar cells," *Nat. Photonics*, vol. 9, no. 2, pp. 106–112, 2015.

[114] M. Saba, F. Quochi, A. Mura, and G. Bongiovanni, "Excited state properties of hybrid perovskites," *Acc. Chem. Res.*, vol. 49, no. 1, pp. 166–173, 2016.

[115] D. Głowienka, T. Miruszewski, and J. Szmytkowski, "The domination of ionic conductivity in tetragonal phase of the organometal halide perovskite $CH_3NH_3PbI_{3-x}Cl_x$," *Solid State Sci.*, vol. 82, pp. 19 – 23, 2018.

[116] H. Wang, L. Whittaker-Brooks, and G. R. Fleming, "Exciton and free charge dynamics of methylammonium lead iodide perovskites are different in the tetragonal and orthorhombic phases," *J. Phys. Chem. C*, vol. 119, no. 34, pp. 19590–19595, 2015.

[117] M. Hirasawa, T. Ishihara, T. Goto, K. Uchida, and N. Miura, "Magnetoabsorption of the lowest exciton in perovskite-type compound $(CH_3NH_3)PbI_3$," *Physica B*, vol. 201, pp. 427–430, 1994.

[118] Y. Miyazawa, M. Ikegami, H.-W. Chen, T. Ohshima, M. Imaizumi, K. Hirose, and T. Miyasaka, "Tolerance of perovskite solar cell to high-energy particle irradiations in space environment," *Science*, vol. 2, pp. 148 – 155, 2018.

[119] Y. Zhou and A. Gray-Weale, "A numerical model for charge transport and energy convention of perovskite solar cells," *Phys. Chem. Chem. Phys.*, vol. 18, pp. 4476–4486, 2015.

[120] J. Mizusaki, K. Arai, and K. Fueki, "Ionic conduction of the perovskite-type halides," *Solid State Ion.*, vol. 11, no. 3, pp. 203–211, 1983.

[121] A. Dualeh, T. Moehl, N. Tétreault, J. Teuscher, P. Gao, M. K. Nazeeruddin, and M. Grätzel, "Impedance spectroscopic analysis of lead iodide perovskite-sensitized solid-state solar cells," *ACS Nano*, vol. 8, no. 1, pp. 362–373, 2014.

[122] C. Eames, J. M. Frost, P. R. F. Barnes, B. C. O'Regan, A. Walsh, and M. S. Islam, "Ionic transport in hybrid lead iodide perovskite solar cells," *Nat. Commun.*, vol. 6, p. 7497, 2015.

[123] W. Weppner and R. A. Huggins, "Ionic conductivity of alkali metal chloroaluminates," *Phys. Lett. A*, vol. 58, no. 4, pp. 245–248, 1976.

[124] I. Riess, "Four point Hebb-Wagner polarization method for determining the electronic conductivity in mixed ionic-electronic conductors," *Solid State Ion.*, vol. 51, no. 3, pp. 219–229, 1992.

[125] I. Riess, "Measurement of ionic conductivity in semiconductors and metals," *Solid State Ion.*, vol. 44, no. 3-4, pp. 199–205, 1991.

[126] I. Riess, "Review of the limitation of the Hebb-Wagner polarization method for measuring partial conductivities in mixed ionic electronic conductors," *Solid State Ion.*, vol. 91, no. 3-4, pp. 221–232, 1996.

[127] K. C. Lee and H. I. Yoo, "Hebb-Wagner-type polarization/relaxation in the presence of the cross effect between electronic and ionic flows in a mixed conductor," *J. Phys. Chem. Solids*, vol. 60, no. 7, pp. 911–927, 1999.

[128] T. Miruszewski, J. Karczewski, B. Bochentyn, P. Jasinski, M. Gazda, and B. Kusz, "Determination of the ionic conductivity of Sr-doped lanthanum manganite by modified Hebb-Wagner technique," *J. Phys. Chem. Solids*, vol. 91, pp. 163–169, 2016.

[129] K. H. Kim, T. Lee, W. Joo, and H. I. Yoo, "Current vs. voltage behavior of Hebb-Wagner ion-blocking cell through compound ($Bi_{1.46}Y_{0.54}O_3$) decomposition and decomposition kinetics," *Solid State Ion.*, vol. 267, pp. 9–15, 2014.

[130] C. Piermarocchi, F. Tassone, V. Savona, A. Quattropani, and P. Schwendimann, "Exciton Formation Rates in GaAs/$Al_xGa_{1-x}As$ Quantum Wells," *Phys. Rev. B*, vol. 55, no. 3, pp. 1333–1336, 1997.

[131] Z. Xiao, Q. Dong, C. Bi, Y. Shao, Y. Yuan, and J. Huang, "Solvent annealing of perovskite-induced crystal growth for photovoltaic-device efficiency enhancement," *Adv. Mater.*, vol. 26, no. 37, pp. 6503–6509, 2014.

[132] H.-S. Kim, C.-R. Lee, J.-H. Im, K.-B. Lee, T. Moehl, A. Marchioro, S.-J. Moon, R. Humphry-Baker, J.-H. Yum, J. E. Moser, M. Grätzel, and N.-G. Park, "Lead iodide perovskite sensitized all-solid-state submicron thin film mesoscopic solar cell with efficiency exceeding 9%," *Sci. Rep.*, vol. 2, p. 591, 2012.

[133] C. Wehrenfennig, G. E. Eperon, M. B. Johnston, H. J. Snaith, and L. M. Herz, "High charge carrier mobilities and lifetimes in organolead trihalide perovskites," *Adv. Mater.*, vol. 26, no. 10, pp. 1584–1589, 2014.

[134] M. N. Saha, "On a physical theory of stellar spectra," *Proc. Royal Soc. A*, vol. 99, no. 697, p. 135, 1921.

[135] D. A. Valverde-Chávez, C. Ponseca, C. Stoumpos, A. Yartsev, M. G. Kanatzidis, V. Sundström, and D. G. Cooke, "Intrinsic femtosecond charge generation dynamics in single crystal $CH_3NH_3PbI_3$," *Energy Environ. Sci.*, vol. 8, pp. 3700–3707, 2015.

[136] N. Sestu, M. Cadelano, V. Sarritzu, F. Chen, D. Marongiu, R. Piras, M. Mainas, F. Quochi, M. Saba, A. Mura, and G. Bongiovanni, "Absorption F-sum rule for the exciton binding energy in methylammonium lead halide perovskites," *J. Phys. Chem. Lett.*, vol. 6, no. 22, pp. 4566–4572, 2015.

[137] H. Zhang, X. Qiao, Y. Shen, T. Moehl, S. M. Zakeeruddin, M. Grätzel, and M. Wang, "Photovoltaic behaviour of lead methylammonium triiodide perovskite solar cells down to 80 *K*," *J. Mater. Chem. A*, vol. 3, pp. 11762–11767, 2015.

[138] P. E. Selbmann, M. Gulia, F. Rossi, E. Molinari, and P. Lugli, "Coupled free-carrier and exciton relaxation in optically excited semiconductors," *Phys. Rev. B*, vol. 54, pp. 4660–4673, Aug 1996.

[139] M. Kira, W. Hoyer, T. Stroucken, and S. W. Koch, "Exciton formation in semiconductors and the influence of a photonic environment," *Phys. Rev. Lett.*, vol. 87, p. 176401, Oct 2001.

[140] V. Janković and N. Vukmirović, "Dynamics of exciton formation and relaxation in photoexcited semiconductors," *Phys. Rev. B*, vol. 92, p. 235208, Dec 2015.

[141] S. Shao, J. Liu, H. H. Fang, L. Qiu, G. H. ten Brink, J. C. Hummelen, L. J. A. Koster, and M. A. Loi, "Efficient perovskite solar cells over a broad temperature window: the role of the charge carrier extraction," *Adv. Energy Mater.*, vol. 7, no. 22, p. 1701305, 2017.

[142] M. Maeda, M. Hattori, A. Hotta, and I. Suzuki, "Dielectric studies on $CH_3NH_3PbX_3$ (X = Cl and Br) single cystals," *J. Phys. Soc. Jpn.*, vol. 66, no. 5, pp. 1508–1511, 1997.

[143] Z.-L. Tseng, C.-H. Chiang, and C.-G. Wu, "Surface engineering of ZnO thin film for high efficiency planar perovskite solar cells," *Sci. Rep.*, vol. 5, p. 13211, 2015.

[144] H.-B. Kim, H. Choi, J. Jeong, S. Kim, B. Walker, S. Song, and J. Y. Kim, "Mixed solvents for the optimization of morphology in solution-processed, inverted-type perovskite/fullerene hybrid Solar cells," *Nanoscale*, vol. 6, no. 12, pp. 6679–6683, 2014.

[145] J. Lian, Q. Wang, Y. Yuan, Y. Shao, and J. Huang, "Organic solvent vapor sensitive methylammonium lead trihalide film formation for efficient hybrid perovskite solar cells," *J. Mater. Chem. A*, vol. 3, no. 17, pp. 9146–9151, 2015.

[146] K. Wu, A. Bera, C. Ma, Y. Du, Y. Yang, L. Li, and T. Wu, "Temperature-Dependent Excitonic Photoluminescence of Hybrid Organometal Halide Perovskite Films," *Phys. Chem. Chem. Phys.*, vol. 16, no. 41, pp. 22476–22481, 2014.

[147] D. Koushik, W. J. H. Verhees, Y. Kuang, S. Veenstra, D. Zhang, M. A. Verheijen, M. Creatore, and R. E. I. Schropp, "High-efficiency humidity-stable planar perovskite solar cells based on atomic layer architecture," *Energy Environ. Sci.*, vol. 10, no. 1, pp. 91–100, 2017.

[148] H. Yu, F. Wang, F. Xie, W. Li, J. Chen, and N. Zhao, "The role of chlorine in the formation process of "$CH_3NH_3PbI_{3-x}Cl_x$" perovskite," *Adv. Funct. Mater.*, vol. 24, no. 45, pp. 7102–7108, 2014.

[149] C. Motta, F. El-Mellouhi, and S. Sanvito, "Charge carrier mobility in hybrid halide perovskites," *Sci. Rep.*, vol. 5, no. 1, p. 12746, 2015.

[150] M. V. Khenkin, D. V. Amasev, S. A. Kozyukhin, A. V. Sadovnikov, E. A. Katz, and A. G. Kazanskii, "Temperature and spectral dependence of $CH_3NH_3PbI_3$ films photoconductivity," *Applied Physics Letters*, vol. 110, no. 22, p. 222107, 2017.

[151] W. Peng, J. Yin, K. T. Ho, O. Ouellette, M. De Bastiani, B. Murali, O. El Tall, C. Shen, X. Miao, J. Pan, E. Alarousu, J. H. He, B. S. Ooi, O. F. Mohammed, E. Sargent, and O. M. Bakr, "Ultralow self-doping in two-dimensional hybrid perovskite single crystals," *Nano Lett.*, vol. 17, no. 8, pp. 4759–4767, 2017.

[152] J. Kim, J. Kwon, M. Kim, J. Do, D. Lee, and H. Han, "Low-dielectric-constant polyimide aerogel composite films with low water uptake," *Polym. J.*, vol. 48, no. 7, pp. 829–834, 2016.

[153] P. S. Whitfield, N. Herron, W. E. Guise, K. Page, Y. Q. Cheng, I. Milas, and M. K. Crawford, "Structures, phase transitions and tricritical behavior of the hybrid perovskite methyl ammonium lead iodide," *Sci. Rep.*, vol. 6, p. 35685, 2016.

[154] A. Dobrovolsky, A. Merdasa, E. L. Unger, A. Yartsev, and I. G. Scheblykin, "Defect-induced local variation of crystal phase transition temperature in metal-halide perovskites," *Nature Communications*, vol. 8, no. 1, pp. 1–7, 2017.

[155] H. D. Kim, H. Ohkita, H. Benten, and S. Ito, "Photovoltaic performance of perovskite solar cells with different grain sizes," *Adv. Mater.*, vol. 28, no. 5, pp. 917–922, 2016.

[156] R. L. Narayan and S. V. Suryanarayana, "Transport properties of the perovskite-type halides," *Mater. Lett.*, vol. 11, no. 8-9, pp. 305–308, 1991.

[157] T. Kuku, "Ionic transport and galvanic cell discharge characteristics of $CuPbI_3$ thin films," *Thin Solid Films*, vol. 325, no. 1-2, pp. 246–250, 1998.

[158] W. E. I. Sha, X. Ren, L. Chen, and W. C. H. Choy, "The efficiency limit of $CH_3NH_3PbI_3$ perovskite solar cells," *Appl. Phys. Lett.*, vol. 106, no. 22, p. 221104, 2015.

[159] D. Yang, R. Yang, K. Wang, C. Wu, X. Zhu, J. Feng, X. Ren, G. Fang, S. Priya, and S. F. Liu, "High efficiency planar-type perovskite solar cells with negligible hysteresis using EDTA-complexed SnO2," *Nat. Commun.*, vol. 9, no. 1, p. 3239, 2018.

[160] T. S. Sherkar, C. Momblona, L. Gil-Escrig, J. Ávila, M. Sessolo, H. J. Bolink, and L. J. A. Koster, "Recombination in perovskite solar cells: Significance of grain boundaries, interface traps, and defect ions," *ACS Energy Lett.*, vol. 2, no. 5, pp. 1214–1222, 2017.

[161] G.-J. A. H. Wetzelaer, M. Scheepers, A. M. Sempere, C. Momblona, J. Ávila, and H. J. Bolink, "Trap-assisted non-radiative recombination in organic–inorganic perovskite solar cells," *Adv. Mater.*, vol. 27, no. 11, pp. 1837–1841, 2015.

[162] Y. Shao, Y. Fang, T. Li, Q. Wang, Q. Dong, Y. Deng, Y. Yuan, H. Wei, M. Wang, A. Gruverman, J. Shield, and J. Huang, "Grain boundary dominated ion migration in polycrystalline organic–inorganic halide perovskite films," *Energy Environ. Sci.*, vol. 9, pp. 1752–1759, 2016.

[163] X. Wu, M. T. Trinh, D. Niesner, H. Zhu, Z. Norman, J. S. Owen, O. Yaffe, B. J. Kudisch, and X.-Y. Zhu, "Trap states in lead iodide perovskites," *J. Am. Chem. Soc.*, vol. 137, no. 5, pp. 2089–2096, 2015.

[164] T. S. Sherkar, C. Momblona, L. Gil-Escrig, H. J. Bolink, and L. J. A. Koster, "Improving perovskite solar cells: insights from a validated device model," *Adv. Energy Mater.*, vol. 7, no. 13, p. 1602432, 2017.

[165] A. B. Sproul, "Dimensionless solution of the equation describing the effect of surface recombination on carrier decay in semiconductors," *J. Appl. Phys.*, vol. 76, no. 5, pp. 2851–2854, 1994.

[166] N. J. Halas and J. Bokor, "Surface recombination on the Si(111) 2×1 surface," *Phys. Rev. Lett.*, vol. 62, pp. 1679–1682, 1989.

[167] X. Wen, W. Chen, J. Yang, Q. Ou, T. Yang, C. Zhou, H. Lin, Z. Wang, Y. Zhang, G. Conibeer, Q. Bao, B. Jia, and D. J. Moss, "Role of surface recombination in halide perovskite nanoplatelets," *ACS Appl. Mater. Interfaces*, vol. 10, no. 37, pp. 31586–31593, 2018.

[168] J. Wang, W. Fu, S. Jariwala, I. Sinha, A. K.-Y. Jen, and D. S. Ginger, "Reducing surface recombination velocities at the electrical contacts will improve perovskite photovoltaics," *ACS Energy Lett.*, vol. 4, no. 1, pp. 222–227, 2019.

[169] J. Idígoras, L. Contreras-Bernal, J. M. Cave, N. E. Courtier, A. Barranco, A. Borras, J. R. Sánchez-Valencia, J. A. Anta, and A. B. Walker, "The role of surface recombination on the performance of perovskite solar cells: Effect of morphology and crystalline phase of tio2 contact," *Adv. Mater. Interfaces*, vol. 5, no. 21, p. 1801076, 2018.

[170] A. Nakane, H. Tampo, M. Tamakoshi, S. Fujimoto, K. M. Kim, S. Kim, H. Shibata, S. Niki, and H. Fujiwara, "Quantitative determination of optical and recombination losses in thin-film photovoltaic devices based on external quantum efficiency analysis," *J. Appl. Phys.*, vol. 120, no. 6, p. 064505, 2016.

[171] P. Cui, P. Fu, D. Wei, M. Li, D. Song, X. Yue, Y. Li, Z. Zhang, Y. Li, and J. M. Mbengue, "Reduced surface defects of organometallic perovskite by thermal annealing for highly efficient perovskite solar cells," *RSC Adv.*, vol. 5, pp. 75622–75629, 2015.

[172] H. Zhu, B. Huang, S. Wu, Z. Xiong, J. Li, and W. Chen, "Facile surface modification of $CH_3NH_3PbI_3$ films leading to simultaneously improved efficiency and stability of inverted perovskite solar cells," *J. Mater. Chem. A*, vol. 6, pp. 6255–6264, 2018.

[173] X. He, Y. Bai, H. Chen, X. Zheng, and S. Yang, "High performance perovskite solar cells through surface modification, mixed solvent engineering and nanobowl-assisted light harvesting," *MRS Advances*, vol. 1, no. 47, pp. 3175–3184, 2016.

[174] E. Y. Tiguntseva, I. N. Saraeva, S. I. Kudryashov, E. V. Ushakova, F. E. Komissarenko, A. R. Ishteev, A. N. Tsypkin, R. Haroldson, V. A. Milichko, D. A. Zuev, S. V. Makarov, and A. A. Zakhidov, "Laser post-processing of halide perovskites for enhanced photoluminescence and absorbance," *J. Phys. Conf. Ser.*, vol. 917, no. 6, p. 062002, 2017.

[175] A. Babayigit, J. D'Haen, H.-G. Boyen, and B. Conings, "Gas quenching for perovskite thin film deposition," *Joule*, vol. 2, no. 7, pp. 1205 – 1209, 2018.

[176] C. Zhu, X. Niu, Y. Fu, N. Li, C. Hu, Y. Chen, X. He, G. Na, P. Liu, H. Zai, Y. Ge, Y. Lu, X. Ke, Y. Bai, S. Yang, P. Chen, Y. Li, M. Sui, L. Zhang, H. Zhou, and Q. Chen, "Strain engineering in perovskite solar cells and its impacts on carrier dynamics," *Nat. Commun.*, vol. 10, no. 1, p. 815, 2019.

[177] D. Liu, M. K. Gangishetty, and T. L. Kelly, "Effect of $CH_3NH_3PbI_3$ thickness on device efficiency in planar heterojunction perovskite solar cells," *J. Mater. Chem. A*, vol. 2, pp. 19873–19881, 2014.

[178] I. Levine, P. K. Nayak, J. T.-W. Wang, N. Sakai, S. Van Reenen, T. M. Brenner, S. Mukhopadhyay, H. J. Snaith, G. Hodes, and D. Cahen, "Interface-dependent ion migration/accumulation controls hysteresis in $MAPbI_3$ solar cells," *J. Phys. Chem. C*, vol. 120, no. 30, pp. 16399–16411, 2016.

[179] D. Kiermasch, P. Rieder, K. Tvingstedt, A. Baumann, and V. Dyakonov, "Improved charge carrier lifetime in planar perovskite solar cells by bromine doping," *Sci. Rep.*, vol. 6, pp. 1–7, 2016.

[180] X. Sun, C. Zhang, J. Chang, H. Yang, H. Xi, G. Lu, D. Chen, Z. Lin, X. Lu, J. Zhang, and Y. Hao, "Mixed-solvent-vapor annealing of perovskite for photovoltaic device efficiency enhancement," *Nano Energy*, vol. 28, pp. 417 – 425, 2016.

[181] T. Sakurai, S. Wang, S. Toyoshima, and K. Akimoto, "Role of electrode buffer layers in organic solar cells," in *2013 International Renewable and Sustainable Energy Conference (IRSEC)*, pp. 46–48, IEEE, March 2013.

[182] G. Garcia-Belmonte, A. Munar, E. M. Barea, J. Bisquert, I. Ugarte, and R. Pacios, "Charge carrier mobility and lifetime of organic bulk heterojunctions analyzed by impedance spectroscopy," *Org. Electron.*, vol. 9, no. 5, pp. 847 – 851, 2008.

[183] D. B. Khadka, Y. Shirai, M. Yanagida, J. W. Ryan, and K. Miyano, "Exploring the effects of interfacial carrier transport layers on device performance and optoelectronic

properties of planar perovskite solar cells," *J. Mater. Chem. C*, vol. 5, pp. 8819–8827, 2017.

[184] G. Juška, K. Genevičius, N. Nekrašas, G. Sliaužys, and G. Dennler, "Trimolecular recombination in polythiophene: fullerene bulk heterojunction solar cells," *Appl. Phys. Lett.*, vol. 93, no. 14, p. 143303, 2008.

[185] K. Yao, F. Li, Q. He, X. Wang, Y. Jiang, H. Huang, and A. K.-Y. Jen, "A copper-doped nickel oxide bilayer for enhancing efficiency and stability of hysteresis-free inverted mesoporous perovskite solar cells," *Nano Energy*, vol. 40, pp. 155 – 162, 2017.

[186] S. Yue, K. Liu, R. Xu, M. Li, M. Azam, K. Ren, J. Liu, Y. Sun, Z. Wang, D. Cao, X. Yan, S. Qu, Y. Lei, and Z. Wang, "Efficacious engineering on charge extraction for realizing highly efficient perovskite solar cells," *Energy Environ. Sci.*, vol. 10, pp. 2570–2578, 2017.

[187] G. Natu, P. Hasin, Z. Huang, Z. Ji, M. He, and Y. Wu, "Valence band-edge engineering of nickel oxide nanoparticles via cobalt doping for application in p-type dye-sensitized solar cells," *ACS Appl. Mater. Interfaces*, vol. 4, no. 11, pp. 5922–5929, 2012.

[188] Q. He, K. Yao, X. Wang, X. Xia, S. Leng, and F. Li, "Room-temperature and solution-processable cu-doped nickel oxide nanoparticles for efficient hole-transport layers of flexible large-area perovskite solar cells," *ACS Appl. Mater. Interfaces*, vol. 9, no. 48, pp. 41887–41897, 2017.

[189] M. Liu, M. Endo, A. Shimazaki, A. Wakamiya, and Y. Tachibana, "Light intensity dependence of performance of lead halide perovskite solar cells," *J. Photopolym. Sci. Tec.*, vol. 30, no. 5, pp. 577–582, 2017.

[190] A. K. K. Kyaw, D. H. Wang, V. Gupta, W. L. Leong, L. Ke, G. C. Bazan, and A. J. Heeger, "Intensity dependence of current–voltage characteristics and recombination in high-efficiency solution-processed small-molecule solar cells," *ACS Nano*, vol. 7, no. 5, pp. 4569–4577, 2013.

[191] K. Tvingstedt, L. Gil-Escrig, C. Momblona, P. Rieder, D. Kiermasch, M. Sessolo, A. Baumann, H. J. Bolink, and V. Dyakonov, "Removing leakage and surface recombination in planar perovskite solar cells," *ACS Energy Lett.*, vol. 2, no. 2, pp. 424–430, 2017.

[192] W. Tress, M. Yavari, K. Domanski, P. Yadav, B. Niesen, J. P. Correa Baena, A. Hagfeldt, and M. Graetzel, "Interpretation and evolution of open-circuit voltage, recombination, ideality factor and subgap defect states during reversible light-soaking and irreversible degradation of perovskite solar cells," *Energy Environ. Sci.*, vol. 11, pp. 151–165, 2018.

[193] W. Rehman, D. P. McMeekin, J. B. Patel, R. L. Milot, M. B. Johnston, H. J. Snaith, and L. M. Herz, "Photovoltaic mixed-cation lead mixed-halide perovskites: links between crystallinity, photo-stability and electronic properties," *Energy Environ. Sci.*, vol. 10, pp. 361–369, 2017.

[194] K. A. Bush, K. Frohna, R. Prasanna, R. E. Beal, T. Leijtens, S. A. Swifter, and M. D. McGehee, "Compositional engineering for efficient wide band gap perovskites with improved stability to photoinduced phase segregation," *ACS Energy Lett.*, vol. 3, no. 2, pp. 428–435, 2018.

[195] F. J. M. Colberts, M. M. Wienk, and R. A. J. Janssen, "Aqueous nanoparticle polymer solar cells: Effects of surfactant concentration and processing on device performance," *ACS Appl. Mater. Interfaces*, vol. 9, no. 15, pp. 13380–13389, 2017.

[196] J. M. Ball, S. D. Stranks, M. T. Hörantner, S. Hüttner, W. Zhang, E. J. W. Crossland, I. Ramirez, M. Riede, M. B. Johnston, R. H. Friend, and H. J. Snaith, "Optical properties and limiting photocurrent of thin-film perovskite solar cells," *Energy Environ. Sci.*, vol. 8, pp. 602–609, 2015.

[197] L. Gil-Escrig, C. Momblona, M.-G. La-Placa, P. P. Boix, M. Sessolo, and H. J. Bolink, "Vacuum deposited triple-cation mixed-halide perovskite solar cells," *Adv. Energy Mater.*, vol. 8, no. 14, p. 1703506, 2018.

[198] M. Zhang, J. S. Yun, Q. Ma, J. Zheng, C. F. J. Lau, X. Deng, J. Kim, D. Kim, J. Seidel, M. A. Green, S. Huang, and A. W. Y. Ho-Baillie, "High-efficiency rubidium-incorporated perovskite solar cells by gas quenching," *ACS Energy Lett.*, vol. 2, no. 2, pp. 438–444, 2017.

[199] J.-W. Lee, Z. Dai, T.-H. Han, C. Choi, S.-Y. Chang, S.-J. Lee, N. De Marco, H. Zhao, P. Sun, Y. Huang, and Y. Yang, "2D perovskite stabilized phase-pure formamidinium perovskite solar cells," *Nature Comm.*, vol. 9, no. 1, p. 3021, 2018.

[200] M. Zhang, H. Yu, M. Lyu, Q. Wang, J.-H. Yun, and L. Wang, "Composition-dependent photoluminescence intensity and prolonged recombination lifetime of perovskite $CH_3NH_3PbBr_{3-x}Cl_x$ films," *Chem. Commun.*, vol. 50, pp. 11727–11730, 2014.

[201] K. Yan, M. Long, T. Zhang, Z. Wei, H. Chen, S. Yang, and J. Xu, "Hybrid halide perovskite solar cell precursors: Colloidal chemistry and coordination engineering behind device processing for high efficiency," *J. Am. Chem. Soc.*, vol. 137, no. 13, pp. 4460–4468, 2015.

[202] D. Khatiwada, S. Venkatesan, N. Adhikari, A. Dubey, A. F. Mitul, L. Mohammad, A. Iefanova, S. B. Darling, and Q. Qiao, "Efficient perovskite solar cells by temperature

control in single and mixed halide precursor solutions and films," *J. Phys. Chem. C*, vol. 119, no. 46, pp. 25747–25753, 2015.

[203] H. Zhou, Q. Chen, G. Li, S. Luo, T.-b. Song, H.-S. Duan, Z. Hong, J. You, Y. Liu, and Y. Yang, "Interface engineering of highly efficient perovskite solar cells," *Science*, vol. 345, no. 6196, pp. 542–546, 2014.

[204] G. Namkoong, A. A. Mamun, T. T. Ava, K. Zhang, and H. Baumgart, "Impact of perovskite precursor solution temperature on charge carrier dynamics and photovoltaic performance of perovskite based solar cells," *Org. Electron.*, vol. 42, pp. 228 – 233, 2017.

[205] M. Jung, S.-G. Ji, G. Kim, and S. I. Seok, "Perovskite precursor solution chemistry: from fundamentals to photovoltaic applications," *Chem. Soc. Rev.*, vol. 48, pp. 2011–2038, 2019.

[206] N. Adhikari, A. Dubey, E. A. Gaml, B. Vaagensmith, K. M. Reza, S. A. A. Mabrouk, S. Gu, J. Zai, X. Qian, and Q. Qiao, "Crystallization of a perovskite film for higher performance solar cells by controlling water concentration in methyl ammonium iodide precursor solution," *Nanoscale*, vol. 8, pp. 2693–2703, 2016.

[207] Y. Lin, X. Ye, Z. Wu, C. Zhang, Y. Zhang, H. Su, J. Yin, and J. Li, "Manipulation of the crystallization of perovskite films induced by a rotating magnetic field during blade coating in air," *J. Mater. Chem. A*, vol. 6, pp. 3986–3995, 2018.

[208] Y. Li, L. Zhi, G. Ge, Z. Zhao, X. Cao, F. Chen, X. Cui, F. Lin, L. Ci, J. Sun, D. Zhuang, and J. Wei, "Investigation on crystallization of $CH_3NH_3PbI_3$ perovskite and its intermediate phase from polar aprotic solvents," *Cryst. Growth Des.*, vol. 19, no. 2, pp. 959–965, 2019.

[209] A. Castro-Carranza, J. C. Nolasco, M. Estrada, R. Gwoziecki, M. Benwadih, Y. Xu, A. Cerdeira, L. F. Marsal, G. Ghibaudo, B. Iniguez, and J. Pallares, "Effect of density of states on mobility in small-molecule n-type organic thin-film transistors based on a perylene diimide," *IEEE Electron Device Lett.*, vol. 33, no. 8, pp. 1201–1203, 2012.

[210] N. Hassan and S. A. Mahmood, "X-ray sensitivity of poly(triarylamine) (PTAA)," in *2015 IEEE International Conference on Telecommunications and Photonics (ICTP)*, pp. 1–4, 2015.

[211] N. Tsutsumi, K. Kinashi, K. Masumura, and K. Kono, "Photorefractive performance of poly(triarylamine)-based polymer composites: An approach from the photoconductive properties," *J. Polym. Sci. B*, vol. 53, no. 7, pp. 502–508, 2015.

[212] G. Chen, F. Zhang, M. Liu, J. Song, J. Lian, P. Zeng, H.-L. Yip, W. Yang, B. Zhang, and Y. Cao, "Fabrication of high-performance and low-hysteresis lead halide perovskite solar cells by utilizing a versatile alcohol-soluble bispyridinium salt as an efficient cathode modifier," *J. Mater. Chem. A*, vol. 5, pp. 17943–17953, 2017.

[213] L. M. Herz, "Charge-carrier mobilities in metal halide perovskites: Fundamental mechanisms and limits," *ACS Energy Lett.*, vol. 2, no. 7, pp. 1539–1548, 2017.

[214] C. Momblona, O. Malinkiewicz, C. Roldán-Carmona, A. Soriano, L. Gil-Escrig, E. Bandiello, M. Scheepers, E. Edri, and H. J. Bolink, "Efficient methylammonium lead iodide perovskite solar cells with active layers from 300 to 900 nm," *APL Mater.*, vol. 2, no. 8, p. 081504, 2014.

[215] G. Giro, J. Kalinowski, P. D. Marco, V. Fattori, and G. Marconi, "Absorption tail photoconductivity in solid films of C60," *Chem. Phys. Lett.*, vol. 211, no. 6, pp. 580 – 586, 1993.

[216] D. Cheyns, J. Poortmans, P. Heremans, C. Deibel, S. Verlaak, B. P. Rand, and J. Genoe, "Analytical model for the open-circuit voltage and its associated resistance in organic planar heterojunction solar cells," *Phys. Rev. B*, vol. 77, p. 165332, 2008.